OPTIMIZATION OF INVERTED ARCHITECTURE METHYLAMMONIUM LEAD IODIDE PEROVSKITE DEVICES AND THE EFFECTS OF WATER ON DEVICE PERFORMANCE

by

Charlotte O.K. Clegg

Submitted in partial fulfillment of the requirements
for the degree of Master of Science

at

Dalhousie University
Halifax, Nova Scotia
August 2016

Table of Contents

List of Tables

List of Figures

Abstract

Methylammonium lead halide perovskites have reached the forefront of next-generation photovoltaic technologies, recently demonstrating a record 20.1 % power conversion efficiency. This thesis details the optimization of solution-processed methylammonium lead iodide perovskites in a planar, inverted device architecture. Sequential deposition of the precursor materials, followed by thermally induced conversion into crystalline perovskite, was found to produce the most uniform film morphology. By controlling the processing atmosphere and relative quantities of deposited precursor, reproducibly efficient perovskite devices were achieved.

A controlled investigation into the effects of water on the photovoltaic performance of perovskites is also presented. Small volumes of water, consistent with those absorbed by air-exposed solvents, were incorporated directly into the perovskite precursor solutions. Increasing water concentrations negatively impacted device performance, exaggerated the current-voltage hysteresis, and introduced different transient behaviours compared to the anhydrous devices. Unexpectedly, the addition of water was also found to improve the long-term device stability.

List of Abbreviations and Symbols Used

Abbreviations

FF	Fill factor
I_{sc}	Short-circuit current (mA)
J_{sc}	Short-circuit current density (mA/cm^2)
R_{RMS}	Root mean squared roughness (nm)
V_{oc}	Open-circuit voltage (V)
AFM	Atomic force microscopy; or, Atomic force microscope
Ca/Al	Calcium/aluminum bilayer
DI	De-ionized
DMF	n,n-dimethylformamide
FTO	Fluorine-doped tin oxide
ITO	Indium tin oxide
MAI	Methylammonium iodide
$MAPbI_3$	Methylammonium lead iodide
MoO_x/Ag	Molybdenum oxide/silver bilayer
PbI_2	Lead iodide
PCBM	[6,6]-phenyl-C61-butyric acid methyl ester
PCE	Power conversion efficiency, (%)
PEDOT:PSS	poly(3,4-ethylenedioxythiophene)-poly(styrenesulfonate)

PL	Photoluminescence
PV	Photovoltaic
SEM	Scanning electron microscopy; or, scanning electron microscope
SMU	Source measure unit
spiro	$2,2',7,7'$-tetrakis-(N,N-di-p-methoxyphenylamine)-$9,9'$-bifluorene
TiO_2	Titanium dioxide
XPS	X-ray photoelectron spectroscopy
XRD	Xray diffractometry; or, xray diffractometer

Symbols

χ	Ionization energy, (eV)
η	Power conversion efficiency, (%)
ϕ_w	Work function, (eV)
E_A	Electron affinity, (eV)
E_C	Conduction band minimum, (eV)
E_F	Fermi level, (eV)
E_g	Bandgap, (eV)
E_{vac}	Vacuum level
E_V	Valence band maximum, (eV)
I_0	Diode current
I_{ph}	Photocurrent

k_b	Boltzmann constant, 1.38×10^{-23} J/K
q	Elementary charge, 1.6×10^{-19} C
R_{sh}	Shunt resistance, (Ω)
R_s	Series resistance, (Ω)
T	Temperature (K)
V	Applied bias, (V)

Acknowledgements

In the process of these last two years many people have contributed both directly and indirectly to the outcomes of this work. First, and foremost, is Dr. Ian G. Hill. His expertise in organic (and inorganic) electronics, construction and design has made this a tremendous learning experience. Equally valuable has been his counselling and advice. Thank you, for keeping me on track. This learning experience was also greatly enriched by Jon-Paul Sun's broad knowledge base and leadership in the lab. I learned a great deal about equipment maintenance and effective research habits both directly and indirectly from his example. One of my later projects (which is not discussed in this thesis) involved a large amount of construction and design. The final product benefited greatly from the input and guidance provided by John Noddin and Kevin Borgel in the machine shop.

I would also like to thank all of my committee members, Dr. Jeff Dahn, Dr. Kimberley Hall and Dr. Ian Hill for their flexibility and feedback, which have allowed my thesis to reach this final stage.

Many office discussions whether about research, or household pets have helped me maintain a reasonable perspective of reality. Thank you Carmen Lee, JP Sun, Jess Topple, Andrew Namespetra, Allan Hupman, Cody Church and Samuel Cameron.

Last, but not least, I would like to thank Chris Lee, for his kind encouragement and moral support these past two years; and, finally, my family for their words of confidence and reminders to take care of myself. Thank you all.

Chapter 1

Introduction

As the global population continues to grow, research into clean sustainable energy sources has become increasingly urgent. Since the industrial revolution, coal and fossil fuel combustion have accelerated rising atmospheric carbon dioxide levels, resulting in serious environmental degradation. From an economic standpoint, the price of oil is highly volatile, subject to the supply afforded by local and global events. Although subject to debate, some estimations place peak oil within a couple decades of the present date; meanwhile, global energy consumption is expected to more than double by 2050 [1, 2]. It is clear that renewable energy development is no longer purely an environmental issue, but also one of serious economic importance.

Among the many clean-energy contenders, solar energy is widely considered to be an attractive option, owing to its global accessibility and abundance. Enough solar energy reaches the Earth's surface in a single hour to meet the world's current energy demands for a year. Within the last five years, the cumulative world photovoltaic capacity has grown tremendously; at the end of 2015 the world solar power production accounted for 1.3% of the world's total energy supply – up from 0.1% in 2012 [1, 3]. Some of the most successful photovoltaic (PV) technologies such as crystalline, multi-crystalline and amorphous silicon solar cells rely on lengthy, high-temperature fabrication processes. Such procedures are both financially and energetically expensive; however, under optimal operating conditions, complete energy payback of silicon PV systems may be achieved within two years [4].

Next generation PVs, such as organic, polymer and perovskite solar cells, aim to address the limitations of existing commercial PV technologies. Next generation PVs offer the advantage of low-temperature solution processability, which dramatically reduces the financial and energetic costs of production. Low-temperature solution processing also introduces the possibility of fabrication on flexible, plastic substrates. Several limitations, such as material stability and lower power conversion efficiencies

still limit the viability of this technology; however, addressing these issues could allow next generation photovoltaics to revolutionize the solar industry.

1.1 Perovskites in the energy economy

Perovskite photovoltaics have rapidly entered the forefront of next generation technologies. Through basic improvements to device architecture, film coverage and morphology, the efficiencies of methylammonium lead halide ($CH_3NH_3PbX_3$; X = I, Cl or, Br) perovskites have risen from a modest 3 % to a record 20.1 % in just over five years [5, 6]. The efficiencies of some perovskite PVs now rival those of commercially available silicon solar cells. Yet, the appeal of perovskite PVs does not rest exclusively on their strong performance; rather, the fact that such strong performance is achievable through low-temperature solution processing. Many research groups have shown that high device efficiencies can be achieved using facile solution processing techniques, which are easily scalable for mass-production [7–13]. Slot-die coated and inkjet printed perovskite devices have already achieved efficiencies in excess of 10 %, which is a promising indicator for the commercial viability of this technology [14, 15]. Currently, long-term stability remains the largest barrier to perovskite development. The lifetime of organometal halide perovskites is known to be limited by several factors, including atmospheric, chemical, thermal and illumination conditions [16, 17]. At present, record stabilities are reported on the order of 1000 hours, which is still too low to be commercially attractive [18–20]. In order for these materials to become commercially realized, the average device lifetime must be substantially raised to reach the industry standard of approximately 20 years.

1.2 Organization of the thesis

The remainder of this thesis is organized into five chapters. The following chapter will discuss the processes governing basic photovoltaic operation as well as the measurement and significance of typical figures of merit. The chapter will end with a brief description of some key properties of perovskite PVs and their operation. The third chapter outlines the general experimental techniques employed in this work; project specific fabrication details will be described further in relevant chapters. The

main body of results are addressed in Chapters 4 and 5. Chapter 4 describes the optimization of efficient inverted-architecture perovskite PVs within the Hill lab. Chapter 5 examines the effects of unintentional water incorporation on perovskite PVs. The final chapter summarizes the main conclusions drawn from this work, and their relevance in the context of perovskite photovoltaics; direction for future work is also suggested.

Chapter 2

Theory of photovoltaic operation

2.1 Overview

Solar photovoltaics (PVs) are electronic devices, which generate electrical energy through the absorption of light. Solar PVs may be modelled as a current source in parallel with a diode, where the magnitude of delivered current is proportional to the incident light intensity. A photovoltage is also developed across the device, enabling it to do electrical work on an external load. This chapter will discuss the principles of photovoltaic operation in inorganic semiconductors, beginning with photon absorption and charge separation. A description of the ideal diode model, and device characterization using common figures of merit follows. The chapter concludes with an overview of significant developments in the fabrication and structure of perovskite PVs.

2.2 Processes in inorganic semiconductors

2.2.1 Photon absorption

To convert optical energy into electrical energy a photovoltaic device must generate and separate free charges (electrons and holes). Carrier generation is achieved through the absorption of incident photons. When a photon of sufficient energy is absorbed, an electron is excited into a higher energy state; this leaves a vacancy, or hole, in its original energy level. The collection of electrons and holes by a cathode and anode, respectively, produces a net photocurrent.

Carrier motion within a solar cell is facilitated by the presence of energy bands within the photoactive material. Energy bands arise from the arrangement of atoms in a crystalline lattice. When a large number of atoms are present, such as in a crystalline solid, the atomic orbitals are split into a near-infinite number of unique energy levels, which may be approximated as a continuum, or an energy band. A

diagram illustrating the formation of energy bands from atomic orbital splitting is shown in Figure 2.1.

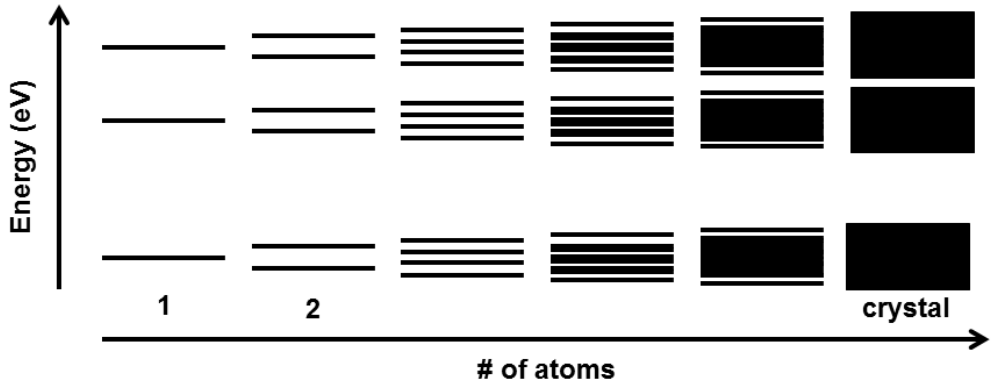

Figure 2.1: Schematic illustrating the formation of energy bands in a crystalline solid.

Depending on the occupancy of the original atomic orbitals, the resulting bands may also be occupied (valence band), or vacant (conduction band). The forbidden range of energies separating the conduction and valence bands is the bandgap (E_g), which is defined with respect to the valence band maximum (E_V, highest valence band energy) and the conduction band minimum (E_C, lowest conduction band energy). The difference between vacuum level and the valence band maximum is defined as the ionization energy (χ), while the difference between vacuum level and the conduction band minimum is defined as the electron affinity (E_A).

$$\chi \equiv E_{vac} - E_V \tag{2.1}$$

$$E_A \equiv E_{vac} - E_C \tag{2.2}$$

A labelled band diagram illustrating these features is shown in Figure 2.2 for brevity.

The absorption and charge transport properties of a material are dictated by its electronic band structure. Photons with energy $E \geq E_g$ are easily absorbed; photons with energy $E < E_g$ are not absorbed, and are transmitted through the material. When the bands are either completely empty or occupied, no net charge transport is possible; a partially filled band is necessary for transport. Photon absorption results in the excitation of electrons to the conduction band, leaving a vacancy, or

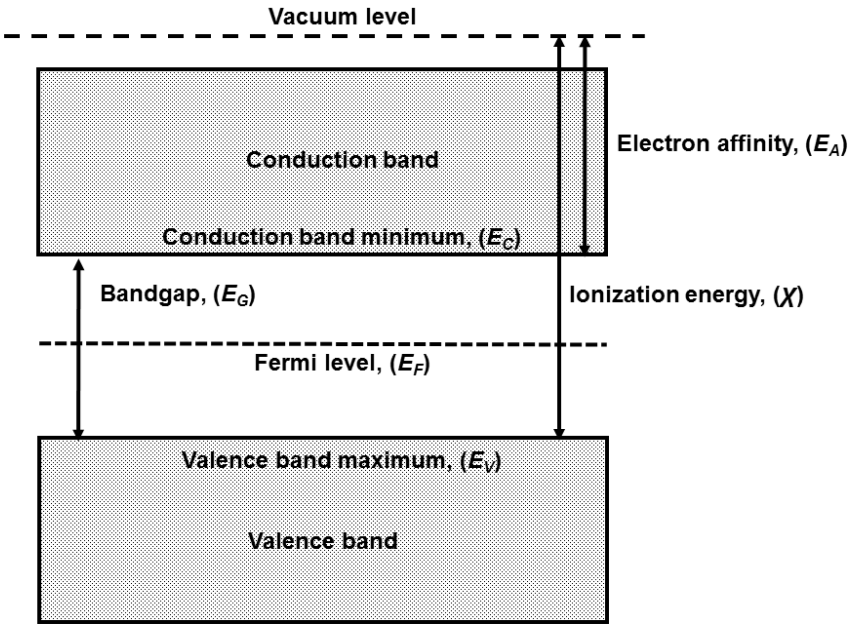

Figure 2.2: Labeled diagram of a crystalline solid, illustrating the conduction band, valence band, bandgap, electron affinity and ionization potential. The Fermi level is also shown (assuming an intrinsic semiconductor).

hole, in the valence band. The presence of electrons in the conduction band and holes in the valence band enables net charge transport to occur in an external field. In the valence band, neighbouring electrons will easily move to occupy holes. For convenience, however, charge transport in the valence band is defined in terms of hole motion. Electrons and holes are both referred to as charge carriers and contribute identically to current flow. The current resulting from photoexcitation is termed the photocurrent.

The maximum photocurrent generated by a photovoltaic device occurs under zero bias, and is referred to as the short-circuit current (I_{sc}). The short-circuit current can be related to a cell's incident spectral irradiance (b_s), and its external quantum efficiency ($QE(E)$), which is the probability that a single photon, of energy E, can supply an electron to an external load.

$$I_{sc} = q \int \frac{b_s(E) QE(E)}{\hbar\omega(E)} dE \tag{2.3}$$

The quantum efficiency is dependent on the material absorption, charge separation

efficiency and charge collection efficiency. For an ideal solar cell, these processes are assumed to be 100 % efficient above the bandgap, above which the quantum efficiency is taken to be unity. The maximum current generated by an ideal photovoltaic is therefore only dependent on the incident light intensity and spectrum.

2.2.2 Charge separation and transport: the pn junction

The separation of charge carriers is enabled by the electronic structure of the photoactive material and the built-in electric field within a PV device. The presence of energy bands ensures that photoexcited electrons remain in an excited state long enough to be extracted at a potential energy above the ground state; without a band gap the excited electrons would scatter into lower energy states within femtoseconds [21].

The driving force for carrier extraction may be provided by the difference in work function between the two electrodes contacting the cell. The work function (ϕ_w) of a metal is the minimum energy required to move an electron from the metal's surface to the vacuum level. More generally, it is equivalent to the difference between the vacuum (E_{vac}) and Fermi (E_F) levels

$$\phi_w = E_{vac} - E_F \tag{2.4}$$

where the Fermi level defines an equilibrium energy level with an occupancy probability of 50 %, separating filled from empty states. When two materials are in contact, electrons are thermodynamically driven to the higher work function material until the Fermi levels of the two materials are aligned. When this occurs between the two electrodes of a PV device, the redistribution of charge establishes an electric field, which facilitates the separation of photogenerated charge carriers.

A Fermi level difference within a PV device can also occur between two compositionally different materials, ultimately giving rise to an electric field across their junction. This effect is commonly modelled by a p-n junction, and forms the basis for charge separation within a PV cell. For intrinsic (undoped) semiconductors at absolute zero, the Fermi level lies halfway between the conduction and valence bands (Figure 2.2); however, its position can be adjusted by doping, which is the controlled addition of chemical impurities into the host crystal structure.

Chemical impurities introduce energy states within the bandgap that are close to the band edge relative to k_bT (25 meV at room temperature). In n-type doping, occupied gap states are introduced near the conduction band edge, and excess electrons are easily transferred into the conduction band. Meanwhile, p-type doping introduces unoccupied gap states near the valence band edge. Electrons from the valence band may easily occupy these states, introducing additional holes into the valence band (Figure 2.3). Because they are in excess, holes and electrons are termed the majority charge carriers in p- and n-type semiconductors, respectively. Despite their excess of majority carriers, doped semiconductors remain electrically neutral due to the balancing charge on the initial impurities. In doped semiconductors, photogeneration leads to a comparatively greater increase in the minority carrier population (electrons in p-type semiconductors and holes in n-type semiconductors).

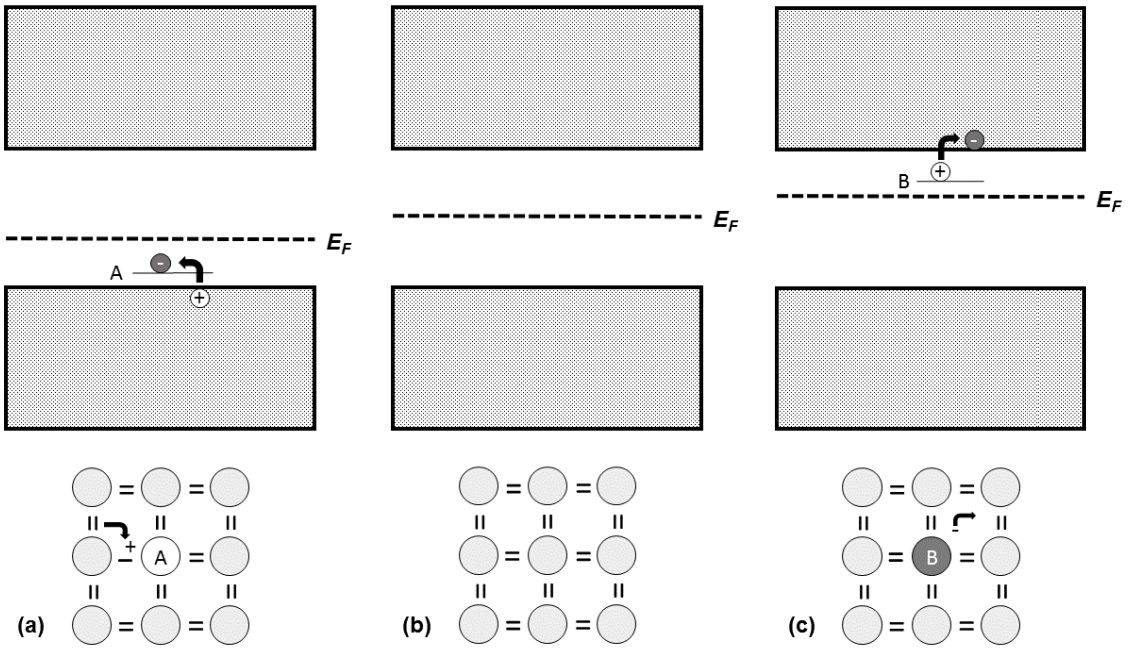

Figure 2.3: Diagram illustrating the effect of (a) p-type and (c) n-type doping with respect to an intrinsic semiconductor (b). When energy states are introduced near the band edge, the energy required for carrier transfer into the valence and conduction bands is easily satisfied at room temperature.

At a p-n interface, majority carriers are thermodynamically driven to diffuse across the junction, leaving an oppositely charged ion core behind, bound in the crystal lattice. The diffusion of majority carriers is known as the diffusion current,

and the volume occupied by the remaining ion cores is the depletion region. The oppositely charged ion cores in the depletion region generate an electric field across the junction, limiting the diffusion current and the width of the depletion region. The electric field across the interface also enables charge separation by helping to sweep photogenerated carriers across the junction, towards their respective electrodes.

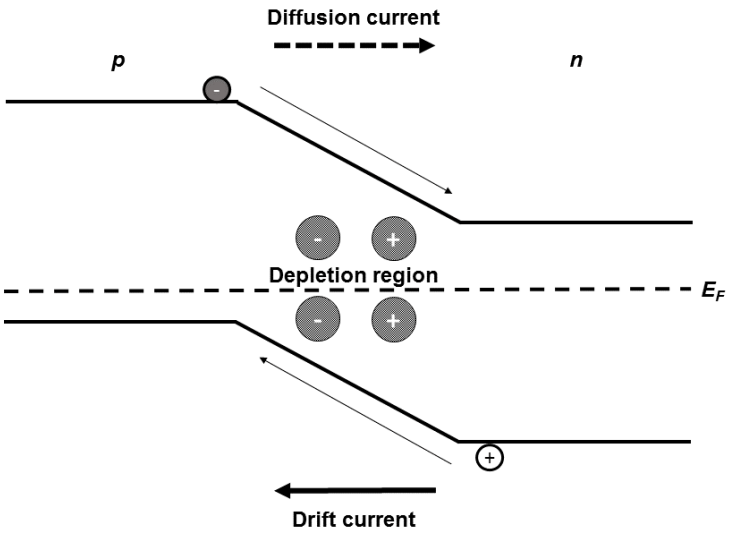

Figure 2.4: Schematic illustrating charge separation across a p-n junction. The photogenerated minority carriers are easily swept across the junction by the built-in field. The spatial location of the ion cores remaining within the depletion region are also illustrated.

2.3 Ideal diode behaviour

The short-circuit current in an ideal solar cell can be related to the cell's quantum efficiency and incident spectral irradiance as described in Equation 2.3. By convention, the photocurrent (I_{ph}) is negatively signed. When an external load is connected to the device, a potential bias develops in opposition to the photocurrent. The opposing current reduces the net current that may be extracted from the device, and is referred to as the diode current (I_0). The overall current-voltage (IV) behaviour of a PV device is well-approximated by the superposition of the photocurrent and the diode current, as described by the ideal diode equation

$$I(V) = I_0(e^{\frac{qV}{k_b T}} - 1) - I_{ph} \tag{2.5}$$

where q is the elementary charge (C), V is the applied bias (V), k_b is the Boltzmann constant (J/K), and T is the ambient temperature (K). The ideal diode equation is modelled by a current source in parallel with a diode; an equivalent circuit is given in Figure 2.5 (a). The relationship between the net current, photocurrent and diode current is highlighted in Figure 2.5 (b), where the power generated

$$P_{gen} = -IV \tag{2.6}$$

is also shown on the secondary axis.

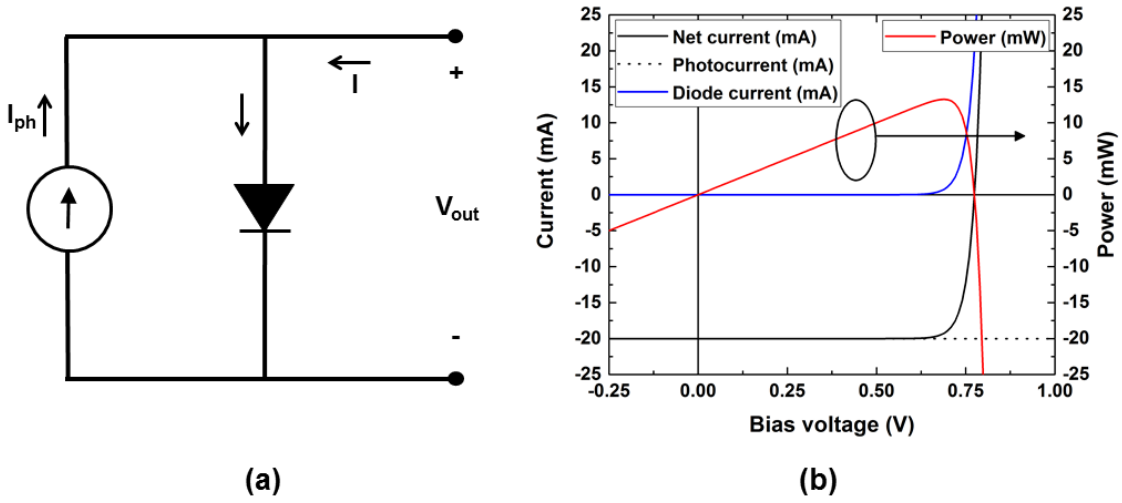

Figure 2.5: Equivalent circuit diagram for the ideal diode model of a photovoltaic device (a), and its corresponding current-voltage behaviour (b).

2.4 Evaluation of device performance:

2.4.1 Current-voltage measurement:

As previously described, the power generated by an operating photovoltaic device can easily be determined from the product of its bias and output current at a particular operating bias. However, additional information about a device's performance can be evaluated by measuring its current-voltage behaviour over a range of applied biases. This can be done by using a source measure unit (SMU), sweeping a range of

bias potentials across the device, while simultaneously measuring the resulting current. Such current-voltage (IV) measurements are performed both with and without illumination. Given the range of global and temporal variations in solar intensity, a calibrated light source must be used for measurements under illumination. Often, the illumination source is designed to simulate AM1.5 light, which is a standardized spectrum representing the spectral irradiance received at the Earth's surface from the sun at a 42^o elevation angle. The AM1.5 illumination intensity is normalized to 1000 W/m^2. (Other standardized spectra may also be used). Once the IV behaviour is known, the maximum generated power can be identified by inspection.

2.4.2 Figures-of-merit:

In addition to its maximum power, the performance of a PV device is most commonly described by four figures of merit: the open-circuit voltage (V_{oc}), the short-circuit current (I_{sc}), the fill factor (FF) and the power conversion efficiency (PCE, η). To eliminate the dependence of photocurrent on device area, it is common practice to report the short-circuit current density (J_{sc}) in place of I_{sc}. This convention is adopted for the remainder of the thesis.

For a device measured under illumination, the open-circuit voltage is the voltage at which no net current is produced by the device. At the open-circuit voltage, the photogenerated current is exactly matched by the dark current. The open-circuit voltage is a measure of the rectifying behaviour of a device; a low V_{oc} reflects poor rectification. Rearranging the ideal diode equation at open-circuit conditions shows the dependency of V_{oc} on the dark current.

$$V_{oc} = \frac{k_b T}{q} \ln(1 + \frac{I_{sc}}{I_0}) \tag{2.7}$$

Since the dark current is dependent on recombination rates within the device, the open-circuit voltage is, by extension, another indicator of device recombination. Roughly speaking, the maximum open-circuit voltage can be approximated by the difference between the electron affinity and ionization energy at the cathode and anode interfaces, respectively.

The short-circuit current density represents the maximum current that can be

extracted from a device, which occurs under zero bias when the two contacts of opposite polarity are shorted together. As previously described, the short-circuit current (density) is dependent on the incident spectral irradiance and quantum efficiency of a particular device (Equation 2.3). A higher incident light intensity results in a greater number of photoexcited carriers and therefore a higher net current (density). Meanwhile, the quantum efficiency envelops several internal properties of a device, namely its absorbance, and charge separation and collection efficiencies. Although a higher number of photons may be absorbed by using a thicker photoactive layer, the charge separation and collection efficiencies may be compromised if the thickness becomes large enough to limit the strength of the built-in field between electrodes. The finite resistance of the photoactive layer may also become current-limiting if the photoactive layer becomes too thick.

The fill factor (FF) describes the ideality of a measured JV curve. It is the ratio of the maximum measured power to the maximum power that is theoretically achievable (schematically depicted in Figure 2.6). As the fill factor approaches unity, the device behaves like an ideal infinite-step function. Maximum power generation is achieved at the elbow of a JV curve, near the product of V_{oc} and J_{sc}.

$$FF = \frac{P_{max}}{J_{sc}V_{oc}} \tag{2.8}$$

In reality, internal losses such as series resistance and leakage current limit the maximum power that may be generated, reducing the device fill factor.

The power conversion efficiency is the most general figure of merit used to compare photovoltaic devices; it represents the ratio of the maximum electrical power extracted from the device (P_{max}) to the incident optical power (P_{in}). Equivalently, the PCE may be represented as the product of the open-circuit voltage, short-circuit current and fill factor compared with the incident power (Equation 2.9). An improvement to any of these parameters will increase the overall device efficiency.

$$\eta = \frac{P_{max}}{P_{in}} = \frac{V_{oc}I_{sc}FF}{P_{in}} \tag{2.9}$$

The maximum theoretical PCE for a single junction solar cell was predicted to be 30 % by William Shockley [22]. This limit stems from a trade-off between the

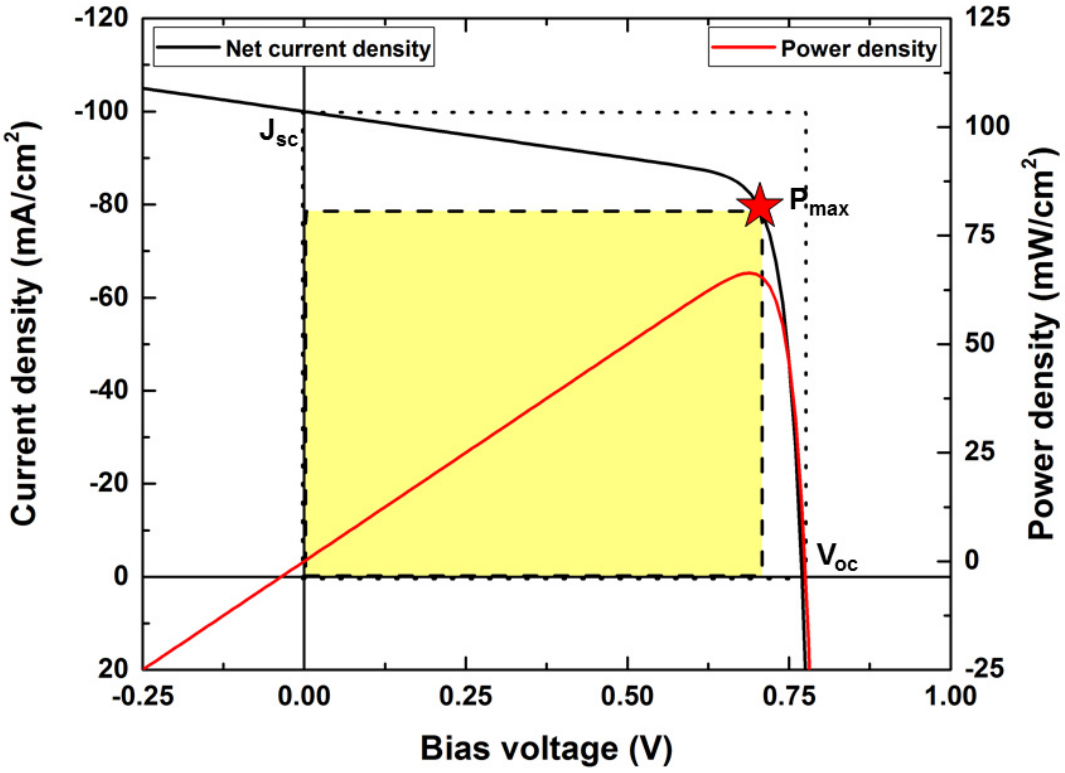

Figure 2.6: Schematic depicting the calculation of a device fill factor from the maximum generated power, the open-circuit voltage and the short-circuit current density.

photocurrent and operating voltage, which both contribute to the generated power (Equation 2.6). A higher photocurrent may be achieved from a smaller bandgap material at the cost of a lowered operating voltage. Assuming the junction is illuminated by a 6000 K black-body radiator, a maximum 30 % efficiency can be achieved using a 1.1 eV bandgap material; this is known as the Shockley-Queisser limit.

2.5 Parasitic losses and non-ideal behaviour

In reality, the maximum efficiency of a photovoltaic device is restricted by internal losses, such as series and shunt resistances. In the presence of such parasitic resistances, electric power is dissipated within the device, reducing the net power generated. An equivalent circuit diagram incorporating parasitic losses is shown in Figure 2.7 (a), for which the diode equation becomes:

$$I(V) = I_0(e^{\frac{q(V-IR_s)}{k_bT}} - 1) - I_{ph} + \frac{V - IR_s}{R_{sh}} \tag{2.10}$$

where I_{ph} is the photocurrent, R_s is the series resistance and R_{sh} is the shunt resistance.

Shunt resistance results from parasitic leakage current through the device. In thin film devices, a low shunt resistance may be attributed to defects such as pinholes permeating through active layer. Figure 2.7 (b) illustrates the effect of lowered shunt resistance, highlighting the decreased fill factor and generated power. For a low enough shunt resistance, the open-circuit voltage may be reduced. Figure 2.7 (c) illustrates the similarly detrimental effect of increased series resistance on device performance. A high series resistance limits current flow through the device. Series resistance commonly originates from contact resistance at the electrode interfaces as well as the finite conductivity of the photoactive materials. For a high enough series resistance, the short circuit current of the device may be compromised. Ideal photovoltaic performance requires high shunt resistance and minimal series resistance.

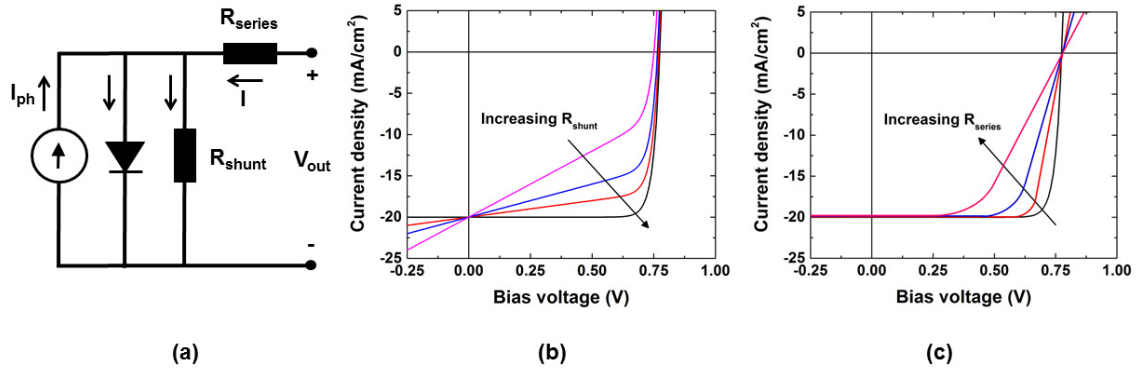

Figure 2.7: Equivalent circuit diagram for a photovoltaic device containing parasitic resistances (a). The JV behaviour of a device with zero series resistance is shown in (b) with varying shunt resistance. The JV behaviour of a device with infinite shunt resistance is shown in (c) with varying series resistance.

2.6 A description of perovskite photovoltaics

The term perovskite refers to a class of materials sharing a common ABX_3 crystal structure, where A and B are two differently sized cations coordinated with the X

anion. The typical cubic perovskite stucture is shown in Figure 2.8 (a), which illustrates the six-fold coordination of the B cation and the octahedral cage surrounding the A cation. Recently, the term perovskite has been adopted in reference to a particular family of perovskite-structured materials exhibiting photovoltaic properties, the organometal halides. Of all the organometal halide perovskites, methylammonium lead halides ($MAPbX_3$) are the most well-studied, and have been shown to demonstrate the highest power conversion efficiencies [6]. Figure 2.8 (b) illustrates the tetragonal $I4cm$ $MAPbI_3$ crystal structure, which occurs at room temperature. The tetragonal phase is known to undergo phase transitions at 330 K and 160 K into the cubic $Pm\bar{3}m$ and orthorhombic $Pnma$ phases, respectively. Lower dimensional 2D-layered, 1D- and 0D-nanostructured perovskites are also possible [23,24,24,25]. This thesis deals exclusively with the methylammonium lead iodide material ($MAPbI_3$), which is loosely referred to as perovskite, herein.

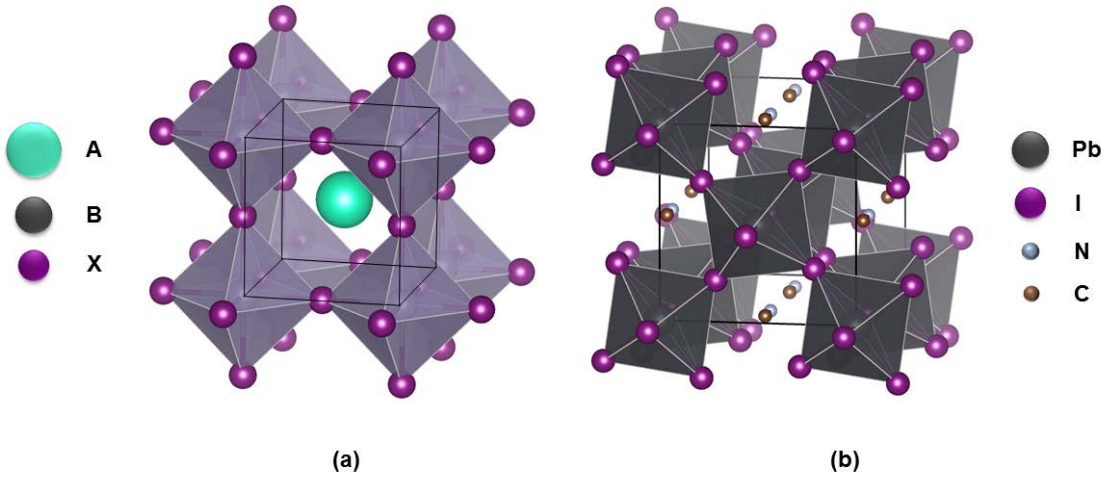

Figure 2.8: Figure illustrating the typical ABX_3 cubic perovskite cyrstal structure (a). The tetragonal methylammonium lead iodide crystal structure, which occurs at room temperature is shown in (b).

Since their first use as light-sensitizers in dye-sensitized solar cells [5], perovskite PV devices have made incredible progress. Aside from their solution-processability, several unique properties contribute to the strong photovoltaic performance of $MAPbI_3$ perovskites, making them promising candidates for next generation solar cells.

The bandgap of $MAPbI_3$ is approximately 1.60 eV, close to the ideal bandgap predicted by the Schockley-Quiesser limit [22,26]. If the illumination source is assumed

to be the AM1.5G (instead of black body) spectrum, the limit predicts that maximum photovoltaic efficiency (33 %) is achieved from a 1.4 eV bandgap material [27]. Above the bandgap, $MAPbI_3$ perovskites exhibit optical strong absorption. This is, in part, due to the high density of electronic states near the conduction and valence band edges, which increases the number of possible photoexcitation events [26,28,29].

$MAPbI_3$ perovskites demonstrate excellent charge transport properties. Upon photoexcitation, free electrons and holes are generated. In most organic photovoltaics, photoexcited electrons and holes experience strong electrostatic attraction, resulting in a bound electron-hole pair, called an exciton. In organic photovoltaics, the exciton binding energy may be as high as 1.4 eV [30]. In comparison, the measured binding energies in $MAPbI_3$ perovskites range between 37 - 55 meV, so the bound electrons and holes are easily liberated at room temperature ($k_b \approx 25$ meV) [31,32]. Once generated, the free carriers exhibit abnormally low recombination rates, and by consequence long carrier diffusion lengths [33–35]. Studies have found electron/hole diffusion lengths ranging from hundreds of nanometers to micrometers in length [34, 35]. Such long diffusion lengths are enabled by the defect tolerance of the $MAPbI_3$ structure [29]. In general, deep-level (mid-gap) defect states act as carrier trapping and recombination centres, and limit the device V_{oc}. In $MAPbI_3$ perovskites, the formation energy for deep-level defect states is high; whereas, the formation energy for shallow-level defect states is much lower [29,36,37]. The shallow-level defect states are predicted to occur within $\pm$ 0.05 eV of the band edges; some are even predicted to occur within the conduction and valence bands [29, 37]. As a result, the effect of defect states on charge carrier trapping is minimal.

There are many variations to the perovskite device structure; however, the most general form is based on a methylammonium lead halide perovskite layer sandwiched between two charge-selective transport layers: a hole transport layer and an electron transport layer. The order of the electrodes and charge-selective layers defines the architecture of the device. Perovskite PVs in which electrons are collected through the base of the device are said to be of normal architecture. Historically, this originates from the first all solid-state structure perovskite device to evolve from perovskite-sensitized solar cells [38]. It is worth clarifying that this naming convention is reversed in the more established organic PV field. Figure 2.9 illustrates the normal

and inverted device architectures for a planar structured perovskite device.

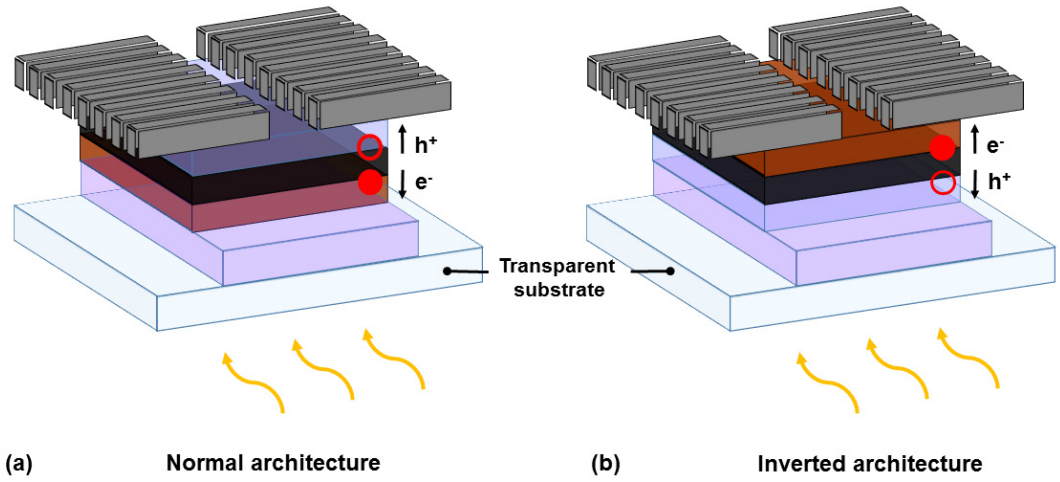

Figure 2.9: Schematic illustrating the normal (a) and inverted (b) device architectures for a planar structured perovskite solar cell.

A common variation to the planar device structure is the use of an additional mesoporous scaffold on top of the bottom charge-selective transport layer. The mesoporous layer is a nanoporous film of sintered metal oxide, which may act either as an insulating scaffold such (e.g. Al_2O_3), or a porous extension of the charge-selective material (e.g. TiO_2). The mesoporous structure is easily infiltrated by solution-processed perovskite, which may form an additional "capping layer" on top of the mesoporous film [39–41]. Mesoporous layers are not a requirement for high-performance devices; however, they have been found to facilitate the formation of continuous perovskite films [42, 43]. Still, there is considerable motivation to move away from the use of mesoporous layers in favour of inverted planar-structure devices. The inverted device architecture enables the use of all organic charge-selective transport layers, which may be formed by low-temperature solution-processing; as a result, planar organic transport layers simplify device processing requirements, and allow for fabrication on flexible substrates. In contrast, mesoporous metal oxide films require extensive high-temperature treatment (typically at 500 – 550 °C), which is above the melting temperature of most flexible substrates [39–41].

In perovskite devices, it is the charge-selective transport layers that provide the

driving force for carrier separation. Through careful material selection, proper energy band alignment can be achieved such that the removal of a particular carrier is energetically favoured by one material and discriminated by the other. The exclusive removal of electrons and holes on opposite sides of the perovskite layer establishes a carrier density gradient across the perovskite film, facilitating the separation of photogenerated charge. Carrier migration to their selective transport layers is facilitated by the excellent transport properties of the perovskite thin film.

The band diagrams illustrating the energy landscape for typical inverted and normal device architectures are shown in Figure 2.10 for open-circuit and short-circuit conditions. Under short-circuit conditions and thermodynamic equilibrium, Fermi level alignment between the two metal contacts creates a potential difference across the device. The potential difference between the two contacts causes electrons and holes to be preferentially collected by the low and high work function electrodes, respectively. In the inverted architecture device, the anode, hole transport material, electron transport material and cathode are illustrated using indium tin oxide (ITO), poly(3,4-ethylenedioxythiophene)-poly(styrenesulfonate) (PEDOT), [6,6]-phenyl-C61-butyric acid methyl ester (PCBM) and a calcium/aluminum bilayer (Ca/Al), respectively. In the normal architecture device, the cathode, electron transport material, hole transport material and anode are illustrated using fluorine-doped tin oxide (FTO), titanium dioxide (TiO_2), $2,2',7,7'$-tetrakis-(N,N-di-p-methoxyphenylamine)-$9,9'$-bifluorene (spiro), and a molybdenum oxide/silver bilayer (MoO_x/Ag), respectively. Under non-equilibrium conditions, the work functions of the ITO, Ca/Al, FTO and MoO_x/Ag contacts are 4.7 eV, 2.9 eV, 4.5 eV and 5.6 eV, respectively.

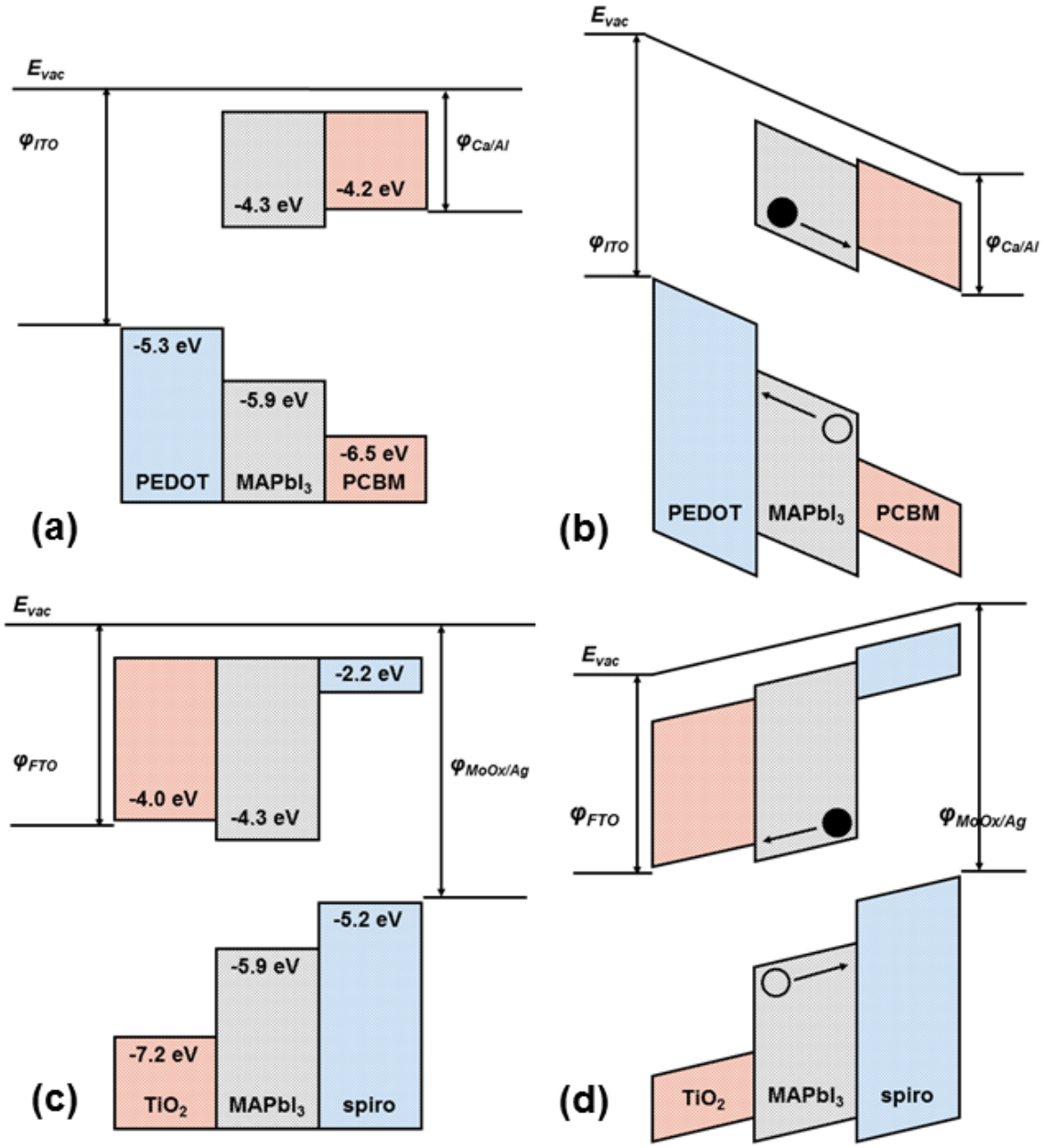

Figure 2.10: Band diagrams illustrating the energy landscape within a typical inverted architecture device under (a) open-circuit and (b) short-circuit conditions. Band diagrams for a typical normal architecture device are also shown under (c) open-circuit and (d) short-circuit conditions. Electron affinities, ionization energies and work functions (ϕ_x) are indicated where relevant.

Chapter 3

Experimental techniques

3.1 Sample preparation

3.1.1 Cleaning

Substrate cleaning is an important step in thin film deposition, as debris and residues can influence film formation and wetting. In this study, all substrate cleaning is performed in a class 1000 clean room. Glass and indium tin oxide (ITO)-coated glass substrates are cleaned by scrubbing in de-ionized (DI) water and Sparkleen^{TM} detergent. The substrates are then ultrasonicated in a clean glass staining jar using baths of detergent, DI water, acetone and ethanol. The ultrasonication is performed by placing the glass staining jar in water bath, which is agitated with a high-frequency transducer. As sound waves generated by the transducers propagate through the solution, alternating low and high pressure pulses enable repeated cavitation and collapse of microscopic bubbles. Contaminants are removed from all surfaces when the bubbles collapse. After ultrasonication, the substrates are dried with filtered compressed air to prevent residue formation.

UV-ozone treatment is used as a final cleaning step. The substrates are placed in an isolated chamber and exposed to UV radiation, which causes dissociation of organic contaminants, and the formation of atomic oxygen and ozone from diatomic oxygen. The dissociated organic molecules react with the atomic oxygen to produce volatile molecules such as CO_2, H_2O and N_2, which are removed from the substrate surface [44].

3.1.2 Thin-film deposition: spin coating and thermal evaporation

Materials that are soluble, or easily dispersed are well-suited for solution processing. Among the many solution processing techniques, spin coating is advantageous due to the relative ease in which a thin film of uniform thickness can be obtained. Although

higher throughput techniques (such as roll-to-roll processing) are possible, spin coating is ideal for material research and development due to its low cost, reproducibility, and high turnover rate [45].

The entire spin coating procedure consists of three stages (Figure 3.1). During the first stage, a volume of solution is dispensed onto a stationary, or spinning substrate. As the substrate is accelerated to a desired rotational velocity, the interaction between viscous and centrifugal forces dictates solution spreading and thinning. As the substrate continues to spin, excess solution is expelled from the substrate, leaving a thin fluid layer. During the last stage, solvent evaporation dominates the formation of the final coating, eventually leaving a thin dry film of material. Choice of solvent, solution concentration, solution temperature, rotational velocity, acceleration, and spinning duration may all affect the thickness, morphology and molecular orientation of the final film. The resulting film thickness can be described by the empirical relationship

$$h = k\omega^{\alpha} \tag{3.1}$$

where ω refers to the rotational velocity, and k and α are empirically determined constants related to solute, solvent and substrate properties. The parameter α is typically found to be -0.5 [46]. Colloquially, the rotational velocity of the substrate is referred to as the spin speed, a term that is adopted throughout the remainder of this thesis.

Thermal evaporation is necessary for the deposition of non-soluble, or poorly-soluble materials; and, is carried out in a vacuum chamber below 4 x 10^{-6} torr base pressure. The pressure is monitored throughout the deposition using an ion gauge in which the measured ion current is directly proportional to the pressure in the vacuum chamber. In an ion gauge, electrons are thermionically emitted from a heated filament, and accelerated towards a positively biased wire grid. Collision of electrons with gas molecules in the vacuum system results in positive ions, which generate a current when collected. The ion current is directly proportional to the density of gas molecules and, therefore, the pressure.

Once a suitable base pressure is reached, deposition is achieved by Joule heating of an evaporation source, which may be a crucible, boat or basket containing the

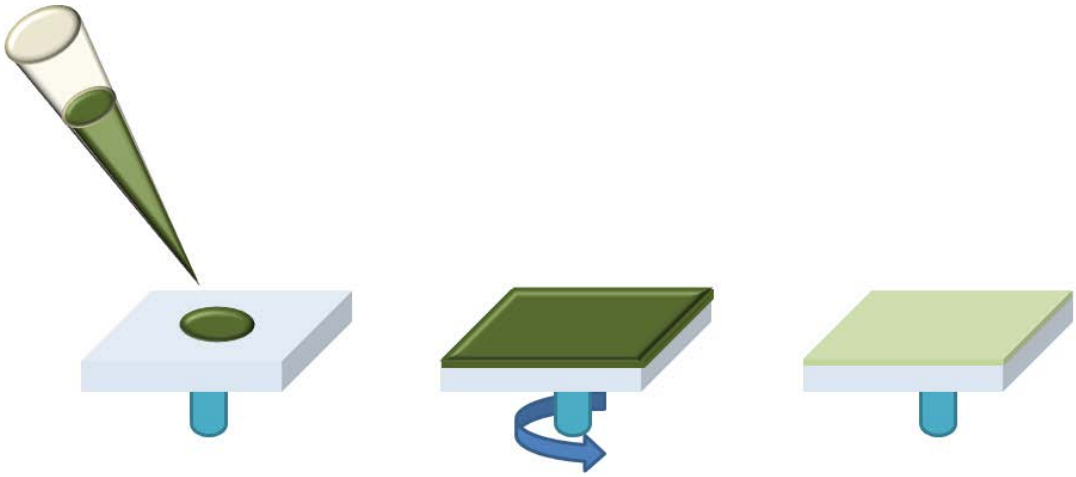

Figure 3.1: Schematic illustrating the three stages of spin coating: solution dispensing, fluid layer thinning, and solvent evaporation.

evaporation material. The current is raised until the source temperature is sufficient to cause evaporation of the material. Under good vacuum, the vaporized material has a long mean free path and travels directly to the substrate, where it condenses; therefore, a substrate may be easily patterned using a shadow mask. (An example of a shadow mask is shown in Figure 3.2 (a)). The amount of material deposited is monitored using a quartz crystal sensor, which vibrates at a specific frequency. During deposition, the vibrational frequency of the crystal changes due to the accumulation of deposited material. The frequency change is related to the mass of the deposited material. For a sensor of a given area, knowing the mass and density, one can calculate the thickness of the deposited layer.

Two deposition systems were used in this work. A bell jar was used for the deposition of metal contacts on normal architecture devices (Figure 3.2 (b)), while a second chamber, attached to an argon-filled glovebox, was used for the deposition of metal contacts on inverted architecture devices (Figure 3.2 (c)). Both vacuum chambers contain multiple evaporation sources, which are separated by metal shim stock to prevent cross-contamination between the sources. Project-specific spin coating and thermal deposition parameters are detailed, as relevant, in Chapters 4 and 5.

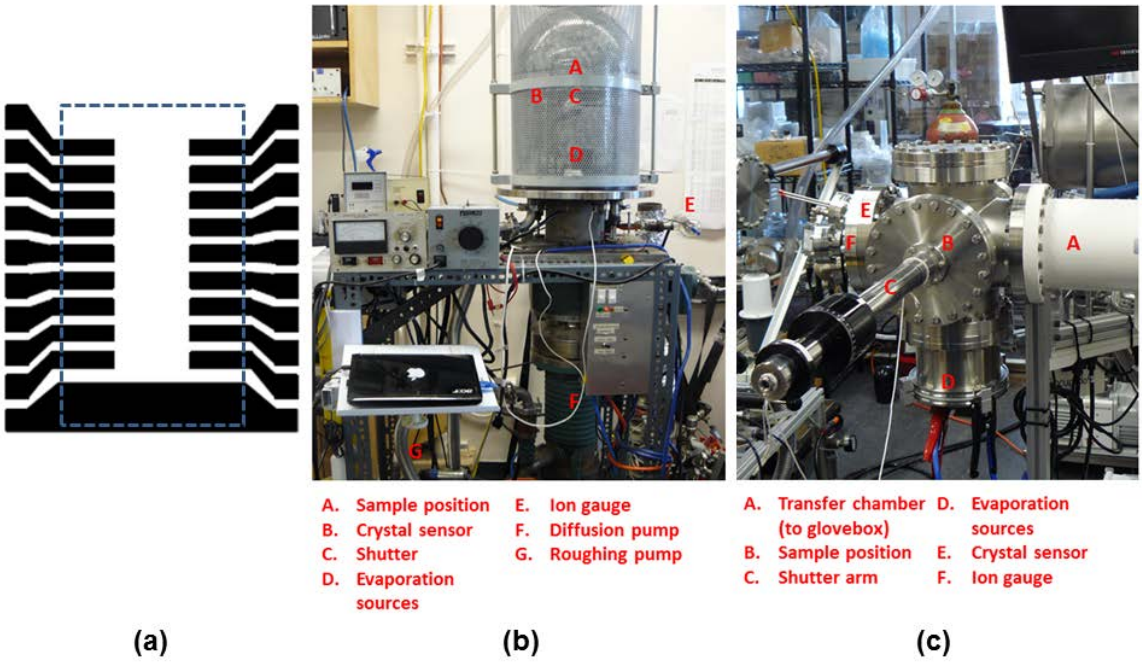

Figure 3.2: (a) An example of the shadow mask pattern used to thermally deposit metal contacts. Each finger is used to contact a single device, which gives a total of 18 devices/substrate. The active area of the device is 0.035 cm^2, as defined by the overlap between the metal contact and the ITO strip in the middle of the substrate. The location of the ITO strip is indicated by the dashed outline. (b) Photograph showing the main components of the bell jar deposition system. The main components of the second evaporation system are shown in (c).

3.2 Characterization techniques:

3.2.1 Optical microscopy:

Optical microscopy is a valuable tool for qualitatively characterizing solution processed thin films. A basic light microscope and camera can be used to identify undesirable film qualities such as over-crystallization, de-wetting, debris and other defects.

WILD Heerbrugg and Zeiss Axio Imager.A2 microscopes were used for rapid screening of solution processed thin films for further optimization. Samples were examined in transmission mode under LED illumination. Representative images of relevant films were collected using an AmScope camera and ToupView imaging software, or an AxioCam ICc5 camera and ZEN imaging software for the Heerbrugg and Axio microscopes, respectively.

3.2.2 Scanning electron microscopy

Scanning electron microscopy (SEM) is a high resolution technique that uses a focused electron beam to image a sample. The electron beam is generated by a tungsten filament, and is focused onto the sample using a combination of electromagnets. The electrons incident on the sample are known as primary electrons. A small portion of the primary electrons collide elastically with the bulk specimen, and are backscattered at large angles ($\theta > 90^o$) into the sample chamber. The probability of backscattering is proportional to the atomic number of the sample squared; therefore, the backscattered signal is sensitive to sample composition. Primary electrons may also collide inelastically with the sample, releasing secondary electrons with a lower kinetic energy. Most secondary electrons will continue to scatter inelastically within the sample, before coming to rest; however, a small portion of secondary electrons near the sample surface may be emitted into the sample chamber. Because secondary electrons are only emitted from the sample surface, the secondary electron signal is highly dependent on the sample topography. Both backscattered and secondary electrons may be detected, and are distinguished by their kinetic energy. An SEM image is formed by scanning the electron beam back-and-forth across the sample, continuously measuring the backscattered and/or secondary electron signal to generate an image.

SEM images were collected using a Phenom benchtop microscope. The particular Phenom model uses a tungsten filament, and contains detectors that are sensitive to both secondary and backscattered electrons. By consequence, the SEM images presented in this study reflect information about the sample topography, and composition.

3.2.3 Atomic force microscopy

Atomic force microscopy (AFM) is a powerful imaging technique, which can be used to characterize surface features on a nanometer scale. An atomic force microscope acquires data by using a sharp probe tip to scan back-and-forth across a surface to "feel" 3D information. The back-and-forth scanning is referred to as a rastering, and is controlled by motion of the sample stage relative to the probe tip. As the probe is rastered across a surface, the tip interacts with topographic features, and samples

the height at each location. Each height sample is recorded as a pixel, and an array of pixels can be used to generate a 2D image containing height information about the surface. The resolution of the image can be improved by increasing the number of pixels at the cost of a slower scan rate.

The AFM characterization in this work was performed using a Bruker Innova microscope, interfaced with NanoDrive software (v 8.02). The sample stage and AFM head are positioned beneath an optical microscope to allow for coarse manual adjustment of the sample with respect to the AFM tip (Figure 3.3 (a)). All characterization was performed in tapping mode using available probe tips: NCHV-A (f = 320 kHz, k = 42 N/m) and NTESPA (f = 300 kHz, k = 40 N/m). In tapping mode, the AFM probe is driven by a piezoelectric element to oscillate near its resonant frequency. Interactions between the probe tip and the sample modulate the amplitude and phase of oscillation, which is monitored by an optical lever (Figure 3.3 (b)). The system adjusts the sample height to maintain a specified oscillation amplitude, known as a setpoint. The deviation of the oscillation from the setpoint is used to adjust the tip-sample distance to restore the setpoint value, thereby inferring topographic information about the sample.

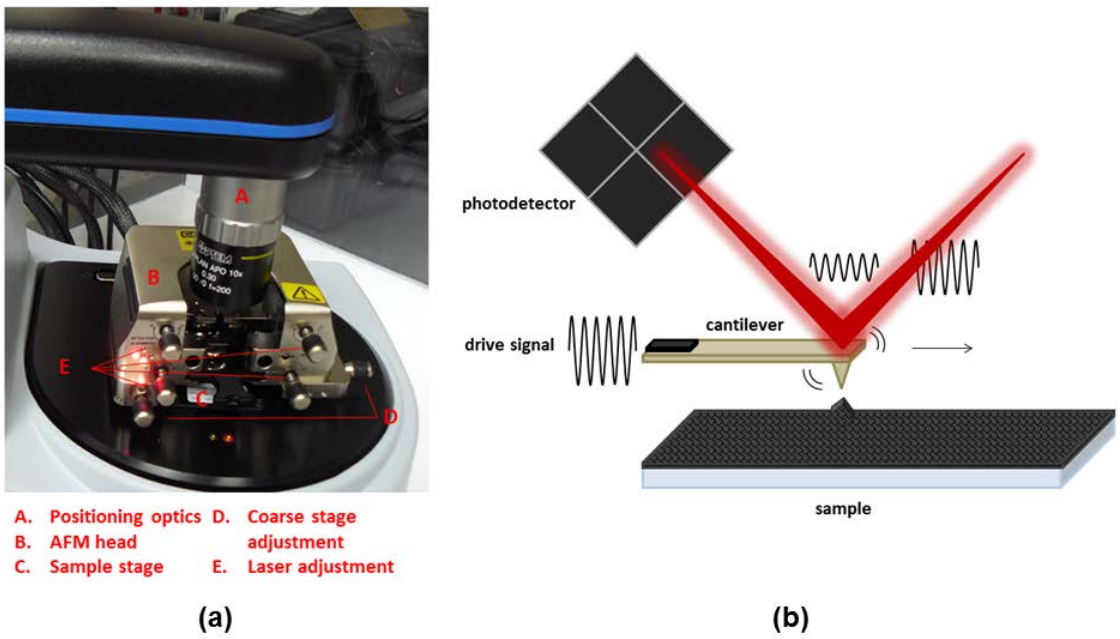

Figure 3.3: (a) A photograph indicating the main components of the Bruker Innova AFM. A schematic depicting the principles of tapping mode AFM is shown in (b).

Image post-processing was performed in NanoScope Analysis (v 1.40). Relevant image processing steps involved data levelling, filtering, and roughness calculations. Data levelling was performed using a second order polynomial to subtract the background plane. A low-pass filter was applied to smooth data when necessary. Roughness measurements were calculated using a NanoScope tool; all reported roughness measurements represent the root mean squared roughness (R_{RMS}) of the surface.

$$R_{RMS} = \sqrt{\frac{1}{n}\sum_{i=1}^{n} y_i^2} \tag{3.2}$$

3.2.4 Xray diffractometry

Among other applications, xray diffractometry (XRD) may be used to determine the composition, crystal structure, and degree of ordering in a crystalline sample. Every crystalline material has a unique diffraction pattern, which is determined by the elemental content and arrangement of atoms in the crystal lattice. In the Bragg-Brentano geometry, monochromatic xrays of wavelength λ are incident on a powder or thin-film sample as illustrated in Figure 3.4 (a). When the path length difference between adjacent lattice planes is equivalent to an integer number of λ, then constructive interference is achieved, as described by Bragg's law (Equation 3.3, Figure 3.4 (b)).

$$n\lambda = 2dsin\theta \tag{3.3}$$

The constructive interference gives rise to a peak diffraction intensity for a particular incident angle. A complete diffraction pattern is achieved for a powder sample by sweeping the xray source and detector to vary the incident angle. A diffraction pattern is typically plotted giving the detected intensity as a function of the scattering angle (2θ, Figure 3.4 (a)).

XRD patterns were measured using a Siemens D5000 diffractometer. A copper K-alpha xray source was used (λ = 1.54 Å). To facilitate comparison between various perovskite thin-films, patterns were collected using specific instrument settings. The scattering angle was measured using 0.05° increments with a 5 second dwell time. The divergence, anti-scattering and receiving slits were 0.5°, 0.5°, and 0.1 mm,

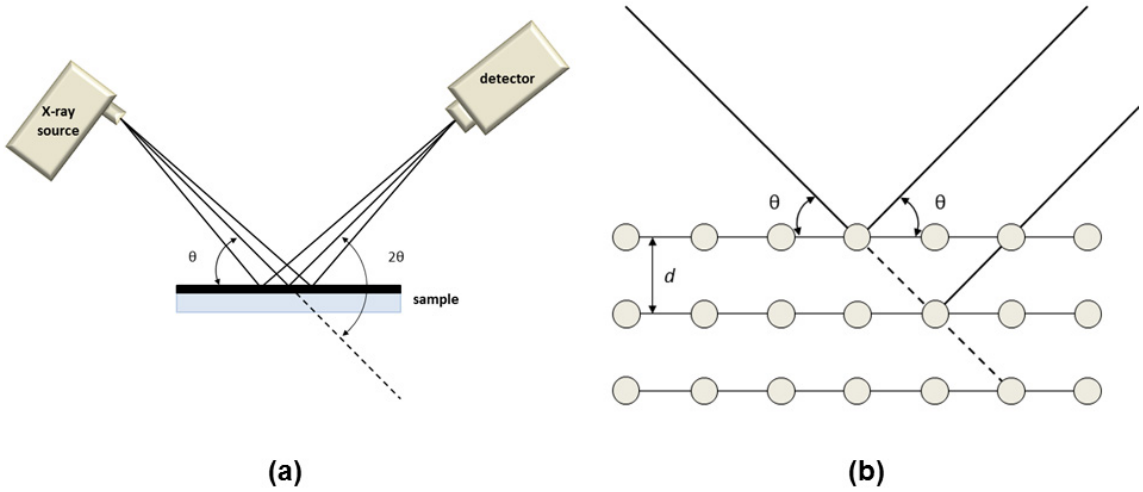

Figure 3.4: Schematics illustrating (a) the Bragg-Brentano diffraction geometry, and (b) the Bragg diffraction condition.

respectively. The perovskite diffraction pattern was collected in a scattering angle range of $2\theta = 10^{o}$ - 60^{o}.

3.2.5 UV-vis absorption spectroscopy

Absorption spectroscopy may be used to discern information about the nature of electronic transitions in a material. Light absorption enables excitation of electrons to a higher energy state, so transitions between occupied and unoccupied orbitals may appear as distinct absorption bands. Shorter wavelength light can facilitate larger energy transitions; while longer wavelength absorption corresponds to low energy transitions. The minimum excitation energy that may be absorbed corresponds to the optical bandgap of the material. Lower energy photons are not absorbed.

Absorption measurements were performed in transmission mode, using an Agilent Cary 60 spectrophotometer. A single wavelength of light from a xenon flash lamp is generated by a scanning monochromator, and is incident normal to the thin film sample. The intensity of transmitted light (I) is detected by a silicon diode and compared with the reference intensity (I_0) incident on the sample. The absorbance is calculated (Equation 3.4), and reported in absorbance units (Abs).

$$A = -\log_{10}(I/I_0) \tag{3.4}$$

The absorption measurements were automated using Agilent software (Cary Scan), programmed to scan through the desired spectral range at 300 nm/min.

3.2.6 Photoluminescence spectroscopy

Photoluminescence (PL) spectroscopy is a useful complement to absorption spectroscopy. Photoexcitation of electrons, leads to eventual decay processes when the electrons relax back into a ground state. The decay processes may occur through radiative (photoluminescence), or non-radiative pathways. The radiative emission spectrum is easily detected, and may provide useful information regarding the material bandgap and level of disorder. The intensity of PL is also a qualitative indicator of the number of non-radiative pathways in a particular material. High intensity PL, suggests a lower number of non-radiative recombination pathways.

PL measurements were performed in reflectance mode, using an Agilent Cary Eclipse spectrophotometer. A particular excitation wavelength is selected from a xenon flash lamp using a scanning monochromator. Radiative decay from the photoexcited sample is detected using a second scanning monochromator, and a photomultiplier tube. The measurement procedure was automated using Agilent software (Cary Scan), programmed to scan through the photoemission spectrum at 120 nm/min. A 520 nm excitation wavelength was used for perovskite samples.

3.2.7 Current-voltage measurements

Current-voltage measurements were performed in an argon-filled glovebox, under simulated AM1.5G sunlight at 100 mW/cm^2. The solar spectrum was generated using a xenon arc lamp in a ScienceTech solar simulator. The illumination intensity was calibrated using a reference thermopile/KG5 glass filter combination. Measurements were recorded using a Keithley 236 SMU, interfaced with a modified LabView program, originally developed by Jon-Paul Sun.

Chapter 4

Optimization of methylammonium lead iodide perovskite in a planar-structure inverted device architecture

4.1 Overview

Like most semiconductor electronics, the quality of perovskite solar cells is strongly affected by processing conditions. Among other factors, the morphology, electronic properties and photovoltaic performance of solution-processed perovskite films are known to be influenced by the choice of: fabrication atmosphere, deposition method, precursor stoichiometry, thermal treatment protocol, solvent, substrate and precursor materials [10, 26, 43, 47–60]. In addition, inherent variations between different equipment and fabrication facilities make many processing details laboratory-specific. This chapter describes the optimization of solution-processed methylammonium lead iodide perovskites within the Hill group laboratory, using a planar-structured inverted device architecture. The effects of deposition conditions, deposition method, fabrication atmosphere and precursor concentrations are described.

4.2 Experimental details

Perovskite thin films are commonly fabricated using one of two solution-processing methods: single-step deposition, or sequential-step deposition.

The single-step deposition method is considered to be the simpler of the two, as it requires only one solution-processing step [61]. The lead halide and organic halide components are dissolved in a single precursor solution, which is deposited onto the desired substrate. The precursor film is then annealed at a temperature ranging between 90 °C to 150 °C to drive the perovskite conversion [60, 62]. The phase purity of the completed perovskite film is influenced by the choice of precursor stoichiometry, annealing temperature and annealing duration [49, 55, 60]. Single-step deposition methods are most commonly employed on mesoporous substrates, which

have been found to enable higher surface coverage [39, 40, 63]; however, high-quality perovskite films have also been demonstrated on planar substrates using similar methods [8, 43, 64].

In contrast to single-step processing, sequential-step deposition is considered to enable better control over film morphology [51, 61]. The lead halide layer is first deposited from a solvent such as gamma-butyrolactone, n,n-dimethylformamide (DMF), n,n-dimethylacetamide or dimethyl sulfoxide. Since lead halides are very poorly soluble in most other solvents, the perovskite conversion is easily achieved through further solution-processing. Most commonly, the lead halide layer is immersed in a solution of the organic halide, or a layer of organic halide is spin-coated on top of the lead halide layer [10, 41]. When the organic halide layer is spin-coated, thermal annealing is required to drive the conversion to perovskite [10, 62]; however, when the lead halide film is immersed in organic halide solution, the perovskite conversion occurs at room temperature within minutes [41]. The degree of conversion achieved via solution immersion is dependent on the solution concentration and immersion duration; however, a single 60 second immersion in a 10 mg/mL organic halide solution has been reported to produce optimal device performance [41, 42, 65]. Variations of both the single-step and sequential-step deposition methods were examined in this study; the fabrication details are outlined below.

4.2.1 Perovskite film fabrication

Single-step deposition

The single-step deposition procedure employed in this study was based on that reported by Xue *et al.* [9]. A solution of methylammonium iodide (MAI), lead iodide (PbI_2) and lead chloride was mixed in anhydrous DMF, stirring at 60 °C for at least 12 hours. The precursors were mixed in a 4:1:1 molar ratio to produce a 40 wt% solution. Prior to use, the precursor solution was passed through a 0.45 µm pore filter. The perovskite layer was formed by spin-coating, 250 µL of solution onto a glass, or ITO/glass substrate coated with poly(3,4-ethylenedioxythiophene)-poly(styrenesulfonate) (PEDOT:PSS). The precursor film was then annealed in an argon-filled glovebox at 100 °C for 60 minutes. The effects of solution temperature, substrate temperature (during spin-coating) and substrate spin speed on the

resulting film morphology were examined.

It is important to note that although anhydrous solvents and precursor materials were used, all single-step solution processing was performed in an ambient environment. At the time that these experiments were performed, the effects of moisture on the photovoltaic properties of perovskite films had not been quantified; these effects are detailed in Chapter 5.

Single-step deposition with solvent washing

Solvent washing treatments are reported as an effective method to achieve compact dense perovskite films with high surface-coverage [66–68]. Effective solvent washing requires careful selection of an orthogonal solvent, in which the perovskite precursors are non-soluble. When the precursor film is washed with the orthogonol solvent during spin-coating, rapid crystal nucleation is induced and grain ripening is hindered. The resulting solvent-washed films are reported to exhibit compact crystal grains with high surface-coverage, crystallinity and photovoltaic performance [66–68]. The effect of solvent-washing was studied on the previously described single-step perovskite films using 1 mL of toluene as an orthogonal solvent. The perovskite film morphology was examined as a function of the time delay between the start of spin-coating and the solvent-wash treatment.

Sequential-step depostion: sequential spin-coating

The sequential spin-coating method used in this study was modified from a procedure reported by Xiao *et al.* [10]. A 450 mg/mL solution of lead iodide was mixed in anhydrous DMF, stirring at 70 °C for a minimum of 12 hours, to ensure dissolution. Prior to deposition, the PbI_2 solution was passed through a 0.45 µm pore filter into a clean glass vial, also held at 70 °C. A layer of PbI_2 was spin-coated at 6000 rpm onto a room-temperature PEDOT:PSS-coated substrate using 300 µL of solution. The completed film was heated on a 70 °C hotplate for 15 minutes to maximize solvent removal. A filtered solution of MAI in isopropanol was spin-coated onto the cooled PbI_2 film, and the PbI_2/MAI bilayer was annealed under argon at 100 °C for 2 hours.

The sequential spin-coating procedure was optimized both in ambient, and an argon-filled glovebox. Maximum device performance was achieved by optimizing the

concentration of the MAI solution. It is also important to note that the spin-coating duration for the PbI_2 film was significantly increased for fabrication under argon, in which the lead iodide film was observed to dry up to 6 times slower. This observation is supported by other work [69]. Under argon, the lead iodide spin duration was increased to 6 minutes (from 1 minute in ambient).

4.2.2 Device fabrication and measurement

Inverted architecture devices

Inverted architecture perovskite devices were fabricated on patterned ITO-coated glass substrates. The substrates were cleaned by scrubbing with detergent and de-ionized (DI) water, then ultrasonicating in baths of detergent, DI water, acetone and ethanol for 20 minutes each. Finally, the substrates were treated with UV-ozone for 20 minutes. The PEDOT:PSS hole transport layer was formed in air by spin-coating 90 µL of filtered PEDOT:PSS (Clevios AI 4083) onto each ITO substrate at 3000 rpm for 60 s. The films were annealed at 140 °C for 60 minutes. The perovskite layer was completed as detailed previously, either in ambient, or an argon-filled glovebox. Following perovskite fabrication, the [6,6]-phenyl-C61-butyric acid methyl ester (PCBM) electron transport layer was formed. A 70 °C solution of PCBM (30 mg/mL in chlorobenzene) was spin-coated onto the cooled perovskite films at 1000 rpm for 180 seconds. When devices were made under argon, the PCBM layer was annealed at 100 °C for 45 minutes [70]. The devices were completed by thermally depositing 15 nm of calcium and 100 nm of aluminum at a base pressure of $\sim 10^{-6}$ Torr. For devices fabricated in ambient, a 40 mg/mL solution of PCBM was used. The PCBM layer was not annealed, and devices were completed with a top contact containing 0.5 nm of lithium fluoride and 100 nm of aluminum.

The thicknesses of the PEDOT:PSS, perovskite and PCBM layers for the devices were estimated to be 50 ± 5 nm, 280 ± 70 nm and 80 ± 10 nm, respectively, using a Dektak profilometer. (The reported uncertainties represent the standard deviation of 9 measurements). The area of the completed devices was 0.035 cm^2 or 0.04 cm^2, depending on the ITO pattern. Current density-voltage (JV) data of completed devices were measured under 100 mW/cm^2 simulated AM1.5G sunlight using a ScienceTech solar simulator, and a Keithley 236 SMU. The illumination

intensity was verified using a calibrated thermopile/KG5 glass filter combination.

Normal architecture devices

Normal architecture devices were produced following a procedure described by Liu and Kelly [42]. The devices were fabricated on glass substrates coated with fluorine-doped tin oxide (FTO). The substrates were cleaned by scrubbing with detergent and de-ionized (DI) water, then ultrasonicating in baths of detergent, DI water, acetone and ethanol for 20 minutes each. Finally, the substrates were treated with UV-ozone for 20 minutes. Three coats of zinc oxide nanoparticles were cast onto the cleaned FTO, spinning at 3000 rpm for 60 seconds. For each coat, 0.3 mL of a filtered nanoparticle suspension (6 mg/mL in n-butanol, chloroform and methanol) was used. The zinc oxide films were baked at 120 °C for 5 minutes between each coat. The perovskite layer was formed using another sequential-step deposition method. A layer of PbI_2 was spin-coated on the completed zinc oxide at 3000 rpm for 60 seconds, using 0.3 mL of filtered 1 M solution. To maximize surface coverage, both the solution and substrate were held at 70 °C prior to deposition. The completed lead iodide film was cooled, pre-wetted with isopropanol for 2 seconds, and immersed in a solution of MAI (10 mg/mL in isopropanol). The substrate was removed after 60 seconds, rinsed with isopropanol and dried under a stream of filtered compressed air. A layer of doped spiro-OMeTAD (80 mg/mL in chlorobenzene) was spin-coated at 4000 rpm for 90 seconds, using 0.2 mL of filtered solution. For each milliliter of spiro-OMeTAD solution, 28.5 µL of 4-*tert*-butylpyridine and 17.5 µL of lithium-bis(trifluoromethanesulfonyl)imide (520 mg/mL in acetonitrile) dopants were added [42]. The devices were completed with 150 nm of silver, thermally deposited at a base pressure of $\sim 10^{-6}$ Torr. The active area of the completed devices was 0.0277 cm^2.

Zinc oxide nanoparticle synthesis

The zinc oxide nanoparticles were fabricated using an established hydrolysis and condensation method as described by Liu *et al.* [42]. Zinc acetate dihydrate (0.295 g) was dissolved in 12.5 mL of methanol, stirring at 65 °C. A solution of potassium hydroxide (0.148 g in 6.5 mL of methanol) was added to the zinc acetate solution,

dropwise with stirring. The potassium hydroxide solution was introduced over the course of 15 minutes. The mixture was stirred rapidly at 65 °C for 2.5 hours. The cooled reactants were centrifuged at 4750 rpm for 30 min, decanted and rinsed with 2 mL of methanol. The centrifuge and rinsing step was repeated twice. The final suspension was formed by adding 7 mL *n*-butanol, 0.5 mL methanol and 0.5 mL of chloroform to the precipitate to produce a 6 mg/mL nanoparticle solution. The particle radius was measured using AFM to be approximately 25 nm. This is comparable to the AFM tip radius, and therefore the actual particles may be smaller.

4.3 Results and discussion

4.3.1 Effect of spin-coating conditions on film morphology and performance

A well-functioning photovoltaic device must generate and separate charge. High surface-coverage by the active layer(s) is needed to maximize photon absorbance and maintain the rectification properties of the device (e.g. Figure 4.2 (b)). Voids through the device will result in lowered carrier generation, and serve as shunt pathways, allowing photogenerated charge carriers to recombine. By consequence the established photovoltage and the net harvestable current will be reduced.

The perovskite film morphology was found to be highly sensitive to solution-processing conditions, particularly when single-step deposition methods were used. Figure 4.1 illustrates the effect of substrate spin speed on the morphology of single-step perovskite films. Because DMF is a high boiling-point solvent (152 °C), low spin speeds were found to result in slow solvent evaporation, allowing preferential crystal nucleation and ripening. Perovskite films spun at 1000 rpm contained large crystal domains, greater than 10 µm across (Figure 4.1 (a)); however, the surface-coverage was low, with up to 10 µm of separation between perovskite domains. Higher rotational velocities were found to increase the rate of solvent evaporation, in turn causing rapid crystal nucleation and limited grain ripening (Figure 4.1 (c)). At 4000 rpm, the perovskite domains were limited to 3 µm in size, and higher surface coverage was achieved.

Barring equipment limitations, the maximum feasible spin speed is restricted by

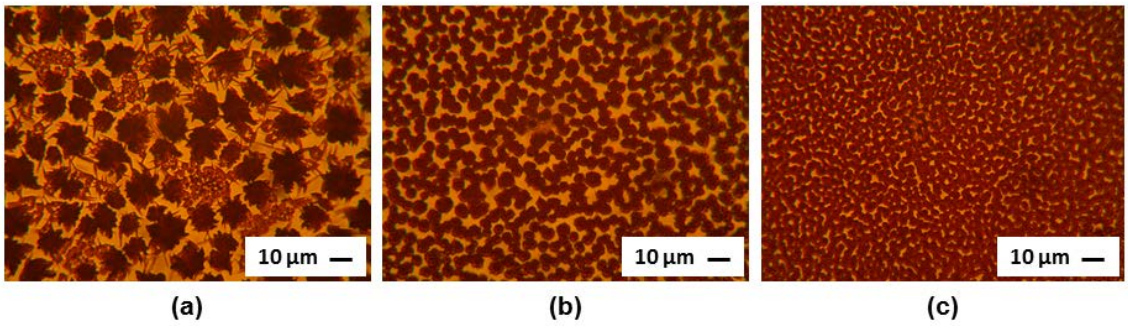

Figure 4.1: Optical microscope images of perovskite films spun onto PEDOT:PSS using a single-step deposition method precursor. Films were made by spinning at (a) 1000 rpm, (b) 2000 rpm and (c) 4000 rpm. Scale bars represent 10 µm. The images were collected using bottom illumination; the darker regions correspond to the perovskite domains.

the resulting film thickness, which decreases at higher rotational velocities (Equation 3.1). When the absorbing layer is too thin, photon absorption is reduced. To maintain the perovskite layer thickness while increasing the rate of DMF evaporation, the precursor solution and substrates were heated. Figure 4.2 illustrates the effect of solution temperature on the resulting perovskite film. When the solution temperature was increased to 60 °C, the substrate coverage was dramatically improved; however, micrometer-sized voids were still evident by scanning electron microscopy (Figure 4.3 (a)). When the substrate temperature was also increased to 60 °C, the number of large voids was substantially reduced (Figure 4.3 (b)).

It was unclear from SEM images whether the features in Figure 4.3 represented pinholes through the entirety of the perovskite layer; in this regard, the current density-voltage data was more revealing. Figure 4.4 shows two JV-curves corresponding to perovskite devices prepared by spin-coating a 60 °C precursor solution at 4000 rpm onto a room-temperature and a heated substrate. In both cases, the JV measurements show weak diode behaviour that is linear through the origin, suggesting that numerous shunt pathways remained throughout the perovskite layer. The lowered shunt resistance of the device would account for the resistive contribution to the JV behaviour.

To improve substrate coverage by the perovskite layer, a toluene solvent-wash

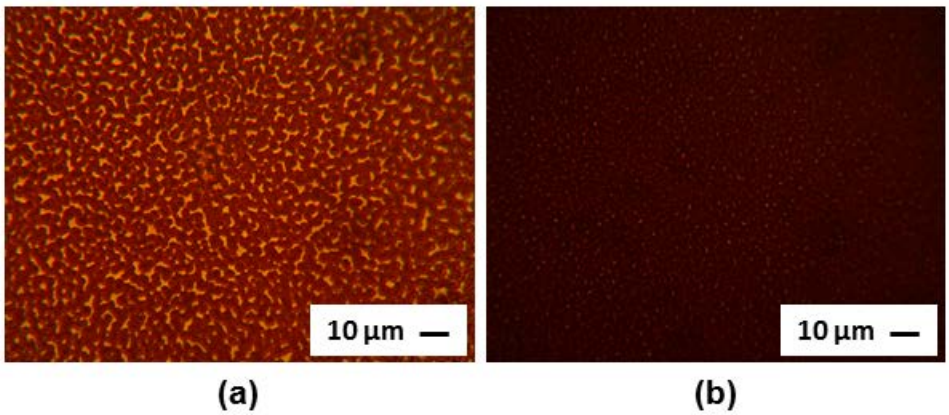

Figure 4.2: Optical microscope images of perovskite films spun from a single-step precursor onto a room temperature PEDOT:PSS-coated substrate. Films were spun at 4000 rpm using (a) a room temperature solution, and (b) a 60 °C solution. Scale bars represent 10 µm. The images were collected using bottom illumination; the darker regions correspond to the perovskite domains.

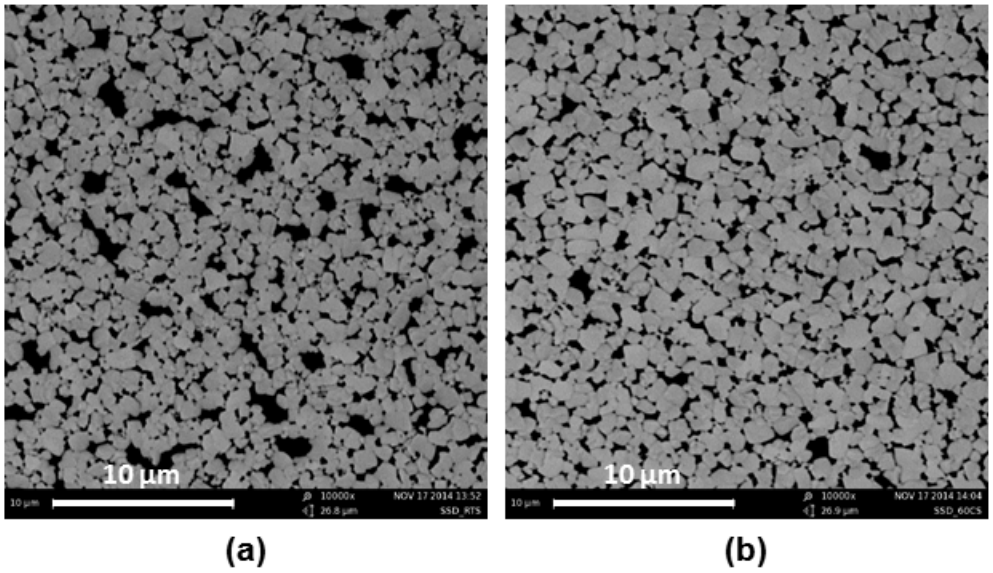

Figure 4.3: Scanning electron microscope images of perovskite films spun from a 60 °C precursor solution onto (a) a room temperature, and (b) a 60 °C PEDOT:PSS-coated glass substrate. Scale bars represent 10 µm.

treatment was incorporated into the previously described single-step deposition procedure. The delay time between when the precursor solution was cast and when the solvent-wash was performed was varied between 7 - 35 seconds (as measured using a stopwatch). Figure 4.5 shows the strong relationship between the perovskite film

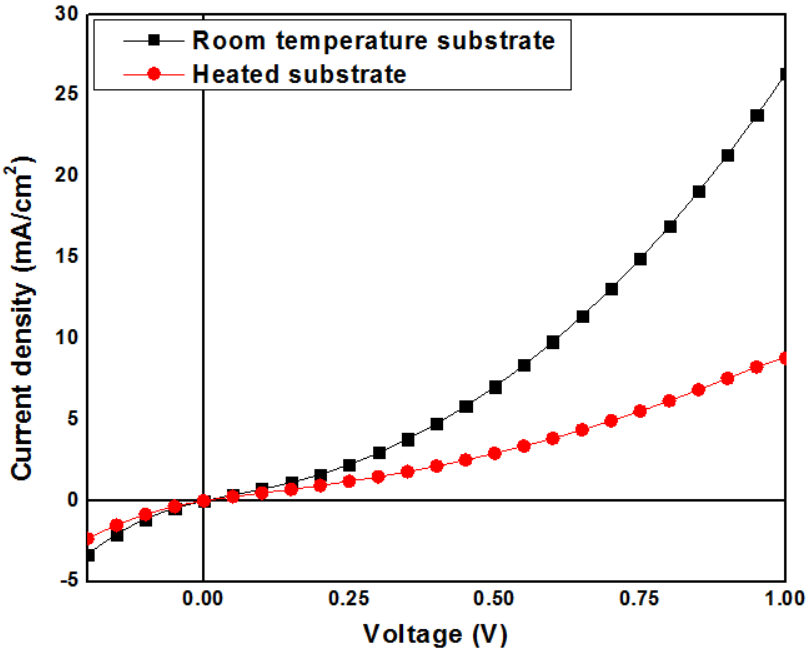

Figure 4.4: JV-curves for inverted architecture perovskite devices deposited using a single-step method on a room temperature and heated substrate.

morphology and the solvent-wash timing. As expected, smaller crystal grains were observed when rapid crystallization was induced; however, as the delay time was increased, the crystal grains began to cluster into wetted and non-wetted domains (Figure 4.5 (d-e). The high-sensitivity of the film morphology to the solvent-wash timing is illustrated in Figure 4.6; both films were fabricated with a 7 second delay before solvent-washing. It is clear that in some instances, the morphology of solvent-washed films was greatly improved, with localized regions even resembling films in published studies [66]; however, the washing treatment was poorly reproducible. Furthermore, the macroscopic film quality was worsened by solvent-washing, which caused localized damage where the solvent was dispensed, and cracking in the final film.

4.3.2 Effect of deposition method

Despite various modifications made to the single-step deposition procedure, reproducible uniform perovskite films were not achieved. In contrast, similar modifications to a sequential deposition procedure produced high surface coverage perovskite films

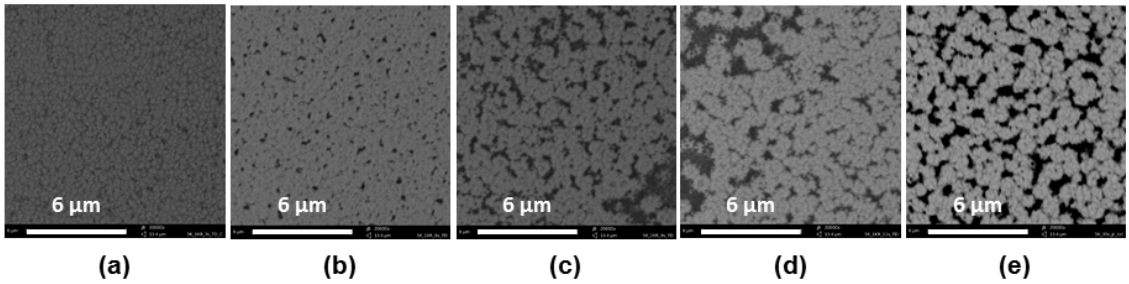

Figure 4.5: Scanning electron microscope images of perovskite films spun using a toluene solvent-wash treatment on a single-step precursor film. The time delay before the solvent-wash was (a) 7 s, (b) 8 s, (c) 9 s, (d) 11 s, and (e) 35 s. Scale bars represent 10 µm.

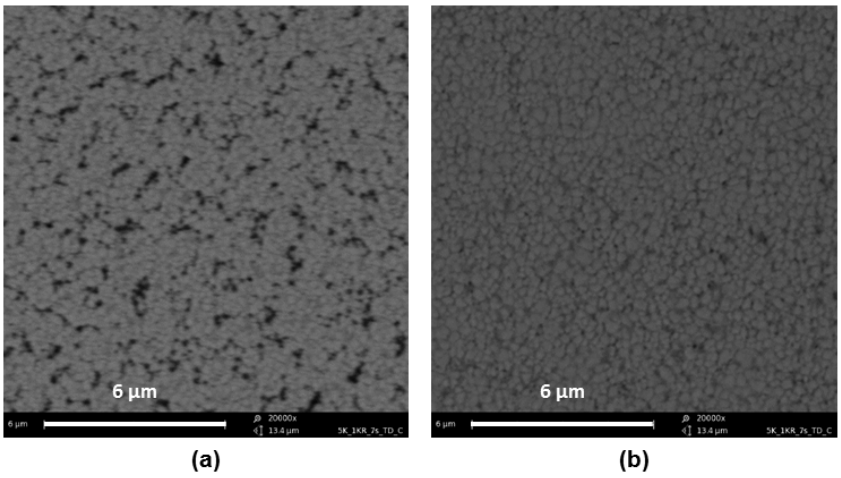

Figure 4.6: Scanning electron microscope images of perovskite films spun using a toluene solvent wash treatment on a single-step precursor film. The time delay before the solvent wash treatment was 7 s in each image. The scale bar represents 6 µm.

with excellent photovoltaic performance. Figure 4.7 (a) shows several JV curves from normal architecture devices, fabricated using a sequential deposition method (Figure 4.7). (The deposition method was modified from published studies as previously detailed [41, 42]). The resulting devices showed strong performance, with an average V_{oc} of 0.99 ± 0.02 V and J_{sc} of 23.6 ± 0.5 mA/cm^2 (Table 4.1). The highest measured device efficiency was 13.4 %, which is competitive with some of the highest performances reported using similar fabrication methods [41, 42]. A top-view SEM image is shown in Figure 4.7 (b), illustrating the crystalline morphology that was

achieved through control of the solution and substrate temperatures.

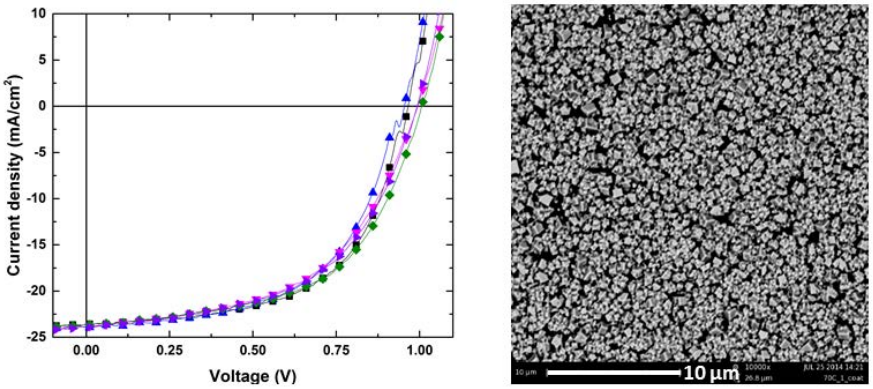

Figure 4.7: JV curves for a set of normal architecture perovskite devices fabricated by sequential deposition (a). A top-view SEM image illustrating the crystalline morphology of the perovskite layer is shown in (b).

Table 4.1: Performance summary for a set of normal architecture perovskite devices fabricated by sequential deposition. Uncertainties represent the maximum deviation from the average within the group of six devices.

	PCE (%)	V_{oc} (V)	J_{sc} (mA/cm^2)	FF
Average	12.7 ± 0.7	0.99 ± 0.02	23.6 ± 0.5	0.54 ± 0.03
Maximum	13.4	1.01	24.0	0.58

Given the overwhelming experimental evidence favouring the morphology and performance of sequentially-deposited perovskites, the single-step deposition method was discontinued. Instead, a sequential spin-coating deposition method was adopted, based on several studies that had shown reproducible, high-efficiency perovskite devices in an inverted architecture [10, 62, 71]. With no optimization, the sequential spin-coating procedure yielded reproducible perovskite films with excellent surface coverage. Figures 4.8 (a) and (b) show top-view SEM images of two separate perovskite films fabricated using the same reported procedure; both films are visually identical, and exhibit a compact planar morphology. Figure 4.8 (c) shows JV curves corresponding to perovskite devices fabricated using the same sequential spin-coating method, with no optimization. The photovoltaic performance of the measured devices was modest, with an average PCE of 3.11 ± 0.2 % (Table 4.2). The JV behaviour was greatly improved in comparison to the single-step fabrication method,

but continued to exhibit resistive contributions. The abnormally low V_{oc} and J_{sc} suggest that device performance was limited by carrier recombination. Although the average device performance was substantially lower than reported in the original studies [10, 62, 71], the morphology of the perovskite films demonstrated strong potential for improvement with further optimization.

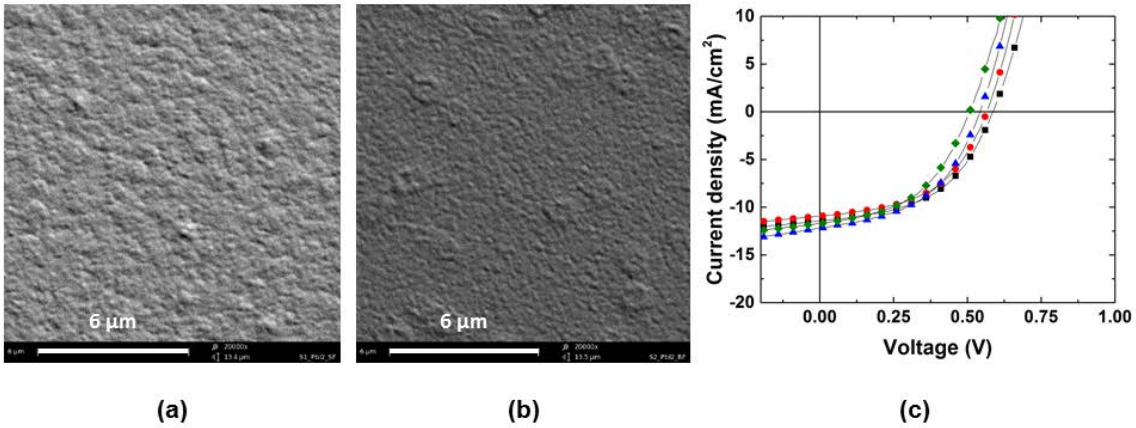

Figure 4.8: Top-view SEM images of unoptimized sequentially spin-coated perovskite films (a & b), illustrating the reproducible, compact morphology of two separate samples. The JV curves in (c) are the first devices made using the unoptimized procedure.

Table 4.2: Performance summary for a set of inverted architecture perovskite devices fabricated by sequential spin-coating. Uncertainties represent the maximum deviation from the average in the group of four devices.

	PCE (%)	V_{oc} (V)	J_{sc} (mA/cm^2)	FF
Average	3.1 ± 0.2	0.56 ± 0.04	11.6 ± 0.6	0.48 ± 0.01
Maximum	3.3	0.59	12.2	0.50

4.3.3 Optimization of ambient fabrication conditions

Following the preliminary device results, further improvements in photovoltaic performance were achieved by tailoring the perovskite layer thickness and the concentration of MAI precursor solution.

The effect of MAI concentration on device performance is illustrated in Figure 4.9 (a). A MAI solution concentration of 50 – 60 mg/mL was found necessary to

produce any substantial photocurrent. Figure 4.9 (b) shows the corresponding x-ray diffraction patterns for perovskite films prepared using 40 mg/mL, 50 mg/mL and 60 mg/mL MAI solutions. An increase in the relative intensity of the (001) PbI_2 diffraction peak was observed in films fabricated with lower concentrations of MAI solution, suggesting a larger PbI_2 phase presence. This trend is anticipated to continue for lower MAI concentrations, and likely accounts for the reduced photocurrent at these concentrations. The wide bandgap PbI_2 phase ($\sim$ 2.3 eV, [72]) is expected to limit photon absorption and contribute to series resistance within the perovskite film.

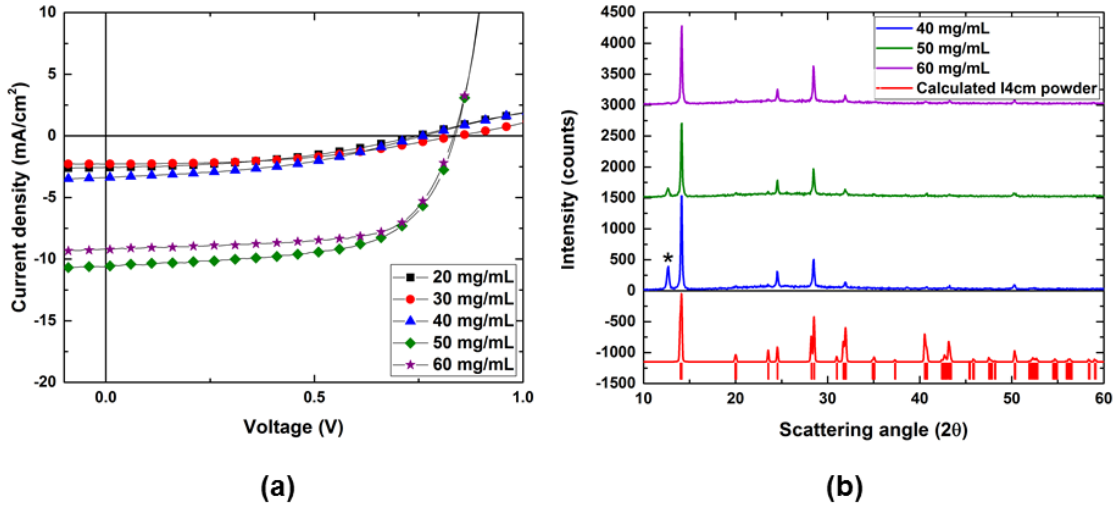

Figure 4.9: *JV* curves illustrating the effect of MAI solution concentration on the performance of sequentially spin-coated perovskite devices (a). The x-ray diffraction patterns corresponding to the higher performing devices are shown in (b). The calculated *I4cm* powder diffraction pattern and peak positions are indicated in red. The position of the (001) PbI_2 diffraction peak is indicated by the asterisk.

Using a 60 mg/mL solution of MAI, the effect of perovskite layer thickness on device performance was also examined. The perovskite layer thickness was adjusted by varying the spin speed of the substrate during the sequential spin-coating procedure. Figure 4.10 shows the *JV* curves for devices made using three perovskite layer thicknesses. The overall effect of thickness on device performance, however, is minimal. A slight increase in the short circuit current density was observed, likely resulting from increased photon absorbance; but, the lower fill factor of thicker devices

resulted in decreased photovoltaic performance. The maximum PCE was measured to be 8.8 %, from a 235 nm thick perovskite layer.

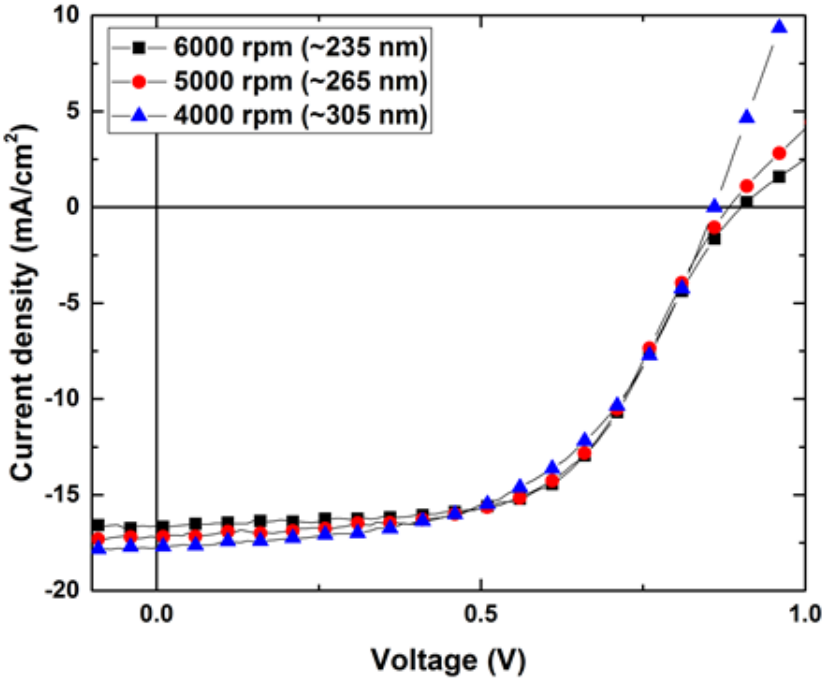

Figure 4.10: JV curves illustrating the minimal dependence of photovoltaic performance on perovskite film thickness for devices fabricated by sequential spin-coating in an ambient atmosphere.

4.3.4 Effect of fabrication atmosphere

Despite substantial improvement in photovoltaic performance, the overall device efficiencies remained low in comparison to published methods [10, 62]. In addition, the JV behaviour of the devices was found to be highly variable, both across a single substrate and between "identically" prepared substrates. Figure 4.11 (a) shows the JV performance of 17 devices fabricated under ambient conditions, on a single substrate. A large spread in V_{oc} is observed, ranging from 0.46 to 0.81 V. The spread in fill factor and J_{sc} are similarly large, and a maximum PCE of only 5.5 % is achieved (Table 4.3). Figure 4.11 (b) summarizes the batch-to-batch variation between the maximum performing devices on identically prepared substrates. The V_{oc} and fill factor are especially varied, ranging from 0.81 to 0.92 V and 0.55 to 0.58, respectively.

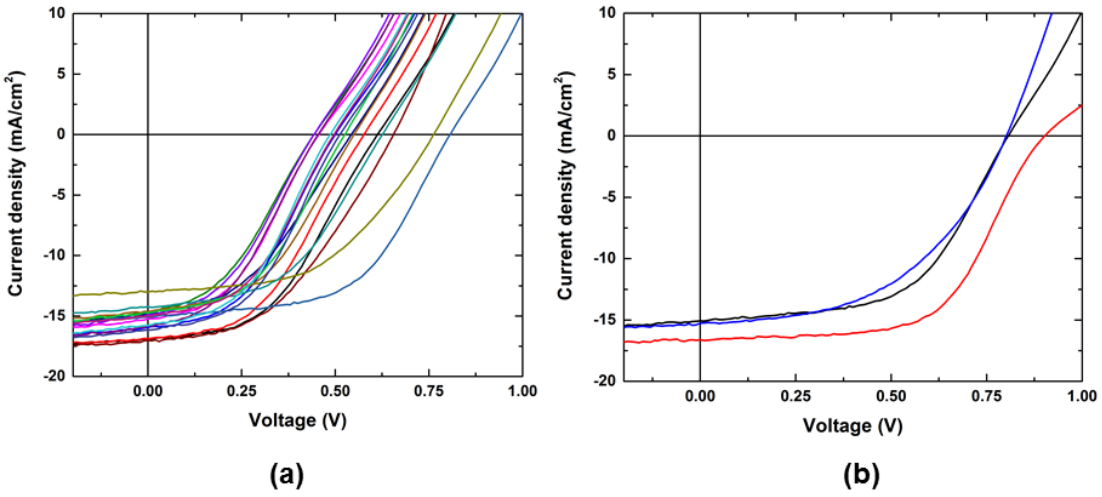

Figure 4.11: JV curves exemplifying the high performance variability of sequentially spin-coated perovskite devices prepared in ambient. Shown in (a) are JV curves from 17 devices on a single substrate. The highest efficiency device on three identically prepared substrates is shown in (b), each prepared approximately one week apart.

Table 4.3: Performance spread for a set of inverted architecture perovskite devices fabricated by sequential spin-coating under ambient conditions. Uncertainties represent the standard deviation of the mean.

	PCE (%)	V_{oc} (V)	J_{sc} (mA/cm^2)	FF
Average	3.5 ± 0.2	0.57 ± 0.03	14.2 ± 0.4	0.44 ± 0.01
Maximum	5.5	0.81	17.0	0.55
Minimum	2.5	0.46	11.7	0.38

In addition to the inconsistent device performance, many of the perovskite films were found to exhibit variable surface textures when fabricated using identical procedures (Figure 4.12). The film in Figure 4.12 (a) contains numerous ridge-like features, which exceed 200 nm in height. In contrast, the film in Figure 4.12 (b), exhibits a planar morphology with a significantly lower root mean square roughness (18.2 nm, in comparison with 54.4 nm). The variable surface roughness is thought to be the most likely cause for the inconsistent device performance. Given the surface feature height in Figure 4.12 (a), the perovskite is likely to protrude through the PCBM layer in certain places. Without the charge-selective PCBM layer, increased recombination would occur at the perovskite-metal interface, resulting in a lowered photocurrent and open-circuit voltage. The degree of recombination would depend

on the roughness of the perovskite layer, which would explain the high JV variability between devices.

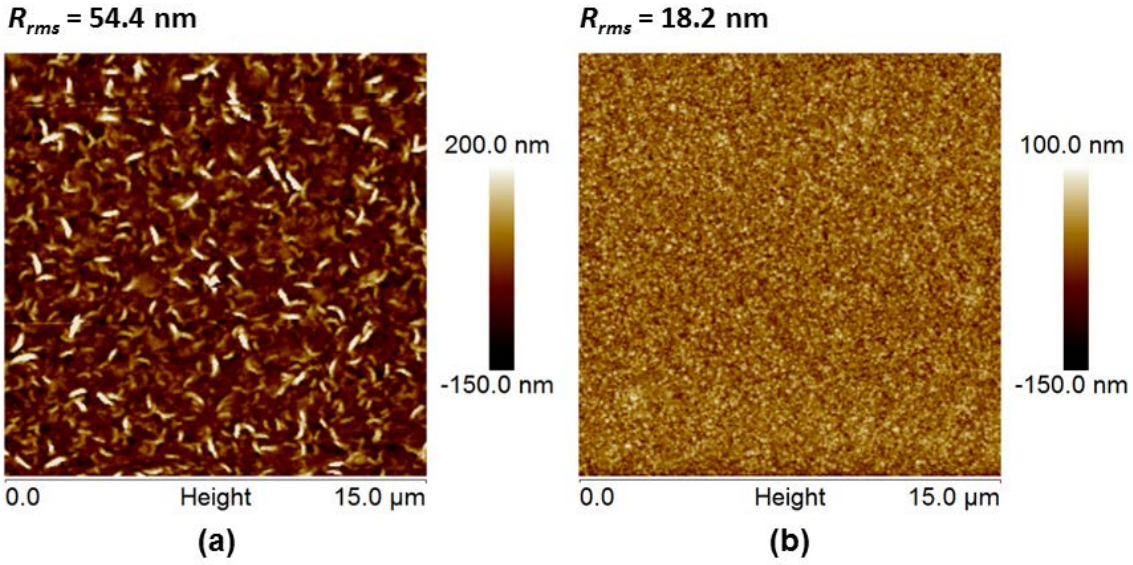

Figure 4.12: AFM images illustrating the variable grain structure of perovskite films prepared by identical sequential spin-coating methods in an ambient environment.

The large difference in film morphology illustrated in Figure 4.12 was speculated to originate from uncontrolled humidity conditions during ambient fabrication. The ridge-like structures, shown in (a) are resemblant of those reported for PbI_2-rich films [73, 74]. It has been speculated that high ambient humidity favours rapid precipitation of small PbI_2 domains, and that the smaller domains enable more facile incorporation of MAI into the PbI_2 lattice [73]. It is possible that the film in Figure 4.12 (b) was fabricated under higher humidity conditions; however, the ambient humidity was not quantitatively recorded at the time.

To reduce uncertainty surrounding the fabrication atmosphere, all further perovskite fabrication was performed in an argon-filled glovebox. With little optimization, the fabrication under argon was observed to produce higher fill factor devices with lower performance variability across a given substrate (Figure 4.13 (a)). Fabrication under inert gas was also observed to yield a less variable surface texture (Figures 4.13 (b) & (c)). It is important to note that the AFM images presented in Figure 4.13 represent perovskite films fabricated in a nitrogen-filled glovebox. Nitrogen has been shown to elicit significantly faster solvent evaporation than argon [69]; however,

no AFM data was collected when argon was used as an inert gas. It is likely that the morphology presented in Figure 4.13 is not representative of that produced by fabrication under argon; but, the repeatable surface texture from sample-to-sample is noteworthy.

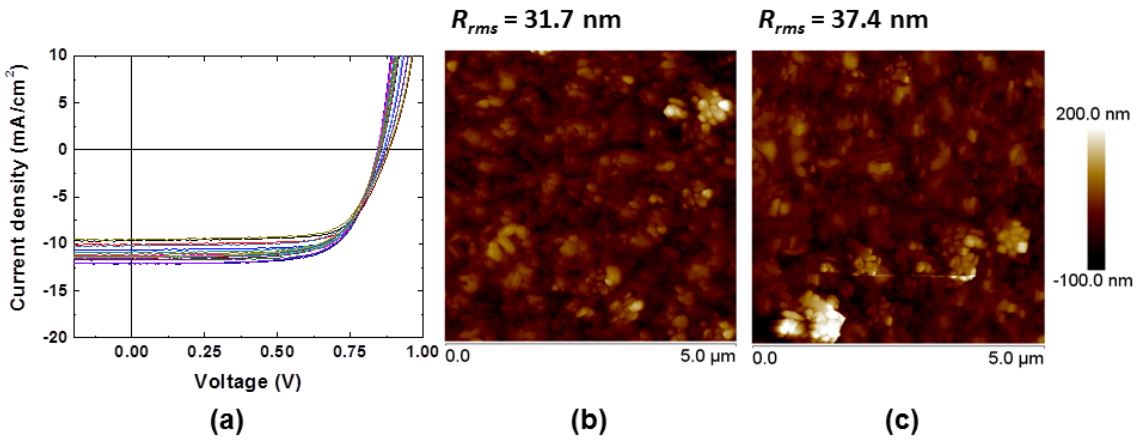

Figure 4.13: JV data for perovskite devices fabricated by sequential spin-coating in an argon-filled glovebox (a). Each JV trace represents one of 18 devices fabricated on a single substrate. AFM images in (b) and (c) illustrate the more consistent surface texture of sequentially spin-coated films prepared in an inert environment.

4.3.5 Effect of precursor stoichiometry

The electronic properties of methylammonium lead iodide perovskites are strongly influenced by the film stoichiometry and preparation method [26, 75]. Hall effect measurements have shown that the perovskite doping character is determined by the relative precursor content of the final film, where an excess of MAI produces p-type qualities and an excess of PbI_2 produces n-type qualities [75]. X-ray photoelectron spectroscopy (XPS) and ultraviolet photoelectron spectroscopy have also shown that the ionization energy is similarly affected; films with a higher relative organic (MAI) content have a lower ionization energy, by up to 0.7 eV [26]. Since the optical bandgap of the perovskite is unchanged, the shift in ionization energy is also accompanied by a shift in electron affinity. The sensitivity of the perovskite band energies to precursor stoichiometry is an issue of consierable importance, as improper band alignment between the perovskite and charge selective transport layers could result in charge

extraction barriers, severely reducing device performance. Therefore, determination of the correct precursor stoichiometry is paramount in achieving high-performance devices.

Systematic work has shown that the ionization energy is dependent not only on the composition, but also the processing condition of the perovskite film [26]. As a result, structural characterization alone is insufficient to identify ideal fabrication conditions. X-ray diffraction and XPS studies have shown that few structural differences are observable with varying composition, even when one of the precursors is incorporated in large excess [26, 75]. It is suggested that non-stoichiometries do not necessarily contribute to additional phases, but may be incorporated at interstitial sites, making them undetectable by XRD [26]. Furthermore, a small amount of residual PbI_2 has been reported to have a passivating effect on perovskite grain boundaries and interfaces, resulting in improved device performance [72, 76, 77].

To optimize perovskite fabrication in an argon-filled glovebox, photovoltaic performance was examined as a function of the reactant availability. The thickness of the PbI_2 was held constant, and the availability of MAI to the perovskite film was varied with the concentration of MAI solution (40 – 50 mg/mL). Figure 4.14 (a) shows the JV curves from the highest performing devices fabricated using a range of MAI concentrations. As shown in Table 4.4, a maximum PCE of 9.8 % was achieved using a 47.5 mg/mL solution of MAI. Below 47.5 mg/mL, lower device performance was observed. The lowest performance using a 45 mg/mL solution is likely an abnormality, possibly resulting from an error in the fabrication procedure. The reduced performance at lower MAI concentrations, however, is in agreement with the higher ionization energies reported in MAI-deficient films [26]. If the perovskite ionization energy is sufficiently raised, an injection barrier would be formed at the perovskite/PCBM interface, hindering carrier extraction. Above 47.5 mg/mL, increased MAI content in the perovskite layer resulted in a dramatic loss of photogenerated current. It is possible that the additional MAI may have induced p-type doping in the perovskite layer, thereby increasing the majority carrier concentration. A higher carrier concentration could result in increased carrier scattering in the perovskite layer, which would reduce the net current that is extracted [75]. It is also possible that if the spin-coated MAI layer was too thick, then a layer of residual

MAI may remain at the perovskite-PCBM interface after annealing. Since MAI is thermally stable until 245 °C, it is unlikely for residual MAI to be removed during the annealing phase [56].

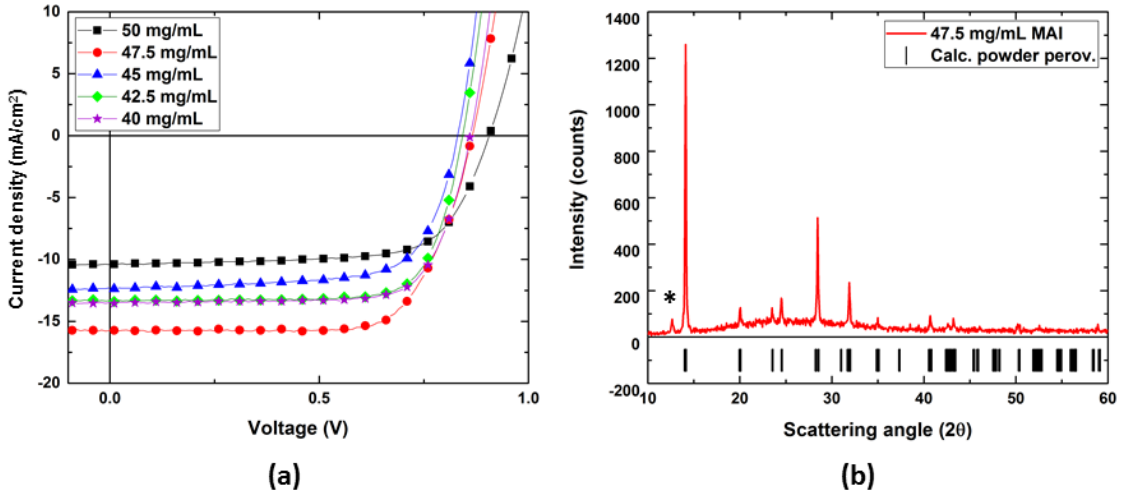

Figure 4.14: *JV* curves for inverted architecture perovskite devices fabricated by sequential spin-coating under argon (a). The *JV* traces represent the highest performing device made with each concentration of MAI precursor. Measurements were performed using a 0.1 V/s sweep rate. The XRD pattern corresponding to the highest performing MAI concentration is shown in (b). The (001) PbI_2 peak position is indicated with an asterisk.

It is interesting to note that the maximum device performance was not achieved using phase-pure perovskite. A XRD pattern of an equivalently fabricated perovskite film is shown in Figure 4.14 (b), highlighting the presence of the (001) PbI_2 diffraction peak at 12.63°. This observation is in alignment with other studies that report on the passivation of perovskite grain boundaries by residual PbI_2 [72, 76, 77]. XPS studies have also reported improved photovoltaic performance in slightly PbI_2-rich devices, even when no crystalline PbI_2 is evident [26].

4.4 Conclusions

The results of this investigation strongly favour the use of sequential deposition methods in order to achieve high efficiency planar-structured perovskite devices. In comparison with single-step methods, the sequential spin-coating procedure was found

Table 4.4: Performance summary for sequentially spin-coated perovskite devices processed under argon with varying concentrations of MAI precursor. The devices were measured using a 0.1 V/s sweep rate. Uncertainties represent the standard deviation of the mean for each fabrication condition. The figures in parentheses represent the highest value achieved for each figure-of-merit.

[MAI] (mg/mL)	PCE (%)	V_{oc} (V)	J_{sc} (mA/cm^2)	FF
40	8.2 ± 0.1	0.876 ± 0.003	12.7 ± 0.1	0.741 ± 0.005
	(8.7)	(0.898)	(13.5)	(0.762)
42.5	7.6 ± 0.2	0.821 ± 0.008	12.3 ± 0.2	0.752 ± 0.003
	(8.6)	(0.857)	(13.4)	(0.772)
45	6.5 ± 0.1	0.804 ± 0.004	12.2 ± 0.1	0.667 ± 0.006
	(7.2)	(0.849)	(13.1)	(0.714)
47.5	9.0 ± 0.1	0.873 ± 0.003	14.7 ± 0.2	0.697 ± 0.007
	(9.8)	(0.889)	(16.3)	(0.740)
50	5.8 ± 0.1	0.918 ± 0.003	9.2 ± 0.2	0.688 ± 0.003
	(6.6)	(0.941)	(10.4)	(0.708)

to easily produce compact dense perovskite films with high surface-coverage. By exercising careful control of the fabrication atmosphere and precursor stoichiometry, a maximum PCE of 9.8 % was achieved in an argon-filled glovebox. This figure is not among the highest efficiencies reported using similar fabrication methods [10,62]; but, it is competitive with many other reports for planar structured inverted architecture devices [11, 12, 26, 78, 79].

Chapter 5

The impact of water on the formation and performance of perovskite photovoltaics

The content of this chapter has been published in RSC Advances and is reproduced from Ref. [80] with permission from the Royal Society of Chemistry.

5.1 Overview

The stability of any emerging technology is always a serious concern. Methylammonium lead iodide perovskites have long been known to be extremely sensitive to liquid water, degrading irreversibly to lead iodide through the removal and eventual decomposition of the methylammonium cation [81, 82]. Perovskite degradation under ambient humidity, however, is reported to be at least partially reversible via the formation of an intermediate hydrate phase [83, 84]. For example, Leguy *et al.* documented the evolution in photovoltaic performance for perovskite device under ambient humidity. Upon exposure to a humid environment, a 90 % reduction in the short circuit current density and a 0.2 V decrease in the open circuit voltage were observed; however, the original photovoltaic performance was recovered after exposure to dry nitrogen for four hours. Through similar investigations, recent work has shown that exposure to ambient water vapour is less detrimental to perovskite photovoltaics than previously thought. Indeed, exposure to ambient moisture during the precursor, deposition, annealing or post-fabrication stages has been reported to significantly enhance the final device performance [58, 73, 85–87].

Despite growing interest in this topic, there is no consensus on the effect of precursor exposure to moisture. Using a sequential spin coating procedure, Wu *et al.* reported a dramatic improvement in the morphology of neat PbI_2 films with the addition of 2 wt% H_2O to the precursor solution. Their optimized fabrication procedure yielded an 18 % efficient device in comparison with their anhydrous control device, which achieved a maximum power conversion efficiency of 0.0063 % [88]. Also

using a sequential deposition procedure, Adhikari *et al.* noted an optimized device performance with the addition of 5 vol% H_2O to the methylammonium iodide dipping solution [89]. Conings *et al.* performed a similar study using a well documented mixed halide, single-step deposition procedure. They observed little overall change in device performance with the substitution of up to 10 vol% of the anhydrous DMF solvent with deionized H_2O, suggesting that the required fabrication environment may be more flexible than previously thought [90]. In contrast, Gong *et al.* reported enhanced photovoltaic performance and stability with the addition of 2 wt% H_2O to the same single-step precursor solution [91].

The large discrepancy in observations indicates that the effects of water on methylammonium lead halide perovskites are still not well-understood, and that more work is needed to determine the precise mechanism(s) through which the two materials interact. Understanding the impact of precise quantities of water on perovskite thin films would be beneficial for further development of solution-processing techniques. In this study, the effects of water on the properties and photovoltaic performance of solution-processed perovskites were examined under highly controlled fabrication conditions.

5.2 Experimental methods

5.2.1 Fabrication details

To minimize uncontrolled exposure to moisture, synthesis and testing of perovskite devices were performed in a dry, argon glovebox ($<$ 0.1 ppm H_2O). All materials used for perovskite fabrication (PbI_2 (Alfa Aesar, 99.9985 %), MAI (Dyesol, $\geq$ 98%), anhydrous isopropanol (Aldrich, 99.5 %), and anhydrous DMF (Aldrich, 99.5 %)) were opened and stored in the glovebox; and, all vials and stir bars were baked at $\sim$120 °C in the glovebox, prior to use.

A sequential spin-coating fabrication method was chosen to reduce any effect that the contrasting water-solubility of PbI_2 and MAI may have on film homogeneity [87]. The effects of moisture were examined by incorporating small volumes of de-ionized water into the PbI_2 precursor solution to produce solutions containing 0, 1, 2, 4 and 6 mol% water with respect to the solute (i.e. mol% H_2O = $[H_2O]/[PbI_2]$ x

100, where [PbI_2] = 450 mg/mL = 0.976 M). These moisture concentrations were chosen to mimic the range of water concentrations expected to be inadvertently incorporated into perovskite precursor solutions during ambient fabrication. Hui *et al.* reported a water concentration of 0.025 mol/L in a DMF-based solution after 20 minutes exposure to a 50 % relative humidity environment [92]. In a 450 mg/mL PbI_2 solution, this equates to roughly 2.6 mol%.

"Wet" PbI_2 solutions were mixed using appropriate ratios of anhydrous solvent and "wet" solvent (a 10 µL/mL mixture of de-ionized H_2O in anhydrous DMF). The "wet" solvent was mixed and added to the PbI_2 solution 8 hours prior to fabrication to minimize the extent to which DMF may be hydrolyzed into formic acid and dimethylamine, while maximizing dissolution of the PbI_2, which is poorly soluble in water [93]. Large volumes of "wet" PbI_2 solutions were mixed to minimize head space in the vial, an especially crucial measure considering the low concentrations of water that were examined. Assuming 2 mL of head space in a standard 4 mL glass vial, the partial pressure of water at 70 °C corresponds to $\sim$2.19x10^{-5} mol of H_2O loss from solution. In a solution containing 6 mol% water, this represents nearly 20 % of the added water, or over 100 % of the added water in a solution containing 1 mol% water.

The MAI was mixed to produce a 47.5 mg/mL stock solution in anhydrous isopropanol, which was used for the fabrication of all films and devices. To avoid including foreign particles in the final films, all solutions were passed through 0.45 µm filters into clean, glass vials prior to use. The "wet" solutions were resealed immediately after filtering to minimize water loss.

5.2.2 Device fabrication and measurement

ITO substrates (2.5 x 2.5 cm) were patterned using a Kapton tape mask and etched in a 12 M HCl bath. The substrates were cleaned by scrubbing with detergent and de-ionized (DI) water, then ultrasonicating in baths of detergent, DI water, acetone and ethanol for 20 minutes each. Finally, the substrates were treated with UV-ozone for 20 minutes. The PEDOT:PSS layer was formed in air by spin-coating 90 µL of filtered Clevios AI 4083 onto each ITO substrate at 3000 rpm for 60 s. The films were annealed at 140 °C for 60 minutes, then rapidly transferred into an argon glovebox

for the remainder of the fabrication. 300 µL of 70 °C PbI_2 solution was spin-coated onto the cooled PEDOT:PSS at 6000 rpm for 180 seconds, then 8000 rpm for 180 seconds. The completed lead iodide films were dried on a 70 °C hotplate for 15 minutes. The perovskite was formed by spin-coating 400 µL of MAI solution onto the lead iodide film at 6000 rpm for 150 seconds, then annealing at 100 °C for 2 hours. 150 µL of 70 °C PCBM solution (30 mg/mL in chlorobenzene) was spun on the cooled perovskite films at 1000 rpm for 180 seconds, then annealed at 100 °C for 45 minutes. The devices were completed by thermally depositing 15 nm of calcium and 100 nm of aluminium at a base pressure of $\sim 10^{-6}$ Torr. The thicknesses of the PEDOT:PSS, perovskite and PCBM layers for the devices were estimated to be 50 nm, 270 nm and 80 nm, respectively, using a Dektak profilometer. The area of the completed devices was 0.035 cm^2.

Current density-voltage (JV) data were measured under 100 mW/cm^2 simulated AM1.5G sunlight using a ScienceTech solar simulator, and a Keithley 236 SMU. The illumination intensity was verified using a reference thermopile/KG5 glass filter combination. JV data were collected by sweeping from 1.5 V to -1.0 V (reverse scan) and -1.0 V to 1.5 V (forward scan) using two scanning rates: 1.0 V/s and 0.1 V/s. Transient photocurrent measurements were performed by biasing the device at 1.5 V for 2 seconds, then measuring the short circuit current density over time for up to 500 seconds.

5.2.3 Film fabrication

To preserve the integrity of the perovskite devices, films were made specifically to perform the characterization procedures. To ensure that the films were representative of the devices, the two were made within a few minutes of each other. The films were made on glass slides (2.5 x 2.5 cm), cleaned in the same manner as the ITO substrates, then coated with PEDOT:PSS and the perovskite, as specified. Several copies of each film were made to avoid confusing any trends with potentially destructive measurements, such as x-ray diffractometry and scanning electron microscopy. The completed films were stored in the glovebox until measurement. All characterization was performed in ambient within 24 hours of device measurement, unless otherwise specified.

5.3 Results and discussion

5.3.1 Device performance

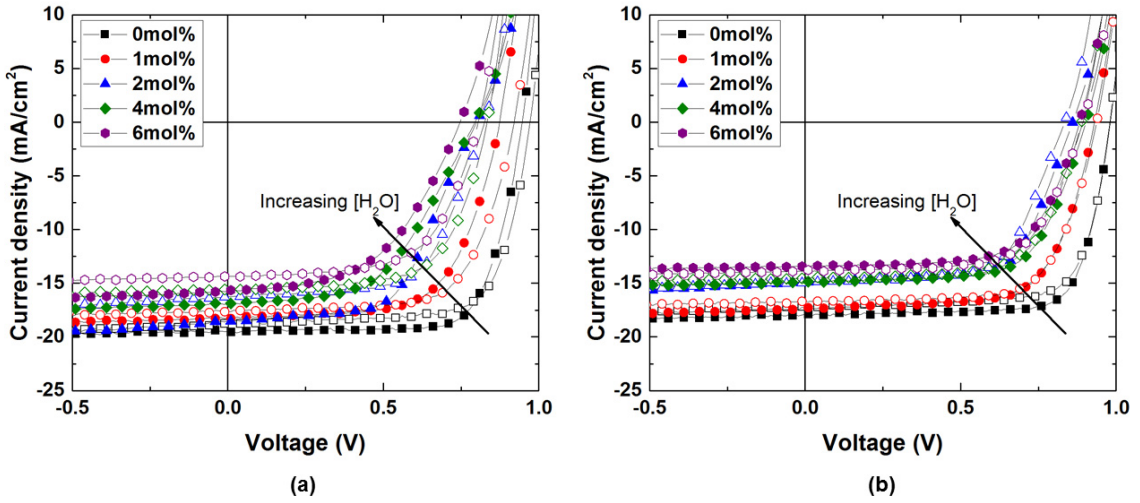

Figure 5.1: JV curves from the champion devices made with varying concentrations of H_2O in the PbI_2 solution. The devices were measured using (a) a 1.0 V/s scan rate, and (b) a 0.1 V/s scan rate. Reverse sweeps are indicated by the shaded symbols, while forward sweeps are indicated by the unshaded symbols.

Figure 5.1 compares the JV curves under one sun illumination (100 mW/cm^2) for the champion device measured at each H_2O concentration. The anhydrous control device was found to demonstrate excellent photovoltaic performance, with a maximum PCE of 13.6 % (measured at 0.1 V/s), comparable with published efficiencies for devices of the same architecture and fabrication method [10, 62, 71]. An undeniable decrease in photovoltaic performance was observed when higher concentrations of water were incorporated into the PbI_2 precursor solution. The addition of only 1 mol% of H_2O lowered the average open circuit voltage by nearly 100 mV, and the fill factor by approximately 0.1 (Table 5.1). As shown in Figure 5.2, the loss of open circuit voltage and fill factor was maintained when the concentration of water in the PbI_2 solution was further increased. A reduction in photocurrent was also observed in devices fabricated with water. Together, these three trends produced a detrimental effect on the overall device efficiency, as illustrated in Figure 5.2.

The trends observed in this dataset are contrary to existing studies, where the addition of water is reported to either: yield a peak device performance at a specific

Table 5.1: *JV* performance summary for devices with varying moisture contents in the PbI_2 solution. Errors represent the standard deviation of 9 - 16 devices measured with a 0.1 V/s scan rate. The figures in parenthesis represent the highest measured performance for each figure-of-merit.

$[H_2O]_{PbI2}$ mol%	V_{oc} (V)	J_{sc} (mA/cm^2)	PCE (%)	Fill factor
0	0.98 ± 0.04	14.6 ± 1.7	10.4 ± 1.5	0.73 ± 0.04
	(1.00)	(18.1)	(13.6)	(0.76)
1	0.91 ± 0.02	13.9 ± 2.3	7.9 ± 1.7	0.62 ± 0.03
	(0.95)	(17.2)	(10.8)	(0.66)
2	0.88 ± 0.02	10.6 ± 1.5	6.2 ± 0.8	0.67 ± 0.02
	(0.92)	(14.7)	(8.5)	(0.70)
4	0.90 ± 0.01	13.1 ± 1.2	7.6 ± 0.7	0.65 ± 0.02
	(0.92)	(14.7)	(8.8)	(0.68)
6	0.90 ± 0.01	11.7 ± 1.1	7.1 ± 0.7	0.68 ± 0.02
	(0.93)	(13.9)	(8.2)	(0.70)

water concentration [88,89,91]; or, produce no observable effect on the overall device performance and morphology [90]. Similar to this study, Conings *et al.* note a drop in open circuit voltage when water is added to the perovskite precursor solution, but the effect is compensated by an increased photocurrent, so no change in the overall device performance is observed [90].

The variety of observations are difficult to resolve; however, the reported device fabrication procedures differ from study to study. It is possible that the added water may interact differently when used in different perovskite precursors (i.e: single-step mixed halide precursor in comparison with sequential spin-coating of the two perovskite precursors). Currently, the only two other studies to examine the impact of added water on sequentially deposited perovskites are not well-controlled; and, report fabrication under ambient conditions, where atmospheric water vapour may also contribute to the observed trends [88,89]. In addition, we have chosen to investigate much smaller concentrations of water (by up to two orders of magnitude), with the belief that it is more representative of the water which may be inadvertently incorporated into precursor solutions during ambient processing. It is also worth highlighting the superior performance of our control devices.

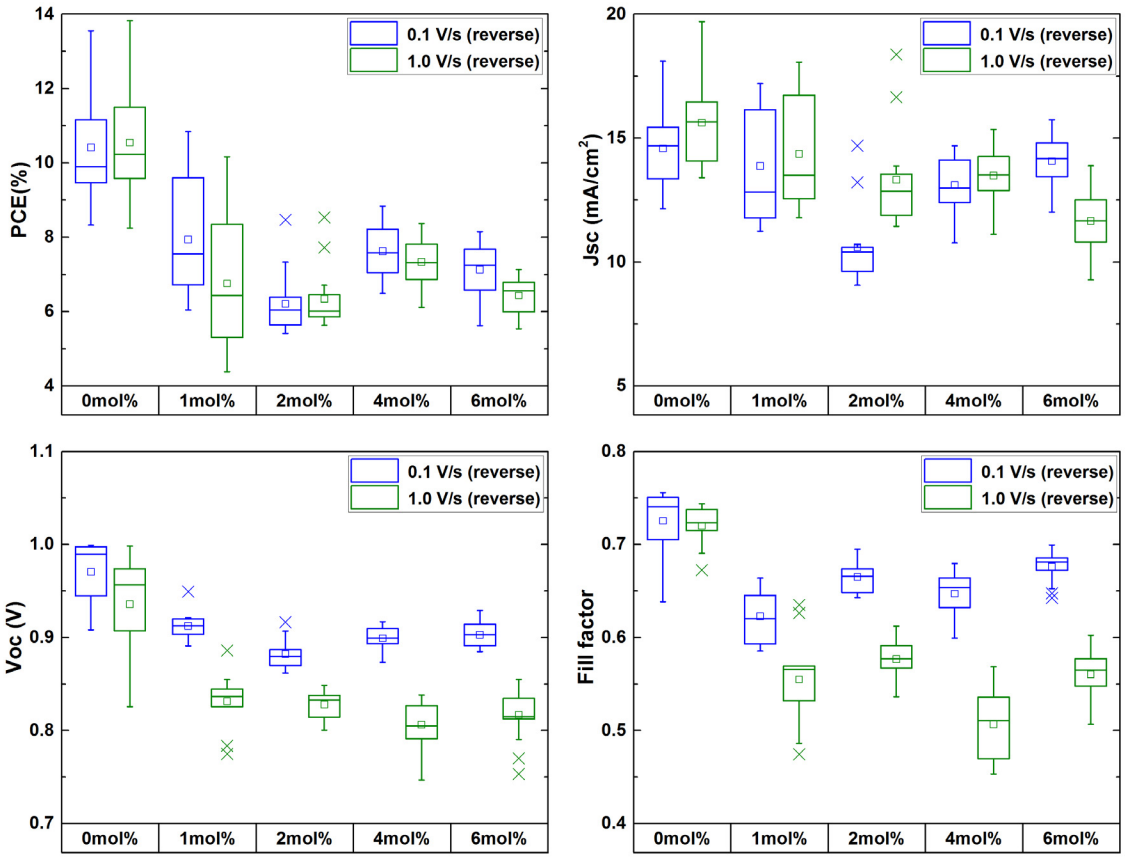

Figure 5.2: Statistical distribution of JV performance metrics for devices made using varying concentrations of H_2O in the PbI_2 solution. Data are representative of 9 - 16 devices tested by sweeping in the reverse direction at 0.1 V/s (blue) and 1.0 V/s (green). The spread of the data, mean, median and outliers are represented by the vertical bars, small square, horizontal line and crosses, respectively. An outlier was defined to be 1.5 times the interquartile range above or below the 75th and 25th percentile, respectively.

5.3.2 Hysteresis and transient behaviours

Transient behaviours are a well-known issue in perovskite photovoltaics. Photocurrent, and photovoltage transients often manifest as pronounced hysteresis in JV measurements. As a result, the measurable performance of a perovskite device may be greatly affected by biasing history, as well as scan-rate, and scan-directional dependencies [94–97]. This issue is a serious concern in the context of establishing an accurate representation of device performance; however, the transient effects,

broadly classified as anomalous hysteresis, are not fully understood. Although convincing theories and experimental evidence have attributed such behaviours to the migration of mobile ions, or capacitive effects there is still no universally accepted explanation [70,95,97–106]. It is, therefore, of great interest to understand the origin and nature of the observed hysteresis.

In comparison with other studies, very little scan-directional hysteresis was observed when JV measurements were taken at 0.1 V/s; the reverse- and forward-direction JV curves are nearly identical (Figure 5.1). This is further illustrated in Figure 5.3, which summarizes the batch statistics for several devices made using the same fabrication conditions. The scan-directional hysteresis is most reflected by a difference in open-circuit voltage, which may be up to $\sim$ 100 mV, for devices with water added to the PbI_2 solution. JV measurement at 1.0 V/s, resulted in a greater amount of hysteresis (Figures 5.1 and 5.4), which was exaggerated by further addition of H_2O to the PbI_2 solution. The low levels of hysteresis observed in this study are not entirely surprising given that reduced hysteresis is often reported in inverted architecture perovskite devices [7,10,12,88,107,108]. It has been suggested that the level of hysteresis is heavily influenced by the particular charge selective transport layers [104, 108, 109], where PCBM is additionally thought to passivate trap states within the perovskite that contribute to photocurrent hysteresis [70, 110].

Device hysteresis was further studied by measuring the effect of biasing history on photovoltaic performance. Each device was held at +1.5 V bias under 1 sun illumination for 2 seconds before measuring the short-circuit current density over 20 seconds. Although strong evidence has been shown to suggest that bias history, and not light soaking, is responsible for hysteresis [96, 97], each device was held at zero bias in the dark for 1 minute before measurement to minimize any possible contributions from competing light driven effects [94, 111–113]. The measured transient photocurrents are shown in Figure 5.5 (a), normalized to their initial short circuit current density (at t = 0 seconds). Interestingly, opposite transient dynamics were observed for devices made using anhydrous precursors and devices made using hydrated precursors. Anhydrous devices were seen to exhibit a photocurrent decay; whereas, all devices fabricated with added water demonstrated photocurrent growth over the 20 second period. As observed by other authors, the transient behaviour for each device

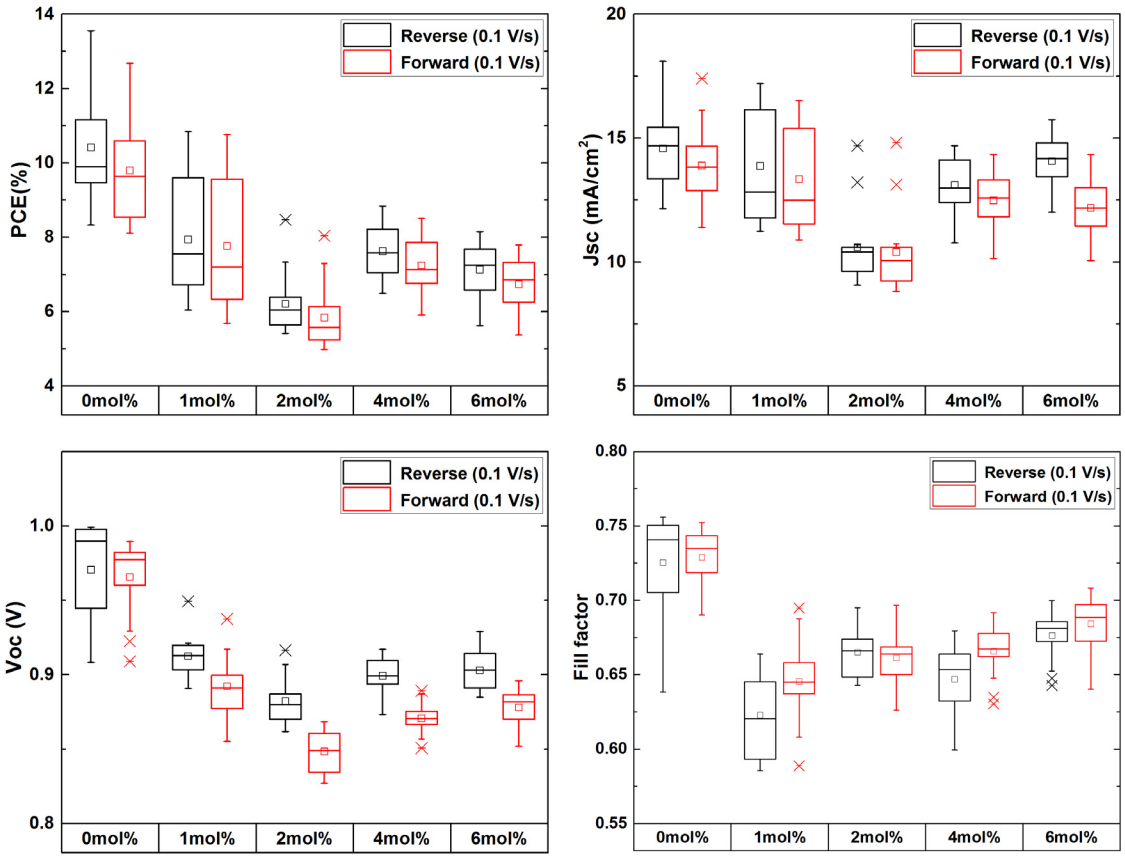

Figure 5.3: Statistical distribution of JV performance metrics for devices made using varying concentrations of H_2O in the PbI_2 solution. Data are representative of 9 - 16 devices tested by sweeping at 0.1 V/s in the reverse direction (black) and the forward direction (red). The spread of the data, mean, median and outliers are represented by the vertical bars, small square, horizontal line and crosses, respectively. An outlier was defined to be 1.5 times the interquartile range above or below the 75th and 25th percentile, respectively.

was observed to be biexponential [96, 98, 104]. The time constants extracted from a biexponential fit to each of the photocurrent transients are shown in Figure 5.5 (b). The magnitude of the time constants was seen to increase gradually with the device moisture content. An anomaly, however, was observed in devices made using 2 mol% H_2O in the PbI_2 solution, which demonstrate an initial photocurrent decay, followed by monoexponential growth. Such behaviour suggests that two competing transport mechanisms may coexist within perovskite films. In general, the slow time components of the short-circuit photocurrent growth were similar in magnitude to

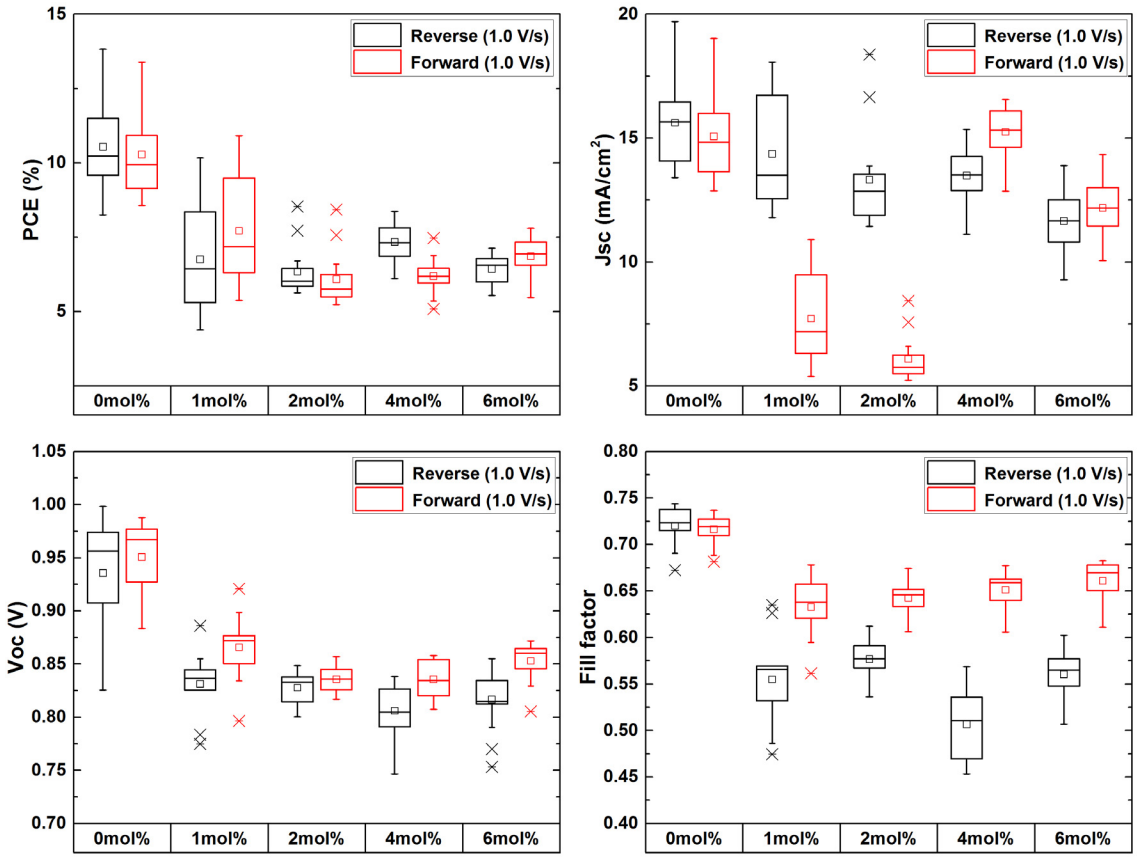

Figure 5.4: Statistical distribution of JV performance metrics for devices made using varying concentrations of H_2O in the PbI_2 solution. Data are representative of 9 - 16 devices tested by sweeping at 1.0 V/s in the reverse direction (black) and the forward direction (red). The spread of the data, mean, median and outliers are represented by the vertical bars, small square, horizontal line and crosses, respectively. An outlier was defined to be 1.5 times the interquartile range above or below the 75th and 25th percentile, respectively.

those reported by Eames *et al.*, who reported transient growth on the timescale of seconds after reverse biasing.

To further study the anomalous device hysteresis, the transient photocurrent measurements were repeated over 500 seconds, as shown in Figure 5.6 (f). In addition, the reverse, then forward JV sweeps of the corresponding devices were measured at 1.0 V/s, 0.1 V/s, then 0.01 V/s. Again, devices fabricated from anhydrous PbI_2 solution exhibited a photocurrent decay; whereas, devices fabricated from hydrated precursors demonstrated a photocurrent growth over the 500 second measurement.

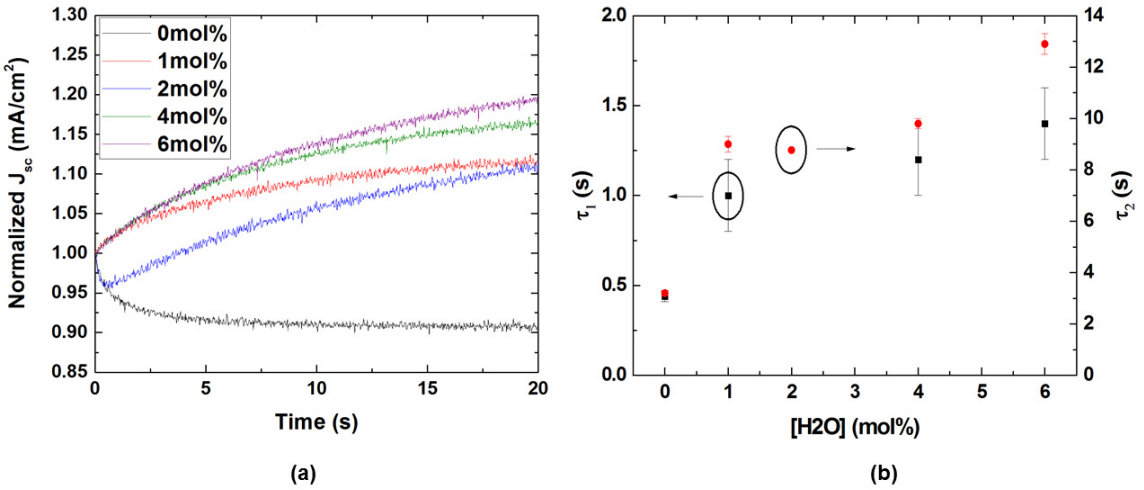

Figure 5.5: Representative transient photocurrent behaviours, at short-circuit, for devices with varying concentrations of H_2O in the PbI_2 solution, (a). The time constants extracted from a biexponential fit of each curve are shown in (b), where τ_1 is shown on the left axis (black), and τ_2 is shown on the right axis (red). The anomalous behaviour of the 2 mol% device was treated by applying a single exponential fit to the transient growth to extract the second time constant.

The steady-state photocurrent for the device in Figure 5.6 (a) is observed to nearly converge with the JV trace measured at the slowest scan rate. As indicated by other authors this suggests that only very slow JV measurement rates ($\leq$0.01 V/s) are truly representative of steady state device operation [94]. Unexpectedly, the transient photocurrent growth observed in hydrated devices was not accompanied by an increased photocurrent at slower scan rates, but rather a decreased photocurrent and an increased open-circuit voltage.

5.3.3 Suggested model of transient effects

A model describing the observed transient behaviours is suggested based on the migration of mobile ions within the perovskite film. Under an external bias, mobile ions are expected to accumulate in specific areas of a device, thereby altering the internal field and charge extraction efficiency. Experimental and theoretical studies have, in fact, suggested ion migration to give rise to transient behaviours and anomalous hysteresis in perovskite devices [70, 95, 97–101]. Although the activation energy associated with the migration of each ion varies between studies, the iodide ion, I^-,

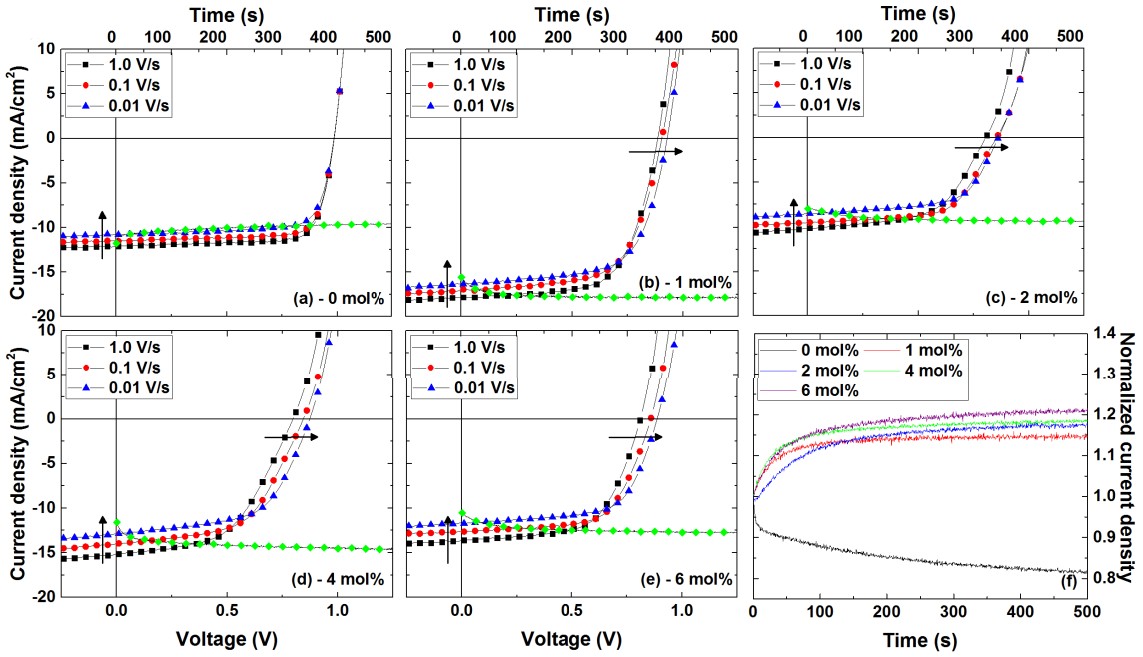

Figure 5.6: Rate dependent JV measurements (for reverse sweeps) and transient photocurrent behaviours for the corresponding device with varying concentrations of H_2O in the PbI_2 solution, (a) - (e). The transient photocurrents are shown in green, and correspond to the time axis from 0 to 500 seconds. The transients shown in (a) - (e) are contrasted in (f), normalized to the initial photocurrents. (The measurements shown in this figure were taken 20 days post-fabrication.)

is consistently found to exhibit the lowest activation energy, followed by MA^+ and Pb^{2+} [98–100,114]. Shao *et al.* have also produced convincing experimental evidence linking I^- migration with hysteresis [101]. A model for the transient effects observed in the anhydrous devices will first be described. A description of the hydrated devices, accounting for the difference in transient dynamics, will follow.

Figure 5.7 shows a band diagram for an inverted architecture perovskite device under short-circuit and forward biasing conditions. Under normal operating conditions, free electrons and holes are collected by the aluminum and ITO, respectively; however, extended forward biasing could enable the I^- ions to migrate freely toward the device anode. Assuming that ion migration is confined to the perovskite layer, the two-second forward bias treatment would cause an accumulation of I^- ions near the PEDOT/perovskite interface, resulting in an internal electric field, which would facilitate carrier extraction. Once the device is short-circuited, I^- ion diffusion away

from the interface would result in a decreased charge collection efficiency, and a decreased photocurrent over time (Figure 5.6). This behaviour is also reflected in the sequence of JV sweeps in Figure 5.6; reverse sweeps performed at slower scan rates allow greater relaxation of the ionic concentration gradient, resulting in a decreased charge collection efficiency, and a lower photocurrent. A similar migration model has also been suggested for normal architecture devices, where forward biasing was reported to enable I^- migration toward the perovskite/anode interface, leaving positively charged iodide vacancies at the opposite interface. In this case, the ion redistribution was suggested to produce band bending at the perovskite interfaces, leading to improved carrier extraction through tunnelling [103, 115].

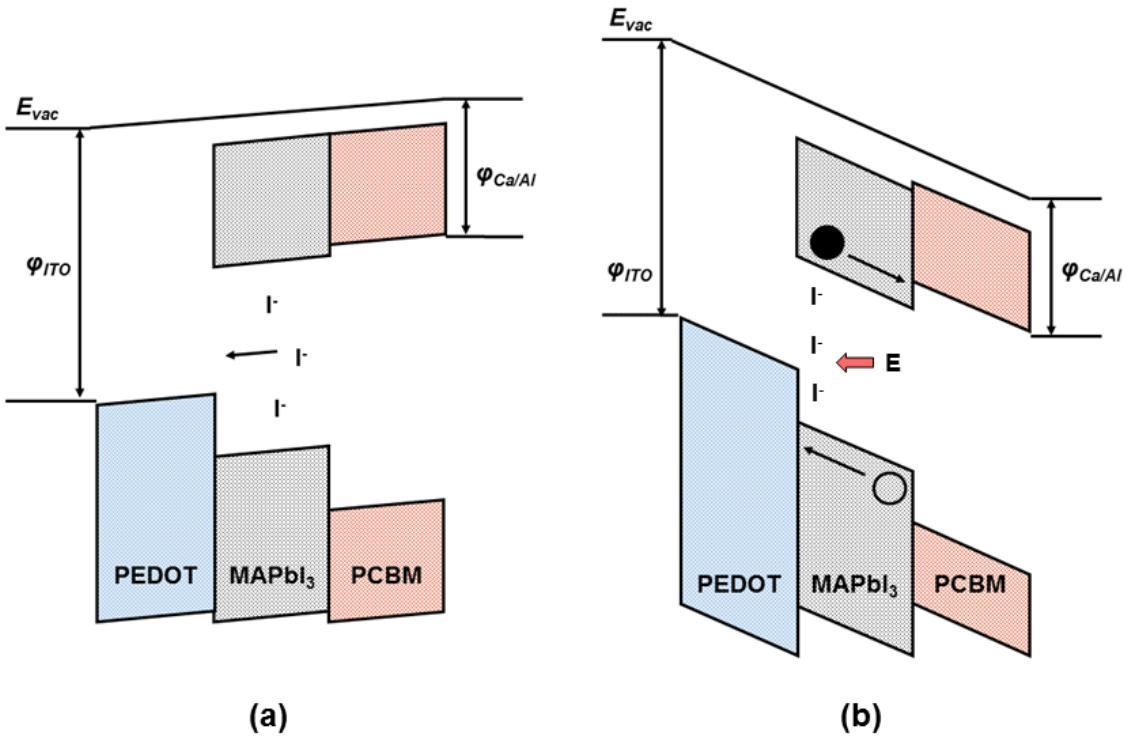

Figure 5.7: Band diagrams illustrating ion migration and carrier extraction within the perovskite device (a) under forward bias and (b) under short-circuit conditions, post-biasing. Over time, the iodide ions are expected to diffuse away from the PEDOT/perovskite interface, resulting in a time-dependent charge extraction efficiency.

In the presence of water, H_2O incorporation into the perovskite is thought to be energetically favourable, leading to its spontaneous infiltration into the lattice [114, 116]. Both computational and experimental studies suggest that the absorbed water

interacts strongly with the methylammonium cation and surrounding iodine atoms through hydrogen-bonding [114, 116]; however, the ultimate degradation pathway(s) caused by water exposure are not agreed upon. Some authors propose an acid-base reaction, whereby a single water molecule may be sufficient to degrade the material, but an excess of water is required to dissolve the by-products [82, 117].

$$n\,[(CH_3NH_3{}^+)PbI_3] + H_2O \longrightarrow [(CH_3NH_3{}^+)_{n-1}(CH_3NH_2)nPbI_3][H_3O] \longrightarrow$$
$$HI + CH_3NH_2 + H_2O + PbI_2 + (n-1)[(CH_3NH_3{}^+)PbI_3] \tag{5.1}$$

Other authors suggest a reversible hydration of the perovskite, where irreversible degradation is only achieved if an excess of water is present to dissolve the $CH_3NH_3{}^+$ [83, 84].

$$4\,(CH_3NH_3)PbI_3 + 4\,H_2O \rightleftharpoons 4\,[CH_3NH_3PbI_3 \cdot H_2O] \rightleftharpoons$$
$$(CH_3NH_3)_4PbI_6 \cdot 2\,H_2O + 3\,PbI_2 + 2\,H_2O \tag{5.2}$$

Based on the proposed reactions, it is speculated that structural and chemical changes resulting from water incorporation favours the motion of MA^+ ions over I^- ions. In the pure monohydrate and dihydrate perovskite phases, water is incorporated between the $[PbI_6]^{4-}$ octahedra with the methylammonium cation, resulting in an arrangement of $[PbI_6]^{4-}$ octahedra separated by methylammonium ions and H_2O [84, 118, 119] (Figure 5.8). Although no crystalline hydrate phases were observed in this study (Figure 5.11), it is possible that sufficient water was incorporated into the perovskite lattice to disrupt the caging of the MA^+ cation, and facilitate its migration throughout the film. The presence of H_2O has also been suggested to deprotonate the methylammonium cation [82, 117], which could allow liberated H^+ ions to migrate throughout the lattice. The energy barrier for H^+ migration is suggested to be lower than for intrinsic ionic species such as $CH_3NH_3{}^+$ and I^- [98, 120]. Regardless of which reaction pathway is more likely, the addition of water to the perovskite is seen to increase the population of mobile ions within film. Furthermore, changes to the perovskite lattice may also lower the activation energy for the migration of certain ionic species, such as MA^+. A larger number of mobile ions would explain the increased hysteresis observed when higher concentrations of water were included in the perovskite film (Figure 5.3).

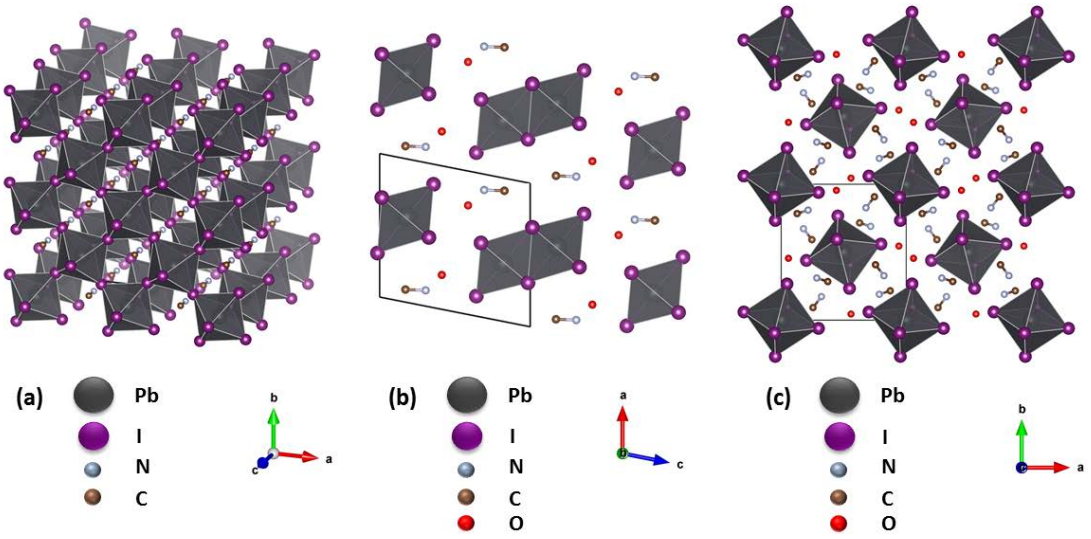

Figure 5.8: Diagram illustrating the methylammonium lead iodide perovskite structure in its anhydrous (a), monohydrate (b), and dihydrate (c) phases. The presented views are projections along the [112], [010] and [001] directions, respectively. The hydrogen atoms are not shown.

The suggested changes in ion mobility could account for the difference in transient dynamics observed between anhydrous and hydrated devices. Under the two-second forward bias treatment, the mobile MA^+ (and possibly H^+) ions would migrate towards the device cathode, resulting in an accumulation of positive charge at the perovskite/PCBM interface (Figure 5.9 (b)). The accumulation of positive charge would create a localized potential well, trapping electrons and decreasing the measured photocurrent. Once the device is short-circuited, the MA^+ ions would diffuse away from the interface, allowing for more efficient charge collection over time. This behaviour is also reflected in the sequence of JV sweeps presented in Figure 5.6 when considering the entire biasing history of the device. After the first measurement at 1.0 V/s, the device was immediately scanned from -1.0 V to +1.5 V before it was measured from +1.5 V to -1.0 V at 0.1 V/s. Therefore, the most recent biasing history of the device before the reverse sweep at 0.1 V/s was 1.5 seconds at increasing forward bias, which would cause positive ion accumulation at the perovskite/PCBM interface. The effect would be exaggerated for progressively slower scan rates; thus, the slowest scan rate (which was previously forward biased for the longest amount

of time) should experience the largest photocurrent suppression. Although the suggested model of ion migration agrees well with experimental data, a more detailed investigation is necessary to verify these concepts.

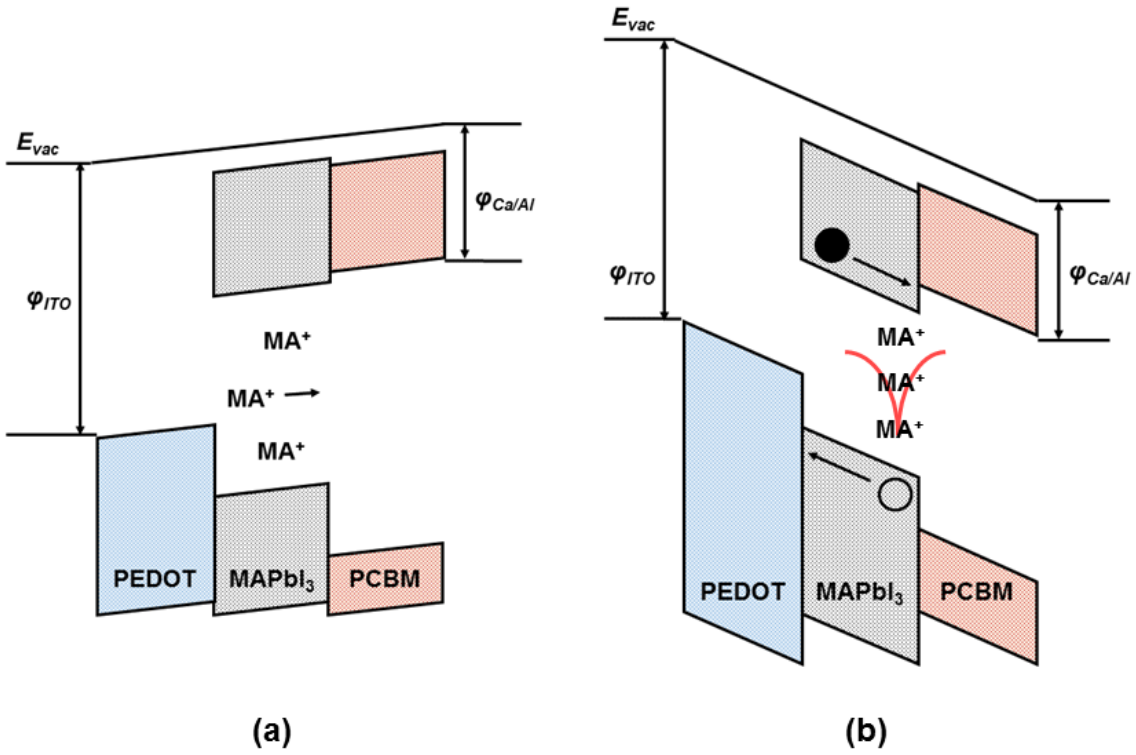

Figure 5.9: Band diagrams illustrating ion migration and carrier extraction within the perovskite device under (a) forward bias and (b) short-circuit conditions, post-biasing. Over time, the methylammonium ions are expected to diffuse away from the perovskite/PCBM interface, resulting in improved charge extraction efficiency.

5.3.4 Effect of water content on film morphology:

As previously discussed, film morphology is known to have a significant impact on the performance of perovskite photovoltaics [43, 51, 64]. Poor surface coverage by the perovskite film decreases photon absorption, and enables the formation of shunt pathways through the device, both of which lower the photogenerated current. Even when full surface coverage is achieved, grain morphology can also affect the device efficiency. Larger crystal grains are favourable, as they lower the probability of carrier trapping by defect states at grain boundaries [101]. It is therefore of interest

to characterize the impact of added water on the morphology of the perovskite layer.

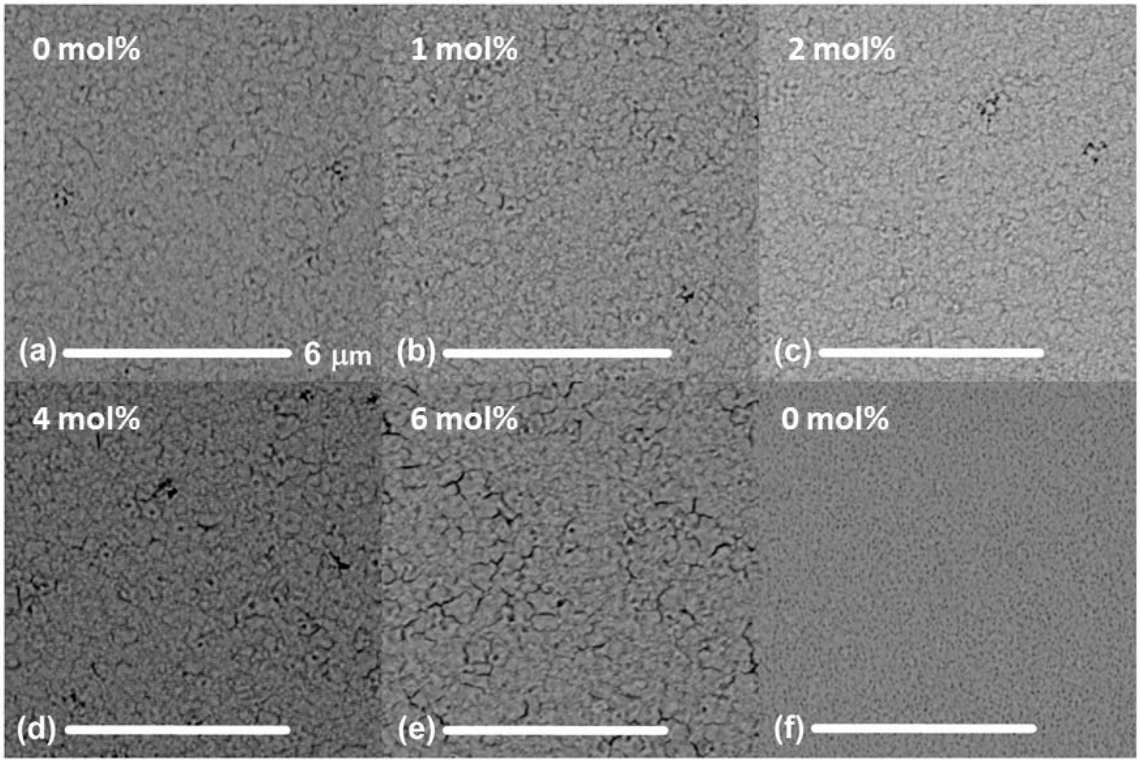

Figure 5.10: Top-view SEM images of films made with varying concentrations of H_2O in the PbI_2 solution: (a) 0 mol%, (b) 1 mol%, (c) 2 mol%, (d) 4 mol% and (e) 6 mol%. A film of unconverted PbI_2 with 0 mol% H_2O is shown for comparison, (f). The scale bar on all films represents 6 μm. Images were taken in regions corresponding to the device locations on the substrate.

Figure 5.10 shows a series of top-view SEM images for the perovskite films fabricated with varying concentrations of water in the PbI_2 solution. In order, the images show films fabricated with 0 mol%, 1 mol%, 2 mol%, 4 mol% and 6 mol% H_2O in the PbI_2 solutions, respectively. The final image is of a PbI_2 film with 0 mol% H_2O, illustrating the high surface coverage of the PbI_2 layer. Overall, the perovskite films were seen to exhibit a compact, dense morphology and a high surface coverage. Films fabricated with less than 4 mol% H_2O in the PbI_2 solution demonstrated the highest surface coverage, with the majority of grain sizes falling below 200 nm and a small fraction of grains exceeding 500 nm in size. In contrast, a much higher fraction of grains exceeded 500 nm when films were fabricated with 4 mol% and 6 mol% H_2O PbI_2 solutions; some grains sizes appeared to exceed 1 µm. These films, however,

showed a lower surface coverage and an increased density of pinholes and cracking between larger grains. Similar trends regarding increased grain size and pinhole formation have also been reported in other studies when moisture is introduced during the perovskite fabrication procedure [58, 73, 86, 87, 90, 91].

The observed film morphology is consistent with trends in measured device performance. Increased cracking and pinhole formation in films with more moisture would introduce a greater number of shunt pathways, explaining the reduction in short-circuit current and open-circuit voltage for devices made with higher concentrations of water (Figures 5.1 and 5.2). It is also possible that larger perovskite grain sizes could be accompanied by increased film roughening in the z-direction, leading to incomplete coverage by the PCBM layer and greater recombination at the interface between the perovskite and top contact.

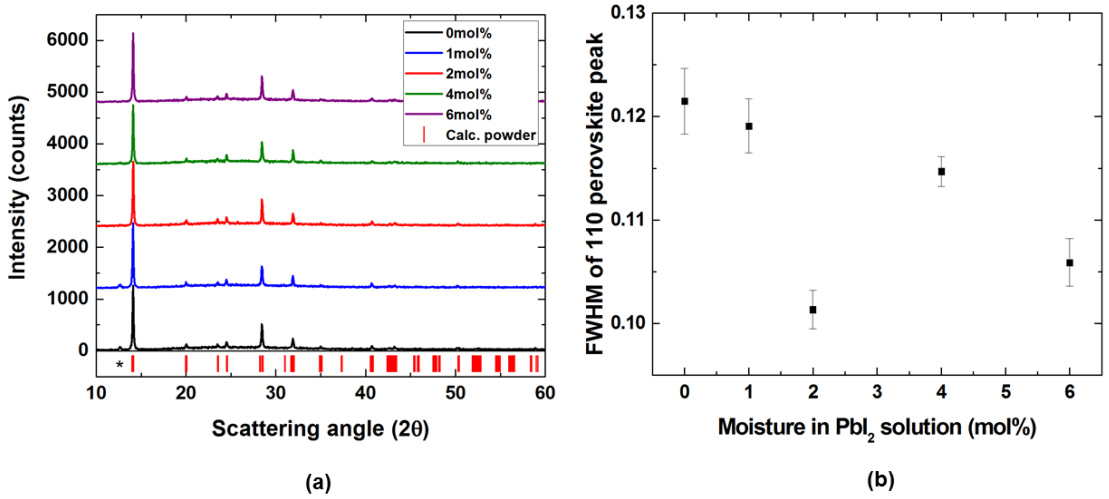

Figure 5.11: Unnormalized XRD patterns of perovskite thin films with varying concentrations of H_2O in the PbI_2 solution, (a). The red ticks indicate the calculated powder perovskite diffraction pattern of the tetragonal $I4cm$ phase; while, the black asterisk marks the location of the (001) PbI_2 diffraction peak. Patterns are offset by 1200 counts for clarity. The FWHM of the (110) perovskite peak is plotted as a function of H_2O concentration, (b).

Figure 5.11 shows a series of XRD patterns for perovskite films prepared with varying moisture content. The patterns indicate that the tetragonal ($I4cm$) $MAPbI_3$ perovskite phase was successfully formed in all instances, with strong preferential orientation in the (110) direction. All films were also seen to exhibit similar relative

peak intensities, which suggests that the preferential grain orientation was not greatly affected by the presence of water. Interestingly, perovskite films fabricated with low concentrations of H_2O in the PbI_2 solution (0 mol% and 1 mol%) contained detectable amounts of crystalline PbI_2, while the other films did not. Other authors have also observed incomplete conversion and residual crystalline PbI_2 when sequential-step perovskite conversion was carried out in a low humidity environment (RH = 1%), while conversion under higher relative humidity was observed to yield phase pure perovskite [73]. Whether the observation of residual PbI_2 in this study was due to degradation during annealing, or simply due to incomplete conversion is unknown. Gangishetty *et al.*, suggest that moisture may facilitate MAI incorporation into the PbI_2/perovskite lattice by introducing a less-compact intermediate hydrate phase, thereby facilitating the perovskite conversion [73].

It is interesting to note that the higher performances of the 0 mol% and 1 mol% H_2O devices correspond to films with residual PbI_2, which is consistent with the passivating effects of lead iodide suggested by other authors [72,76,77]. Although this hypothesis is well-supported by the presented data (Figure 5.11), it is important to note that the presence (or absence) of crystalline PbI_2 in Figure 5.11 (a) be regarded with caution due to the inherent limitations of using the Bragg-Brentano diffraction geometry to indicate phase composition in thin-film samples. Finally, as described by the Debye-Scherrer equation, the slight broadening of the (110) perovskite peak may be correlated with a higher proportion of smaller crystallites within the bulk of the films.

In this study, no significant enhancement in the diffraction intensity was observed with increasing moisture in the PbI_2 solution, which suggests that all films were similarly crystalline. The fact that other studies have observed increased crystallinity in perovskite films annealed under relative humidity suggests that ambient moisture may facilitate solvent vapour annealing of the perovskite films [58]. It is interesting to note that very similar effects to those reported of ambient moisture treatments have also been observed in perovskite films treated with DMF solvent vapour [71]. It seems possible that the enhanced crystallinity and performance observed in such reports may be primarily a consequence of improved film morphology, rather than any chemical change resulting from the water inclusion in the perovskite lattice.

5.3.5 Photophysics of the perovskite devices

Methylammonium lead iodide perovskites are known to exhibit strong absorption across the visible light region. Regardless of the water content, all perovskite films produced an absorption spectrum characteristic of methylammonium lead iodide (Figure 5.12 (a)). The absorption spectra of all films appeared similar, but suggest a marginally lower absorption intensity with increasing water concentration. It is difficult to verify the significance of this trend, however, since the apparent absorption of any material may be influenced by light scattering off crystal grains, or light transmission through cracks and pinholes. An accurate quantification of such effects would require a more rigorous experimental set-up.

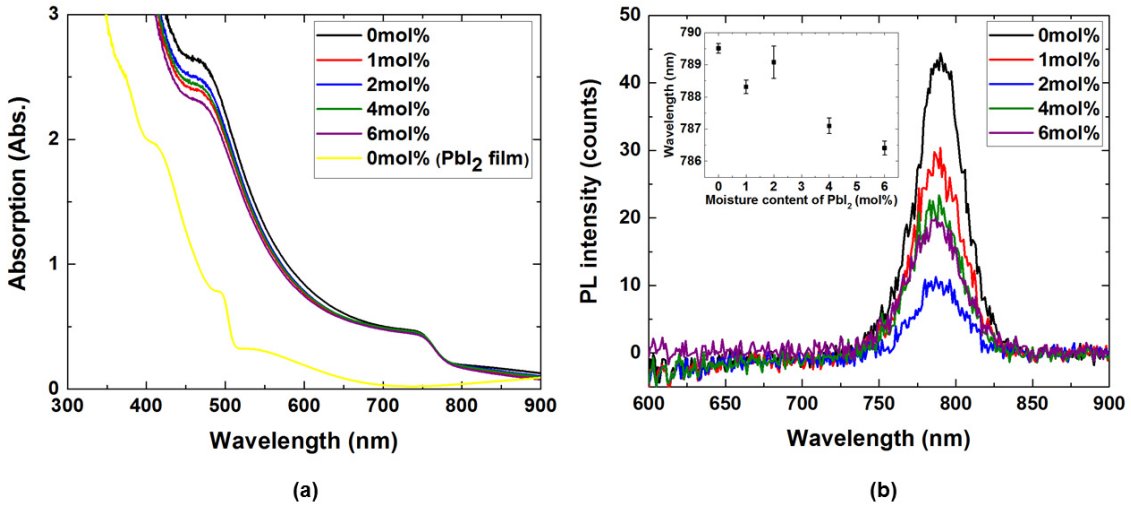

Figure 5.12: The UV-vis absorption spectra (a), and photoluminescence spectra (b) of perovskite thin films made with varying concentrations of H_2O in the PbI_2 solution. Spectra were measured within 24 hours of device testing.

As previously described, photoluminescence (PL) measurements can provide a good indication of the types of recombination pathways in photovoltaic materials. High PL intensity is often attributed to less non-radiative recombination of photo-generated carriers; and therefore, better photovoltaic performance. Steady state PL measurements of the perovskite thin films were collected using a Cary Eclipse spectrophotometer, operating at a 520 nm excitation wavelength. A distinct emission peak was observed at ∼790 nm, with the highest emission intensity corresponding

to the anhydrous perovskite film. In general, the PL intensity was seen to decrease with increasing water concentration in the PbI_2 solution, which suggests an increased number of non-radiative recombination pathways. This trend is consistent with the decreased device performance observed in perovskite films with added moisture (Figure 5.1). Peak fitting indicates a slight blue shift ($\Delta\lambda$ =$\sim$3 nm) in the maximum luminescence intensity with the addition of increasing quantities of water (Figure 5.12 (b), inset). Similar trends have also been reported by other authors upon exposure of the perovskite to ambient humidity [121, 122]; the observed blue-shift is suggested to arise from lattice strain resulting from water incorporation into the perovskite crystal [122].

5.3.6 Effect of moisture content on device stability:

The long-term stability of any emerging technology is always an issue of considerable importance. In this regard, methylammonium lead halide perovskites currently fall short of realistic goals, particularly in the presence of water. However, when JV measurements were repeated 20 days post-fabrication, the inclusion of moisture into the perovskite layer was, remarkably, observed to have a stabilizing effect on the long-term device performance. Figure 5.13 compares the JV curves for several devices tested 24 hours post-fabrication with the same devices tested 20 days post-fabrication. The precise performance metrics are summarized in Table 5.2. The best anhydrous device was observed to experience, roughly, a 25 % decrease in power conversion efficiency (PCE) and a 30 % decrease in photocurrent after 20 days of storage. The severity of the performance loss was alleviated by the inclusion of water in the PbI_2 solution, with the best 1 mol% device yielding the greatest stability and a higher PCE than the best anhydrous device after 20 days. Only a 9 % decrease in the measured PCE was observed in the 1 mol% device after 20 days. It is important to note that all devices in this study were stored under argon, and were at no point exposed to an ambient atmosphere. Wu *et al.* and Gong *et al.* also report good stabilities for their optimized devices, in comparison to their anhydrous control device, reporting a 10 % and 8 % loss of PCE after 40 and 6 days, respectively [88, 91]. As far as we know, however, this is the first report where long-term device stability under inert conditions is explicitly linked to all devices with included moisture. These

results are both unexpected and interesting, and should be considered an important topic of future investigation.

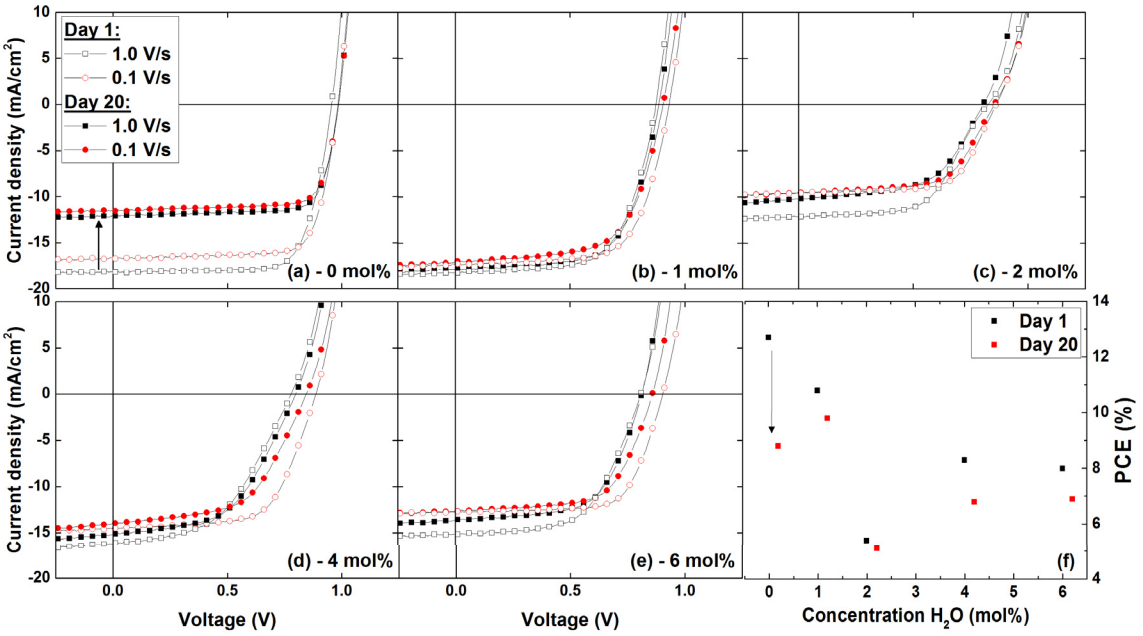

Figure 5.13: *JV* curves for perovskite devices made with varying concentrations of water measured 1 day (unshaded symbols) and 20 days (shaded symbols) post-fabrication. The *JV* curves represent measurements from forward to reverse bias at two scan rates: 1.0 V/s (black) and 0.1 V/s (red). The PCE loss after 20 days is summarized in (f).

5.4 Conclusions

This study has shown that the incorporation of controlled volumes of water into the PbI_2 precursor, similar to those expected due to inadvertent exposure of PbI_2/DMF solutions to moist air, causes significant changes in the performance of sequentially spin-coated perovskite devices. Contrary to recent publications, increasing concentrations of water are observed not only to reduce overall device performance, but also to exaggerate the scan-rate and scan-directional dependent current-voltage hysteresis. We propose that the addition of water to the precursor solution results in a larger population of mobile ions in the final perovskite film, which migrate under bias, causing *JV* hysteresis. Surprisingly, the inclusion of water in the perovskite film is also observed to stabilize long-term device performance. At best an approximately

Table 5.2: Comparison of *JV* performance metrics for devices made with varying moisture contents in the PbI_2 precursor solution. Devices were measured before and after 20 days storage in an argon glovebox.

[H_2O] (mol %)	Voc (V)		Jsc (mA/cm2)		PCE (%)		FF	
	Day 1	Day 20	Day 1	Day 20	Day 1	Day 20	Day 1	Day 20
0	0.998	0.995	16.8	11.4	12.7	8.8	0.76	0.77
1	0.949	0.916	17.2	17.1	10.8	9.8	0.66	0.63
2	0.878	0.865	9.5	9.5	5.4	5.1	0.65	0.61
4	0.894	0.845	14.6	14.1	8.3	6.8	0.63	0.57
6	0.917	0.861	12.8	12.7	8.0	6.9	0.68	0.63

9 % decrease in PCE was observed for a device with 1 mol% H_2O after 20 days. In comparison, a device fabricated from completely anhydrous precursors experienced a loss in PCE of nearly 25 %. In addition, the PCE of the best 1 mol % H_2O device exceeded that of the best anhydrous device after 20 days. The suggested model for ion migration must still be verified; and, the precise mechanism through which water enhances long-term device stability is yet to be determined. Both issues should be considered an important subject for further investigation.

Chapter 6

Conclusions and future work

6.1 Conclusions

Perovskite materials are widely considered to be the up-and-coming PV technology. Of the many fabrication methods reported for perovskite thin-films, sequential-step solution-processing projects the most promising avenue for further development. The morphology control offered by sequential deposition, allows high-performance perovskite solar cells to be achieved in multiple device structures and architectures. Above all, the planar inverted device architecture, is currently the most environmentally and economically sensible option, owing to is its simplicity, and low-temperature processing requirements. Optimizing perovskite devices of this design would enable the most facile transition to commercial mass-production techniques, assuming the stability issues can be resolved.

Still, many facets of methylammonium lead halide perovskites must be understood: among them, the effect of moisture on device performance and stability. The results of this study imply that careful environmental control must be exercised in order to achieve maximum photovoltaic performance. It is possible that the immediate and dramatic effect of moisture on photovoltaic performance could contribute to the wide variation of published efficiencies. While strict environmental control may not always be possible, the precise fabrication environment should be diligently reported.

6.2 Future work

The scope of this thesis has identified several unique and some unexpected behaviours that merit further investigation.

In particular, Chapter 5: the impact of water on the formation and performance of perovskite photovoltaics, bears several shortcomings in its present state. First

and foremost, the water content in the final perovskite film was not quantified. It is possible that the water incorporated into the PbI_2 precursor solutions was entirely evaporated during the two hour annealing treatment at 100 °C, which was required to convert the PbI_2/MAI bilayer into crystalline perovskite. If this is true, then partially hydrated $MAPbI_3$ perovskite phases cannot contribute to the observed transient behaviours as described in the suggested model of ion migration. X-ray photoelectron spectroscopy may provide some enlightenment in this regard provided that the remaining H_2O concentrations are within the instrumental detection limit (typically one part per thousand). Another possibility would involve dissolving the perovskite films to perform Karl Fischer titration.

This study would also benefit from a more conclusive identification of the presence and species of mobile ions, which would greatly influence the suggested model describing transient behaviours. Although other authors have used techniques such as energy-dispersive x-ray spectroscopy to identify element redistribution throughout the perovskite film, it may be possible to obtain similar information through other means [101]. In particular, it would be interesting to modify factors, other than moisture content, which affect ion migration. For example, higher concentrations of MAI in the final perovskite film may favour the migration of MA^+ over I^- ions, and mimic the transient behaviours observed in hydrated perovskite devices. The use of other organic cations should also exhibit different migration dynamics based on their molecular weight. It is conceivable that smaller organic cations would migrate more freely through the perovskite lattice leading to more rapid transient behaviours (i.e. with shorter migration time constants), while larger organic cations should exhibit slower transient effects. The formamidium cation ($CH(NH_2)_2{}^+$) would be a sensible starting point, as it is only slightly larger than the methylammonium cation, and has been shown to demonstrate competitive performance to $MAPbI_3$ perovskites [123]. Numerous other organic ammonium salts such as ethylammonium iodide are also commercially available; although they have not been as extensively studied, they would be natural follow-ups. Ion migration has been experimentally linked with grain boundaries and defects [101]; therefore, it may also be of interest to perform similar transient measurements on single crystal perovskites. If ion migration is the only source contributing to the observed transient effects, single crystal perovskite

devices should exhibit little to no transient behaviours.

A repeated study examining the incorporation of water into the MAI precursor solution is another possible avenue of exploration. If the effects of water are manifested only in the $MAPbI_3$ product, then results similar to those presented in Chapter 5 should be expected. It is likely, however, that water interacts more favourably with one of the two perovskite precursors, especially given the high water solubility of MAI. Experimental and theoretical evidence has also suggested hydrogen bonding interactions between the MA^+ cation and H_2O [114,116]. It is therefore possible that such a study may elicit more dramatic results than those presented here. The water solubility of MAI would also enable a much larger range of water concentrations to be easily studied in comparison to PbI_2, which has a very limited solubility in water.

Finally, a mechanism enabling the (surprising) enhancement of device stability via water inclusion in the PbI_2 precursor solution has not been identified. Given that long-term stability remains one of the greatest obstacles to perovskite photovoltaics, this should be considered an important subject for further investigation. It is possible that slow water loss from the hydrated perovskite devices leads to improved JV performance, counterbalancing the overall device degradation and causing an *apparent* improvement to long-term stability. This postulate should be verified by monitoring H_2O evolution from the perovskite layer over time. Such a study could be performed using techniques such as energy-dispersive x-ray spectroscopy or x-ray photoelectron spectroscopy, assuming that the H_2O concentrations in the perovskite films remain within instrumental detection limits. Another possibility would involve dissolving similarly prepared and aged perovskite films for Karl Fischer titration.

Bibliography

[1] D. S. Ginley and D. Cahen, *Fundamentals of materials for energy and environmental sustainability* (Cambridge university press, 2012).

[2] N. S. Lewis and D. G. Nocera, "Powering the planet: Chemical challenges in solar energy utilization", Proceedings of the National Academy of Sciences **103** (2006) 15729–15735.

[3] M. Brunisholz, "Snapshot of global photovoltaic markets", Technical Report Report IEA PVPS T1-29:2016, International Energy Agency (IEA) (2015).

[4] M. M. de Wild-Scholten, "Energy payback time and carbon footprint of commercial photovoltaic systems", Solar Energy Materials and Solar Cells **119** (2013) 296–305.

[5] A. Kojima, K. Teshima, Y. Shirai, and T. Miyasaka, "Organometal halide perovskites as visible-light sensitizers for photovoltaic cells", Journal of the American Chemical Society **131** (2009) 6050–6051.

[6] W. S. Yang, J. H. Noh, N. J. Jeon, Y. C. Kim, S. Ryu, J. Seo, and S. I. Seok, "High-performance photovoltaic perovskite layers fabricated through intramolecular exchange", Science (2015) 1234–1237.

[7] J. Xiong, B. Yang, R. Wu, C. Cao, Y. Huang, C. Liu, Z. Hu, H. Huang, Y. Gao, and J. Yang, "Efficient and non-hysteresis CH3NH3PbI3/PCBM planar heterojunction solar cells", Organic Electronics **24** (2015) 106–112.

[8] J. You, Z. Hong, Y. M. Yang, Q. Chen, M. Cai, T.-B. Song, C.-C. Chen, S. Lu, Y. Liu, H. Zhou, et al., "Low-temperature solution-processed perovskite solar cells with high efficiency and flexibility", ACS Nano **8** (2014) 1674–1680.

[9] Q. Xue, Z. Hu, J. Liu, J. Lin, C. Sun, Z. Chen, C. Duan, J. Wang, C. Liao, W. M. Lau, F. Huang, H.-L. Yip, and Y. Cao, "Highly efficient fullerene/perovskite planar heterojunction solar cells via cathode modification with an amino-functionalized polymer interlayer", Journal of Materials Chemistry A **2** (2014) 19598–19603.

[10] Z. Xiao, C. Bi, Y. Shao, Q. Dong, Q. Wang, Y. Yuan, C. Wang, Y. Gao, and J. Huang, "Efficient, high yield perovskite photovoltaic devices grown by interdiffusion of solution-processed precursor stacking layers", Energy & Environmental Science **7** (2014) 2619–2623.

[11] O. Malinkiewicz, A. Yella, Y. H. Lee, G. M. Espallargas, M. Graetzel, M. K. Nazeeruddin, and H. J. Bolink, "Perovskite solar cells employing organic charge-transport layers", Nature Photonics **8** (2014) 128–132.

[12] J. Seo, S. Park, Y. C. Kim, N. J. Jeon, J. H. Noh, S. C. Yoon, and S. I. Seok, "Benefits of very thin PCBM and LiF layers for solution-processed p–i–n perovskite solar cells", Energy & Environmental Science **7** (2014) 2642–2646.

[13] C.-H. Chiang, Z.-L. Tseng, and C.-G. Wu, "Planar heterojunction perovskite/PC71BM solar cells with enhanced open-circuit voltage via a (2/1)-step spin-coating process", Journal of Materials Chemistry A **2** (2014) 15897–15903.

[14] S.-G. Li, K.-J. Jiang, M.-J. Su, X.-P. Cui, J.-H. Huang, Q.-Q. Zhang, X.-Q. Zhou, L.-M. Yang, and Y.-L. Song, "Inkjet printing of CH3NH3PbI3 on a mesoscopic TiO2 film for highly efficient perovskite solar cells", Journal of Materials Chemistry A **3** (2015) 9092–9097.

[15] K. Hwang, Y.-S. Jung, Y.-J. Heo, F. H. Scholes, S. E. Watkins, J. Subbiah, D. J. Jones, D.-Y. Kim, and D. Vak, "Toward large scale roll-to-roll production of fully printed perovskite solar cells", Advanced Materials **27** (2015) 1241–1247.

[16] T. A. Berhe, W.-N. Su, C.-H. Chen, C.-J. Pan, J.-H. Cheng, H.-M. Chen, M.-C. Tsai, L.-Y. Chen, A. A. Dubale, and B.-J. Hwang, "Organometal halide perovskite solar cells: degradation and stability", Energy & Environmental Science **9** (2016) 323–356.

[17] G. Niu, X. Guo, and L. Wang, "Review of recent progress in chemical stability of perovskite solar cells", Journal of Materials Chemistry A **3** (2015) 8970–8980.

[18] Y. S. Kwon, J. Lim, H.-J. Yun, Y.-H. Kim, and T. Park, "A diketopyrrolopyrrole-containing hole transporting conjugated polymer for use in efficient stable organic–inorganic hybrid solar cells based on a perovskite", Energy & Environmental Science **7** (2014) 1454–1460.

[19] A. Mei, X. Li, L. Liu, Z. Ku, T. Liu, Y. Rong, M. Xu, M. Hu, J. Chen, Y. Yang, et al., "A hole-conductor–free, fully printable mesoscopic perovskite solar cell with high stability", Science **345** (2014) 295–298.

[20] J. A. Christians, J. S. Manser, and P. V. Kamat, "Multifaceted excited state of CH3NH3PbI3: Charge separation, recombination, and trapping", The journal of physical chemistry letters **6** (2015) 2086–2095.

[21] J. Nelson et al., *The physics of solar cells*, volume 1 (World Scientific, 2003).

[22] W. Shockley and H. J. Queisser, "Detailed balance limit of efficiency of p-n junction solar cells", Journal of applied physics **32** (1961) 510–519.

[23] C. C. Stoumpos, C. D. Malliakas, and M. G. Kanatzidis, "Semiconducting tin and lead iodide perovskites with organic cations: phase transitions, high mobilities, and near-infrared photoluminescent properties", Inorganic chemistry **52** (2013) 9019–9038.

[24] D. B. Mitzi, K. Chondroudis, and C. R. Kagan, "Organic-inorganic electronics", IBM journal of research and development **45** (2001) 29–45.

[25] Y. Chen, M. He, J. Peng, Y. Sun, and Z. Liang, "Structure and growth control of organic–inorganic halide perovskites for optoelectronics: From polycrystalline films to single crystals", Advanced Science **3**.

[26] J. Emara, T. Schnier, N. Pourdavoud, T. Riedl, K. Meerholz, and S. Olthof, "Impact of film stoichiometry on the ionization energy and electronic structure of CH3NH3PbI3 perovskites", Advanced Materials **28** (2016) 553–559.

[27] S. Rühle, "Tabulated values of the shockley–queisser limit for single junction solar cells", Solar Energy **130** (2016) 139–147.

[28] W.-J. Yin, J.-H. Yang, J. Kang, Y. Yan, and S.-H. Wei, "Halide perovskite materials for solar cells: a theoretical review", Journal of Materials Chemistry A **3** (2015) 8926–8942.

[29] W.-J. Yin, T. Shi, and Y. Yan, "Unique properties of halide perovskites as possible origins of the superior solar cell performance", Advanced Materials **26** (2014) 4653–4658.

[30] I. Hill, A. Kahn, Z. Soos, and R. Pascal Jr, "Charge-separation energy in films of π-conjugated organic molecules", Chemical Physics Letters **327** (2000) 181–188.

[31] V. D'Innocenzo, G. Grancini, M. J. Alcocer, A. R. S. Kandada, S. D. Stranks, M. M. Lee, G. Lanzani, H. J. Snaith, and A. Petrozza, "Excitons versus free charges in organo-lead tri-halide perovskites", Nature communications **5** (2014) 1–6.

[32] M. Hirasawa, T. Ishihara, T. Goto, K. Uchida, and N. Miura, "Magnetoabsorption of the lowest exciton in perovskite-type compound (CH3NH3)PbI3", Physica B: Condensed Matter **201** (1994) 427–430.

[33] C. Wehrenfennig, G. E. Eperon, M. B. Johnston, H. J. Snaith, and L. M. Herz, "High charge carrier mobilities and lifetimes in organolead trihalide perovskites", Advanced Materials **26** (2014) 1584–1589.

[34] G. Xing, N. Mathews, S. Sun, S. S. Lim, Y. M. Lam, M. Grätzel, S. Mhaisalkar, and T. C. Sum, "Long-range balanced electron-and hole-transport lengths in organic-inorganic CH3NH3PbI3", Science **342** (2013) 344–347.

[35] S. D. Stranks, G. E. Eperon, G. Grancini, C. Menelaou, M. J. Alcocer, T. Leijtens, L. M. Herz, A. Petrozza, and H. J. Snaith, "Electron-hole diffusion lengths exceeding 1 micrometer in an organometal trihalide perovskite absorber", Science **342** (2013) 341–344.

[36] J. Kim, S.-H. Lee, J. H. Lee, and K.-H. Hong, "The role of intrinsic defects in methylammonium lead iodide perovskite", The journal of physical chemistry letters **5** (2014) 1312–1317.

[37] W.-J. Yin, T. Shi, and Y. Yan, "Unusual defect physics in CH3NH3PbI3 perovskite solar cell absorber", Applied Physics Letters **104** (2014) 063903.

[38] H.-S. Kim, C.-R. Lee, J.-H. Im, K.-B. Lee, T. Moehl, A. Marchioro, S.-J. Moon, R. Humphry-Baker, J.-H. Yum, J. E. Moser, et al., "Lead iodide perovskite sensitized all-solid-state submicron thin film mesoscopic solar cell with efficiency exceeding 9%", Scientific reports **2** (2012) 591.

[39] J. M. Ball, M. M. Lee, A. Hey, and H. J. Snaith, "Low-temperature processed meso-superstructured to thin-film perovskite solar cells", Energy & Environmental Science **6** (2013) 1739–1743.

[40] M. M. Lee, J. Teuscher, T. Miyasaka, T. N. Murakami, and H. J. Snaith, "Efficient hybrid solar cells based on meso-superstructured organometal halide perovskites", Science **338** (2012) 643–647.

[41] J. Burschka, N. Pellet, S.-J. Moon, R. Humphry-Baker, P. Gao, M. K. Nazeeruddin, and M. Grätzel, "Sequential deposition as a route to high-performance perovskite-sensitized solar cells", Nature **499** (2013) 316–319.

[42] D. Liu and T. L. Kelly, "Perovskite solar cells with a planar heterojunction structure prepared using room-temperature solution processing techniques", Nature photonics **8** (2014) 133–138.

[43] G. E. Eperon, V. M. Burlakov, P. Docampo, A. Goriely, and H. J. Snaith, "Morphological control for high performance, solution-processed planar heterojunction perovskite solar cells", Advanced Functional Materials **24** (2014) 151–157.

[44] J. R. Vig, "Ultraviolet-ozone cleaning of semiconductor surfaces", Technical report, DTIC Document (1992).

[45] F. C. Krebs, "Fabrication and processing of polymer solar cells: a review of printing and coating techniques", Solar energy materials and solar cells **93** (2009) 394–412.

[46] K. Norrman, A. Ghanbari-Siahkali, and N. Larsen, "6 studies of spin-coated polymer films", Annual Reports Section" C"(Physical Chemistry) **101** (2005) 174–201.

[47] C.-W. Chen, H.-W. Kang, S.-Y. Hsiao, P.-F. Yang, K.-M. Chiang, and H.-W. Lin, "Efficient and uniform planar-type perovskite solar cells by simple sequential vacuum deposition", Advanced Materials **26** (2014) 6647–6652.

[48] D. Shen, X. Yu, X. Cai, M. Peng, Y. Ma, X. Su, L. Xiao, and D. Zou, "Understanding the solvent-assisted crystallization mechanism inherent in efficient organic–inorganic halide perovskite solar cells", Journal of Materials Chemistry A **2** (2014) 20454–20461.

[49] A. Dualeh, N. Tétreault, T. Moehl, P. Gao, M. K. Nazeeruddin, and M. Grätzel, "Effect of annealing temperature on film morphology of organic–inorganic hybrid pervoskite solid-state solar cells", Advanced Functional Materials **24** (2014) 3250–3258.

[50] J.-H. Im, I.-H. Jang, N. Pellet, M. Grätzel, and N.-G. Park, "Growth of CH3NH3PbI3 cuboids with controlled size for high-efficiency perovskite solar cells", Nature nanotechnology **9** (2014) 927–932.

[51] J.-H. Im, H.-S. Kim, and N.-G. Park, "Morphology-photovoltaic property correlation in perovskite solar cells: One-step versus two-step deposition of CH3NH3PbI3", Apl Materials **2** (2014) 081510.

[52] P. Docampo, F. C. Hanusch, N. Giesbrecht, P. Angloher, A. Ivanova, and T. Bein, "Influence of the orientation of methylammonium lead iodide perovskite crystals on solar cell performance", APL Materials **2** (2014) 081508.

[53] P. Docampo, F. C. Hanusch, S. D. Stranks, M. Döblinger, J. M. Feckl, M. Ehrensperger, N. K. Minar, M. B. Johnston, H. J. Snaith, and T. Bein, "Solution deposition-conversion for planar heterojunction mixed halide perovskite solar cells", Advanced Energy Materials **4**.

[54] C. Bi, Q. Wang, Y. Shao, Y. Yuan, Z. Xiao, and J. Huang, "Non-wetting surface-driven high-aspect-ratio crystalline grain growth for efficient hybrid perovskite solar cells", Nature communications **6**.

[55] Z. Song, S. C. Watthage, A. B. Phillips, B. L. Tompkins, R. J. Ellingson, and M. J. Heben, "Impact of processing temperature and composition on the formation of methylammonium lead iodide perovskites", Chemistry of Materials **27** (2015) 4612–4619.

[56] W. Zhang, M. Saliba, D. T. Moore, S. K. Pathak, M. T. Hörantner, T. Stergiopoulos, S. D. Stranks, G. E. Eperon, J. A. Alexander-Webber, A. Abate, et al., "Ultrasmooth organic–inorganic perovskite thin-film formation and crystallization for efficient planar heterojunction solar cells", Nature communications **6**.

[57] D. T. Moore, H. Sai, K. W. Tan, D.-M. Smilgies, W. Zhang, H. J. Snaith, U. Wiesner, and L. A. Estroff, "Crystallization kinetics of organic–inorganic trihalide perovskites and the role of the lead anion in crystal growth", Journal of the American Chemical Society **137** (2015) 2350–2358.

[58] J. You, Y. M. Yang, Z. Hong, T.-B. Song, L. Meng, Y. Liu, C. Jiang, H. Zhou, W.-H. Chang, G. Li, et al., "Moisture assisted perovskite film growth for high performance solar cells", Applied Physics Letters **105** (2014) 183902.

[59] Y. Wu, A. Islam, X. Yang, C. Qin, J. Liu, K. Zhang, W. Peng, and L. Han, "Retarding the crystallization of PbI2 for highly reproducible planar-structured perovskite solar cells via sequential deposition", Energy & Environmental Science **7** (2014) 2934–2938.

[60] M. Saliba, K. W. Tan, H. Sai, D. T. Moore, T. Scott, W. Zhang, L. A. Estroff, U. Wiesner, and H. J. Snaith, "Influence of thermal processing protocol upon the crystallization and photovoltaic performance of organic–inorganic lead trihalide perovskites", The Journal of Physical Chemistry C **118** (2014) 17171–17177.

[61] S. D. Stranks, P. K. Nayak, W. Zhang, T. Stergiopoulos, and H. J. Snaith, "Formation of thin films of organic–inorganic perovskites for high-efficiency solar cells", Angewandte Chemie International Edition **54** (2015) 3240–3248.

[62] C. Bi, Y. Shao, Y. Yuan, Z. Xiao, C. Wang, Y. Gao, and J. Huang, "Understanding the formation and evolution of interdiffusion grown organolead halide perovskite thin films by thermal annealing", Journal of Materials Chemistry A **2** (2014) 18508–18514.

[63] V. Burlakov, G. Eperon, H. Snaith, S. Chapman, and A. Goriely, "Controlling coverage of solution cast materials with unfavourable surface interactions", Applied Physics Letters **104** (2014) 091602.

[64] P. Docampo, J. M. Ball, M. Darwich, G. E. Eperon, and H. J. Snaith, "Efficient organometal trihalide perovskite planar-heterojunction solar cells on flexible polymer substrates", Nature communications **4** (2013) 1–6.

[65] E. Zheng, X.-F. Wang, J. Song, L. Yan, W. Tian, and T. Miyasaka, "PbI2-based dipping-controlled material conversion for compact layer free perovskite solar cells", ACS applied materials & interfaces **7** (2015) 18156–18162.

[66] N. J. Jeon, J. H. Noh, Y. C. Kim, W. S. Yang, S. Ryu, and S. I. Seok, "Solvent engineering for high-performance inorganic–organic hybrid perovskite solar cells", Nature materials **13** (2014) 897–903.

[67] J. W. Jung, S. T. Williams, and A. K.-Y. Jen, "Low-temperature processed high-performance flexible perovskite solar cells via rationally optimized solvent washing treatments", RSC Advances **4** (2014) 62971–62977.

[68] M. Xiao, F. Huang, W. Huang, Y. Dkhissi, Y. Zhu, J. Etheridge, A. Gray-Weale, U. Bach, Y.-B. Cheng, and L. Spiccia, "A fast deposition-crystallization procedure for highly efficient lead iodide perovskite thin-film solar cells", Angewandte Chemie **126** (2014) 10056–10061.

[69] A. S. Milev, M. A. Wilson, G. K. Kannangara, H. Feng, and P. A. Newman, "Isothermal evaporation of ethanol in a dynamic gas atmosphere", The Journal of Physical Chemistry A **116** (2011) 150–157.

[70] Y. Shao, Z. Xiao, C. Bi, Y. Yuan, and J. Huang, "Origin and elimination of photocurrent hysteresis by fullerene passivation in CH3NH3PbI3 planar heterojunction solar cells", Nature communications **5** (2014) 1–7.

[71] Z. Xiao, Q. Dong, C. Bi, Y. Shao, Y. Yuan, and J. Huang, "Solvent annealing of perovskite-induced crystal growth for photovoltaic-device efficiency enhancement", Advanced Materials **26** (2014) 6503–6509.

[72] Q. Chen, H. Zhou, T.-B. Song, S. Luo, Z. Hong, H.-S. Duan, L. Dou, Y. Liu, and Y. Yang, "Controllable self-induced passivation of hybrid lead iodide perovskites toward high performance solar cells", Nano letters **14** (2014) 4158–4163.

[73] M. K. Gangishetty, R. W. Scott, and T. L. Kelly, "Effect of relative humidity on crystal growth, device performance and hysteresis in planar heterojunction perovskite solar cells", Nanoscale **8** (2016) 6300–6307.

[74] D. Liu, M. Gangishetty, and T. Kelly, "Effect of CH3NH3PbI3 thickness on device efficiency in planar heterojunction perovskite solar cells", Journal of Materials Chemistry A **2** (2014) 19873–19881.

[75] Q. Wang, Y. Shao, H. Xie, L. Lyu, X. Liu, Y. Gao, and J. Huang, "Qualifying composition dependent p and n self-doping in CH3NH3PbI3", Applied Physics Letters **105** (2014) 163508.

[76] T. Supasai, N. Rujisamphan, K. Ullrich, A. Chemseddine, and T. Dittrich, "Formation of a passivating CH3NH3PbI3/PbI2 interface during moderate heating of CH3NH3PbI3 layers", Applied Physics Letters **103** (2013) 183906.

[77] D. Cao, C. Stoumpos, C. Malliakas, M. Katz, O. Farha, J. Hupp, and M. Kanatzidis, "Remnant pbi2, an unforseen necessity in high-efficiency hybrid perovskite-based solar cells?", Applied Physics Letters Materials **2** (2014) 1–7.

[78] S. Sun, T. Salim, N. Mathews, M. Duchamp, C. Boothroyd, G. Xing, T. C. Sum, and Y. M. Lam, "The origin of high efficiency in low-temperature solution-processable bilayer organometal halide hybrid solar cells", Energy & Environmental Science **7** (2014) 399–407.

[79] J.-Y. Jeng, Y.-F. Chiang, M.-H. Lee, S.-R. Peng, T.-F. Guo, P. Chen, and T.-C. Wen, "CH3NH3PbI3 perovskite/fullerene planar-heterojunction hybrid solar cells", Advanced Materials **25** (2013) 3727–3732.

[80] C. Clegg and I. G. Hill, "Systematic study on the impact of water on the performance and stability of perovskite solar cells", RSC Advances **6** (2016) 52448–52458.

[81] B. Hailegnaw, S. Kirmayer, E. Edri, G. Hodes, and D. Cahen, "Rain on methylammonium lead iodide based perovskites: Possible environmental effects of perovskite solar cells", The Journal of Physical Chemistry Letters **6** (2015) 1543–1547.

[82] J. M. Frost, K. T. Butler, F. Brivio, C. H. Hendon, M. Van Schilfgaarde, and A. Walsh, "Atomistic origins of high-performance in hybrid halide perovskite solar cells", Nano letters **14** (2014) 2584–2590.

[83] J. Yang, B. D. Siempelkamp, D. Liu, and T. L. Kelly, "Investigation of CH3NH3PbI3 degradation rates and mechanisms in controlled humidity environments using in situ techniques", ACS Nano **9** (2015) 1955–1963.

[84] A. M. Leguy, Y. Hu, M. Campoy-Quiles, M. I. Alonso, O. J. Weber, P. Azarhoosh, M. Van Schilfgaarde, M. T. Weller, T. Bein, J. Nelson, et al., "Reversible hydration of CH3NH3PbI3 in films, single crystals, and solar cells", Chemistry of Materials **27** (2015) 3397–3407.

[85] H. Zhou, Q. Chen, G. Li, S. Luo, T.-B. Song, H.-S. Duan, Z. Hong, J. You, Y. Liu, and Y. Yang, "Interface engineering of highly efficient perovskite solar cells", Science **345** (2014) 542–546.

[86] S. Pathak, A. Sepe, A. Sadhanala, F. Deschler, A. Haghighirad, N. Sakai, K. C. Goedel, S. D. Stranks, N. Noel, M. Price, et al., "Atmospheric influence upon crystallization and electronic disorder and its impact on the photophysical properties of organic–inorganic perovskite solar cells", ACS nano **9** (2015) 2311–2320.

[87] G. E. Eperon, S. N. Habisreutinger, T. Leijtens, B. J. Bruijnaers, J. J. van Franeker, D. W. deQuilettes, S. Pathak, R. J. Sutton, G. Grancini, D. S. Ginger, et al., "The importance of moisture in hybrid lead halide perovskite thin film fabrication", ACS nano **9** (2015) 9380–9393.

[88] C.-G. Wu, C.-H. Chiang, Z.-L. Tseng, M. K. Nazeeruddin, A. Hagfeldt, and M. Grätzel, "High efficiency stable inverted perovskite solar cells without current hysteresis", Energy & Environmental Science **8** (2015) 2725–2733.

[89] N. Adhikari, A. Dubey, E. A. Gaml, B. Vaagensmith, K. M. Reza, S. A. A. Mabrouk, S. Gu, J. Zai, X. Qian, and Q. Qiao, "Crystallization of a perovskite

film for higher performance solar cells by controlling water concentration in methyl ammonium iodide precursor solution", Nanoscale **8** (2016) 2693–2703.

[90] B. Conings, A. Babayigit, T. Vangerven, J. D'Haen, J. Manca, and H.-G. Boyen, "The impact of precursor water content on solution-processed organometal halide perovskite films and solar cells", Journal of Materials Chemistry A **3** (2015) 19123–19128.

[91] X. Gong, M. Li, X.-B. Shi, H. Ma, Z.-K. Wang, and L.-S. Liao, "Controllable perovskite crystallization by water additive for high-performance solar cells", Advanced Functional Materials **25** (2015) 6671–6678.

[92] Y. Hui and R. D. Webster, "Absorption of water into organic solvents used for electrochemistry under conventional operating conditions", Analytical chemistry **83** (2011) 976–981.

[93] J. Juillard, "Dimethylformamide: purification tests for purity and physical properties", Pure Appl Chem **49** (1977) 885–892.

[94] E. Unger, E. Hoke, C. Bailie, W. Nguyen, A. Bowring, T. Heumüller, M. Christoforo, and M. McGehee, "Hysteresis and transient behavior in current–voltage measurements of hybrid-perovskite absorber solar cells", Energy & Environmental Science **7** (2014) 3690–3698.

[95] H. J. Snaith, A. Abate, J. M. Ball, G. E. Eperon, T. Leijtens, N. K. Noel, S. D. Stranks, J. T.-W. Wang, K. Wojciechowski, and W. Zhang, "Anomalous hysteresis in perovskite solar cells", The Journal of Physical Chemistry Letters **5** (2014) 1511–1515.

[96] B. C. O'Regan, P. R. Barnes, X. Li, C. Law, E. Palomares, and J. M. Marin-Beloqui, "Optoelectronic studies of methylammonium lead iodide perovskite solar cells with mesoporous TiO2: Separation of electronic and chemical charge storage, understanding two recombination lifetimes, and the evolution of band offsets during J–V hysteresis", Journal of the American Chemical Society **137** (2015) 5087–5099.

[97] W. Tress, N. Marinova, T. Moehl, S. Zakeeruddin, M. K. Nazeeruddin, and M. Grätzel, "Understanding the rate-dependent J–V hysteresis, slow time component, and aging in CH3NH3PbI3 perovskite solar cells: the role of a compensated electric field", Energy & Environmental Science **8** (2015) 995–1004.

[98] C. Eames, J. M. Frost, P. R. Barnes, B. C. O'regan, A. Walsh, and M. S. Islam, "Ionic transport in hybrid lead iodide perovskite solar cells", Nature communications **6** (2015) 1–6.

[99] J. M. Azpiroz, E. Mosconi, J. Bisquert, and F. De Angelis, "Defect migration in methylammonium lead iodide and its role in perovskite solar cell operation", Energy & Environmental Science **8** (2015) 2118–2127.

[100] J. Haruyama, K. Sodeyama, L. Han, and Y. Tateyama, "First-principles study of ion diffusion in perovskite solar cell sensitizers", Journal of the American Chemical Society **137** (2015) 10048–10051.

[101] Y. Shao, Y. Fang, T. Li, Q. Wang, Q. Dong, Y. Deng, Y. Yuan, H. Wei, M. Wang, A. Gruverman, et al., "Grain boundary dominated ion migration in polycrystalline organic-inorganic halide perovskite films", Energy & Environmental Science .

[102] B. Chen, M. Yang, X. Zheng, C. Wu, W. Li, Y. Yan, J. Bisquert, G. Garcia-Belmonte, K. Zhu, and S. Priya, "Impact of capacitive effect and ion migration on the hysteretic behavior of perovskite solar cells", The journal of physical chemistry letters **6** (2015) 4693–4700.

[103] C. Li, S. Tscheuschner, F. Paulus, P. E. Hopkinson, J. Kießling, A. Köhler, Y. Vaynzof, and S. Huettner, "Iodine migration and its effect on hysteresis in perovskite solar cells", Advanced Materials .

[104] H. Yu, H. Lu, F. Xie, S. Zhou, and N. Zhao, "Native defect-induced hysteresis behavior in organolead iodide perovskite solar cells", Advanced Functional Materials .

[105] T.-Y. Yang, G. Gregori, N. Pellet, M. Grätzel, and J. Maier, "The significance of ion conduction in a hybrid organic–inorganic lead-iodide-based perovskite photosensitizer", Angewandte Chemie **127** (2015) 8016–8021.

[106] P. Delugas, C. Caddeo, A. Filippetti, and A. Mattoni, "Thermally activated point-defects diffusion in methylammonium lead trihalide: Anisotropic and ultra-high mobility of iodine", The journal of physical chemistry letters .

[107] J. H. Heo, H. J. Han, D. Kim, T. K. Ahn, and S. H. Im, "Hysteresis-less inverted CH3NH3PbI3 planar perovskite hybrid solar cells with 18.1% power conversion efficiency", Energy & Environmental Science **8** (2015) 1602–1608.

[108] H.-S. Kim, I.-H. Jang, N. Ahn, M. Choi, A. Guerrero, J. Bisquert, and N.-G. Park, "Control of I–V hysteresis in CH3NH3PbI3 perovskite solar cell", The journal of physical chemistry letters **6** (2015) 4633–4639.

[109] J. Carrillo, A. Guerrero, S. Rahimnejad, O. Almora, I. Zarazua, E. Mas-Marza, J. Bisquert, and G. Garcia-Belmonte, "Ionic reactivity at contacts and aging of methylammonium lead triiodide perovskite solar cells", Advanced Energy Materials .

[110] J. Xu, A. Buin, A. H. Ip, W. Li, O. Voznyy, R. Comin, M. Yuan, S. Jeon, Z. Ning, J. J. McDowell, et al., "Perovskite-fullerene hybrid materials suppress hysteresis in planar diodes", Nature communications **6** (2015) 1–8.

[111] C. Zhao, B. Chen, X. Qiao, L. Luan, K. Lu, and B. Hu, "Revealing underlying processes involved in light soaking effects and hysteresis phenomena in perovskite solar cells", Advanced Energy Materials **5** (2015) 1–6.

[112] W. Zhang, V. M. Burlakov, D. J. Graham, T. Leijtens, A. Osherov, V. Bulović, H. J. Snaith, D. S. Ginger, S. D. Stranks, et al., "Photo-induced halide redistribution in organic-inorganic perovskite films", Nature communications **7**.

[113] E. Mosconi, D. Meggiolaro, H. Snaith, S. D. Stranks, and F. De Angelis, "Light-induced annihilation of frenkel defects in organo-lead halide perovskites", Energy & Environmental Science .

[114] E. Mosconi, J. M. Azpiroz, and F. De Angelis, "Ab initio molecular dynamics simulations of methylammonium lead iodide perovskite degradation by water", Chemistry of Materials **27** (2015) 4885–4892.

[115] I. Campbell and B. Crone, "Improving carrier injection in organic diodes by incorporating charge trapping molecules", Applied physics letters **88** (2006) 172113.

[116] C. Muller, T. Glaser, M. Plogmeyer, M. Sendner, S. Doring, A. A. Bakulin, C. Brzuska, R. Scheer, M. S. Pshenichnikov, W. Kowalsky, et al., "Water infiltration in methylammonium lead iodide perovskite: Fast and inconspicuous", Chemistry of Materials **27** (2015) 7835–7841.

[117] G. Niu, W. Li, F. Meng, L. Wang, H. Dong, and Y. Qiu, "Study on the stability of CH3NH3PbI3 films and the effect of post-modification by aluminum oxide in all-solid-state hybrid solar cells", Journal of Materials Chemistry A **2** (2014) 705–710.

[118] J. A. Christians, P. A. Miranda Herrera, and P. V. Kamat, "Transformation of the excited state and photovoltaic efficiency of CH3NH3PbI3 perovskite upon controlled exposure to humidified air", Journal of the American Chemical Society **137** (2015) 1530–1538.

[119] B. R. Vincent, K. N. Robertson, T. S. Cameron, and O. Knop, "Alkylammonium lead halides. part 1. isolated PbI64-ions in (CH3NH3)4PbI62H2O", Canadian journal of chemistry **65** (1987) 1042–1046.

[120] D. A. Egger, L. Kronik, and A. M. Rappe, "Theory of hydrogen migration in organic–inorganic halide perovskites", Angewandte Chemie International Edition **54** (2015) 12437–12441.

[121] W. Zhou, Y. Zhao, C. Shi, H. Huang, J. Wei, R. Fu, K. Liu, D. Yu, and Q. Zhao, "Reversible healing effect of water molecules on fully crystallized metal-halide perovskite film", The Journal of Physical Chemistry C **120** (2016) 4759–4765.

[122] G. Grancini, V. D'Innocenzo, E. Dohner, N. Martino, A. S. Kandada, E. Mosconi, F. De Angelis, H. Karunadasa, E. Hoke, and A. Petrozza, "CH3NH3PbI3 perovskite single crystals: surface photophysics and their interaction with the environment", Chemical Science **6** (2015) 7305–7310.

[123] F. Wang, H. Yu, H. Xu, and N. Zhao, "HPbI3: A new precursor compound for highly efficient solution-processed perovskite solar cells", Advanced Functional Materials **25** (2015) 1120–1126.